Hybrid Transparent Conductive Oxide Nanostructured Materials for Photovoltaic Applications

by

Marwa Abd-Ellah

A thesis

presented to the University of Waterloo

in fulfillment of the

thesis requirement for the degree of

Doctor of Philosophy

in

Chemistry

Waterloo, Ontario, Canada, 2015

AUTHOR'S DECLARATION

This thesis consists of material all of which I authored or co-authored: see Statement of Contributions included in the thesis. This is a true copy of the thesis, including any required final revisions, as accepted by my examiners.

I understand that my thesis may be made electronically available to the public.

Statement of Contributions

Marwa Abd-Ellah contributed to the concept and design of the study. M. A. performed the experiments including samples preparation and characterization. M.A. analyzed and interpreted the data, and tested the constructed solar cell performance. Samad Bazargan prepared the SnO_2 nanostructures using the pulsed laser deposition system (Chapter 6). M.A. wrote the papers (parts of which are used in Chapters 3 & 6). Tong Leung, Lei Zhang, Joseph P. Thomas, Nina F. Heinig, Liyan Zhao, Nafiseh Moghimi, Xiongyao Wang, Md Anisur Rahman, and Saurabh Sirvastava discussed the results and commented on the manuscripts.

Abstract

In Ontario, there are great incentives to invest in solar cell research through the Feed-In Tariff program, which has successfully increased the total connected capacity of solar power in Ontario to well over 215 MW. Extensive studies have been conducted on fabrication of efficient solar cells, with the most mature technology being silicon-based solar cells. However, other types of solar cells have been introduced as alternatives to silicon based solar cells due to their laborious work, energy consumption, and high cost of production. Different inorganic and organic photovoltaic systems including dye-sensitized, organic/polymer, quantum-dot, and hybrid nanocrystal/polymer hetero-junctions solar cells have been proposed to provide comparable efficiencies.

Transparent conductive oxides are usually the main component in any solar system because of its role as an electrode photoanode, acting as a diffusion barrier and an open-circuit voltage attenuator. These are due to their high electrical conductivity, wide optical transmittance, and relatively ease of synthesis. As a result, a rich amount of studies on their synthesis, modification, and application as photo-catalytic electrodes, gas sensors, photonic crystals, and solar cell photoanodes exists in the literature. Their use in photovoltaics as thin film materials has since evolved into nanostructured films, as numerous studies have showed that the material morphology is an important parameter in improving solar cell performance. Many nanostructured transparent conductive oxide films have been extensively investigated for use as an n-type semiconductor in a p-n junction solar cell system or as a photoanode in a dye-sensitized solar cell (DSSC). Thus far these applications have proven challenging in terms of achieving high device efficiencies, particularly by taking advantage of their inherently higher surface area-to-volume ratio, better photon harvesting, and enhanced interparticle charge transport with shorter diffusion lengths across the device structure.

With a large direct band gap (3.37 eV), a large exciton binding energy (60 m eV), and high electron mobility (120 $cm^2\ V^{-1}\ s^{-1}$), zinc oxide (ZnO) is considered an excellent candidate as an (n-type) transparent semiconducting material at room temperature for photovoltaic application. In the present work, two different ZnO nanostructural morphologies are prepared by controlling the electrolyte conductivity using a direct, catalyst- and seed-layer free electrodeposition method. The effect of deposition time and temperature on the growth of the high-specific-surface-area ZnO nanotubes electrodeposited is studied. Furthermore, the morphology, crystallinity, and chemical composition of the resulting ZnO nanotubes and nanorods are fully characterized with a proposed

model of their growth mechanism. These one-dimensional ZnO nanostructures are then employed as an n-type semiconductor, along with a p-type Cu_2O thin film, to fabricate an inorganic p-n junction solar cell. As an important step to improve device performance, the electrical and optical properties of the p-type Cu_2O film are optimized by simple annealing. Two different device structures, consisting of the electrodeposited ZnO nanorods and nanotubes grown on the top of a thick n-type ZnO seed layer (500 nm) covered by an optimized (2.5μm) p-type Cu_2O layer (in order to provide the full built-in potential across the junction area), are fabricated. The relations of structural morphology (i.e. nanotube vs nanorod) and characteristic solar cell parameters are investigated. The new device architecture is found to offer minimum leakage path and reduced recombination loss expected in a typical nanostructure-based solar cell. A photon-to-electron conversion efficiency (PCE) of 0.8 % is obtained for ZnO nanotubes compared to other traditional one-dimensional nanostructures (i.e. nanorods or nanowires) that is due to the increased junction area and the better charge collection. These results illustrate the advantage of single-step electrodeposition of ZnO nanotubes, which provide a larger interfacial area and a much lower defect density than previously reported nanotubes obtained by etching ZnO nanorods.

Taking advantage of their higher electron dynamics than the classical TiO_2, ZnO and SnO_2 are employed as photoanode materials to fabricate an organic DSSC system. To further improve the optical absorption, the effects of surface modification using gold nanoparticles to ZnO nanotubes are investigated. Different gold electrolyte concentrations are used to manipulate the plasmonic nanoparticle size while deposition time is used to control the aerial density. These studies lead to a significant increase in the PCE for DSSC based on ZnO nanotubes with gold nanoparticle modification (6%) when compared to that with pristine ZnO nanotubes (4.7%). Surface decoration with plasmonic gold nanoparticles therefore provides an efficient approach to creating not only high surface area for superior loading of dye molecules but also enhanced absorption specifically in the visible range by taking advantage of their surface plasmon resonance effect.

Hierarchical one-dimensional SnO_2 nanostructures are also employed as photoanode material for DSSC application. With a band gap of 3.8 eV, low UV degradation characteristic and generally high thermal and chemical stability, SnO_2 is also an excellent photoanode alternative to TiO_2. Almost 10-fold enhancement of PCE (3.6%) when compared with pristine SnO_2 nanobelts with (0.48%) is obtained for these hierarchical SnO_2 nanostructures. This significant improvement is in part due to better dye loading of highly branched nanostructures. Additional surface passivation has also been

performed on the as-deposited hierarchical SnO_2 nanostructures by dip-coating with an MgO passivation layer of appropriately optimized thickness. Such an insulating layer is found to effectively reduce the recombination loss process caused by the higher electron mobility of SnO_2 photoanode nanostructures. This MgO-passivation treatment further enhances the PCE to (4.14%).

The present work therefore shows that one-dimensional ZnO and SnO_2 nanostructures provide a viable, powerful platform for developing the next-generation photovoltaic devices. This study further demonstrates the novel techniques used to significantly enhance the PCEs for both inorganic p-n junction solar cell and organic DSSC.

Acknowledgements

First and foremost, all praise to Allah the lord of the entire universe.

I would like to express my deep appreciation to my supervisor Prof. Tong Leung for his continuous encouragement and effective guidance during my study. He provided me the opportunity to learn with on-hand experience using different tools, and helpful advice and friendly spirit. He will always be my mentor in all aspects of my life. My special thanks go to my advisory committee members: Prof. Dan Thomas, Prof. Magdy Salama, and Prof. Vivek Maheshwari, for their constructive feedback and their highly inspiring discussions during our annual meetings.

Distinct recognition is due for our postdoctoral fellows at Waterloo Advanced Technology Laboratory (WATLab): Dr. Nina Heinig and Dr. Liyan Zhao for their expert training and continual help with different microscopy and spectroscopy tools. A special thank goes to Dr. Samad Bazargan who prepared the SnO_2 nanostructures using the pulsed laser deposition system. I would also like to express my gratitude to Dr. Lei Zhang, Dr. Joseph Palathinkal Thomas, and Dr. Nafiseh Moghimi for their endless patience and outstanding assistance. I am truly thankful to my senior colleagues and group members: Dr. Xiongyao Wang, Dr. Avisek Chatterjee, Dr. Yan Wang-Duffort, Dr. Shantinarayan Rout, Jung-Soo Kang, Bahareh Rahsepar, Saurabh Srivastava, Anisur Rahman, Donald McGillivray, Hanieh Farkhondeh, and Mahdi Beedel, for their sincere friendship and the positive attitude within our group. I will always be proud for being a part of this significant family. I gratefully acknowledge all members of the University of Waterloo Chemistry Department, the Waterloo Institute for Nanotechnology (WIN), and the Natural Sciences and Engineering Research Council of Canada (NSERC) for their generous funding of my research in Canada. I am also grateful to the Chemistry Department at Al-Azhar University in Egypt for their kind support.

Last but not least, I express my warm gratefulness to my family, my parents and my sibling for their endless love and care, which give me the strength to reach my goals. Finally, I want to express my deep sincere thanks to the love of my life, Mohamed, who always has my back and has a lot of faith in me sometimes even more than myself.

Dedication

To my much-loved Family,

To my beloved Mohamed,

To my sweetheart Yusuf

Table of Contents

List of Figures

List of Tables

Chapter 1
Introduction

1.1 Nanostructured Transparent Conductive Oxides

Nanotechnology has been expanding extensively into many fields since the ground breaking talk "*There is Plenty of Room at the Bottom*" by Richard P. Feynman in 1959.[1] Generally, nanostructured materials are ultrafine structures with a grain size on the order of nanometers (10^{-9} m) or, in a broader description, any material that contains grains or clusters below 100 nm.[2] In the past few decades, different materials have been prepared in the nanoscale using various techniques. A great number of studies have been performed on the functionalization and application of novel nanostructured materials, demonstrating the power of quantum effects that are responsible for the new behavior and properties of these materials at their nanoscale.

Transparent conducting oxides (TCOs) are one of the well-known semiconductors that have been synthesized at the nanoscale and utilized in many applications due to their availability, biocompatibility, and versatile nanostructural morphologies. In general, TCOs are conductive metal oxides with a wide band gap (greater than 3 eV) that enables the transmittance of light up to the ultra-violet (UV) region. Ordinarily, undoped oxides with a band gap of larger than 3 eV would be an insulator at room temperature. However, doping of such oxides would increase the charge carrier density and allow the electrons to move freely, which in effect move the Fermi level into the conduction band. Interestingly, TCOs are intrinsic oxides with full *d* band orbitals and they possess stoichiometric defects such as oxygen vacancies that can be ionized and used to donate electrons into the conduction band. TCOs are also popular because of their high electrical (semiconducting) properties that lie between metals and insulators due to their unique electronic band structures, allowing electrons to be thermally excited across the band gaps and contribute in the electrical conduction process.[3] There are many examples of TCO materials have been synthesized in the nanoscale with an enormous number of morphologies using a variety of dry and wet synthesis techniques. As a result of their unique optical and electrical properties, the fundamentally interesting band structure, and the high surface area to volume ratio of their nanostructures, TCOs are considered excellent candidates as active materials and are commonly used in different photovoltaic systems.[4]

1.1.1 Properties of nanostructured transparent conductive oxides

Nanostructured TCOs are abundant biodegradable materials, which can be prepared at moderate cost using many synthesis techniques. TCOs are particularly well known for their high transparency (above 80%) in the visible spectrum. They also have high thermal stability, and mechanical and chemical durability, which are suitable for flexible electronic devices. In addition, their high conductivity (10^3~10^4 S/cm), together with their ability to be easily doped extrinsically or intrinsically in an sufficient quantity to further enhance the carrier concentration tailored to specific application, have make TCOs very versatile electronic materials.

In 1907, Badeker uncovered the first TCO by oxidation of metallic Cd to produce CdO thin film, which was shown to be optically transparent while remaining highly conducting. Shortly thereafter, more materials exhibiting similar characteristics of both optical transparency and high electrical conductivity were discovered.[4] These include both undoped oxides, such as ZnO, SnO_2, In_2O_3, and TiO_2, and doped oxides such as aluminium-doped ZnO (AZO), tin-doped In_2O_3 (ITO), and antimony or fluorine doped SnO_2 (ATO and FTO, respectively). Table 1.1 summarizes some important material properties of common TCOs, as reproduced from Gordon.[5]

Table 1.1 Summary of material properties of selected important TCOs[5*]

Property (unit)	CdO	In_2O_3	SnO_2	ZnO
Mineral name	-	-	cassiterite	zincite
Average material amount in the earth's crust (ppm)	0.3	0.1	40	132
Band gap E_g (300 K) (eV)	2.3	3.75(dir)	3.6(dir)	3.4(dir)
Effective electron mass m^*/me	0.15/0.11	0.35	0.30	0.28
Lattice mobility ($cm^2/V\ s$)	620	210	255	200
Minimum resistivity (Ω cm)	$\approx 3 \times 10^{-5}$	$\approx 1 \times 10^{-4}$	$\approx 3 \times 10^{-4}$	$\approx 2 \times 10^{-4}$

[*] Reproduced with permission from: Gordon, R. G., MRS Bull. 25, 52-57, 2000. Copyright (2000) by the Materials Research Society.

1.1.2 Nanostructured transparent conductive oxides for photovoltaic applications

The optical and electrical properties of nanostructured TCO films are the main attractions for many optoelectronic applications, including flat panel displays, touch panel controls, organic light emitting diodes, and solar cells. Depending on the application, they can be used to build diodes, which depend on the band alignment of the n-type conducting oxides to the p-type semiconductor or vice versa. TCOs can also be used to form ohmic contact or Schottky diode, depending on the Schottky barrier height created when a conducting oxide comes in contact with a metal. The barrier height (Φ_B) corresponds to the difference between the electron affinity of the semiconductor (χ) divided by the charge (q) and the work function of the metal (Φ_{metal}), according to the equation:

$$\Phi_B \approx \Phi_{metal} - \chi/q$$

Interestingly, n-type TCOs have generally high work functions, even higher if they can be maximized by having an oxygen-rich, outer surface during synthesis. As shown in Figure 1.1, ZnO, SnO_2, and In_2O_3 have their conduction band minima lying deeper than the Fermi levels of the respective parent metals. These findings confirm the prominent behavior of most n-type TCOs from normal oxides.[6] Beside their work functions, there are many other considerations before choosing TCO materials for photovoltaic applications. Their band alignment, the ease of their processing, and the material cost are some other important parameters, which should be evaluated carefully.

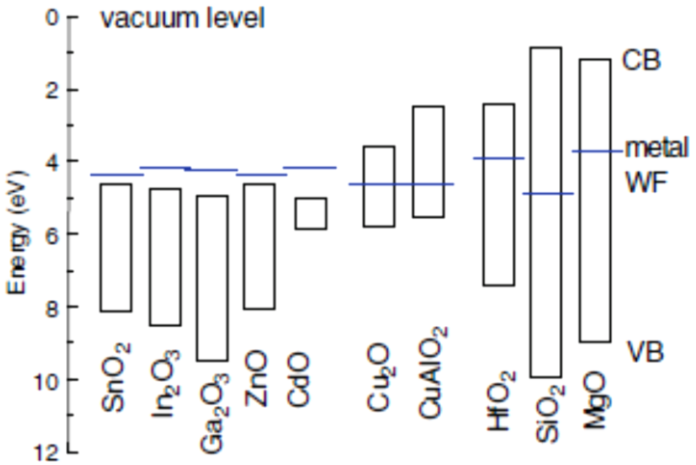

Figure 1.1 Comparison of the band gaps of TCOs relative to the work functions (WFs) of their parent metals. The parent metal WF for (n-type) TCO lies above the conduction band of the oxide. [6] †

† Reproduced with permission from: Robertson, J., and Falabretti, B. Handbook of Transparent Conductors. Hosono, H., Paine, D. C.; Ginely, D., Ed., Springer US, 2011 Copyright (2011) by Springer.

Several examples of TCOs have been commonly used in many inorganic and organic solar cells, including TiO_2, In_2O_3, ZnO, CdO, and SnO_2. Ongoing research is continuing to find new alternatives with better interfacial properties and higher thermal and chemical stability. Table 1.2 shows the commonly used TCOs in different types of solar cells, along with their requirements for solar cell applications.[7] In the present work, we will focus on two currently used materials: ZnO and SnO_2, as green materials that can be produced using simple processing conditions. They represent an interesting, readily available transparent semiconductors that are among the most commonly used materials for solar cell and other applications, due to their attractive properties.

Table 1.2 Summary of commonly used TCOs for photovoltaic applications.[7‡]

Cell Type	TCO in Current Use	TCO Needs	Materials Goals
Heterojunction with intrinsic thin layer (HIT) cell	Indium tin oxide (ITO)	Smooth, good interfacial properties, very good conductivity, low-temperature deposition, light trapping	Indium zinc oxide (IZO), indium-free materials, ZnO
Copper indium gallium selenide (CIGS)	Intrinsic-ZnO/Al:ZnO	Interfacial stability to CdS, low-temperature deposition, resistance to diffusion and shorting, need to make/improve the junction	Single-layer TCO to replace two layers and CdS layer
CdTe	(SnO_2) Zn_2SnO_4/Cd_2SnO_4	Stable interface to CdS/CdTe at temperature, diffusion barrier	Doping of ZnSnOx materials, single-layer TCO
Nano-hybrid polymer cell	ZnO, SnO_2, TiO_2	Nanostructure with right length scale, work-function matching, interface with organic, correct doping level for carrier transport	Self-organized structures core–shell structures, new nonconventional TCOs
Grätzel cell	TiO_2	Nanostructure with high electron mobility	Improved TiO_2 morphology and possible use of doped materials, new non-TiO_2 materials
Amorphous Si	SnO_2, ITO, and ZnO; many cells employ two TCOs	Temperature stability, chemical stability, and appropriate texture for both TCO layers	Higher conductivity, texture, and ohmic contact for both TCO layers

‡ Reproduced with permission from: Fortunato, E., Ginley, D., Hosono, H., and Paine, D. C., MRS Bull. 32, 242-247, 2007. Copyright (2007) by the Materials Research Society.

1.2 Nanostructured Transparent Conductive Zinc Oxide

Zinc oxide (ZnO) is a well-known (II-IV) binary compound semiconductor that possesses a direct wide band gap of 3.4 eV with a large exciton binding energy (60 meV) and high electron mobility (120 cm^2 V^{-1} s^{-1}).[8, 9] It is one of the most intensely studied materials due its strong piezoelectricity, special optical property, and biocompatibility. ZnO has been extensively used for many optoelectronic applications such as light emitting devices and photovoltaic cells.[10, 11] In general, ZnO has three different crystal structures: cubic rock salt, cubic zinc blende, and the most thermodynamically stable hexagonal wurtzite structure. Synthesis of ZnO nanostructures has been conducted on different substrates, including silicon, glass, sapphire, diamond and graphene, by using either wet-chemistry methods, such as sol-gel, hydrothermal and electrochemical methods, or dry synthesis techniques including sputter-coating, chemical vapor deposition, molecular-beam epitaxy, pulsed-laser deposition, and metal organic chemical vapor deposition. ZnO has attracted a lot of attention because of its large variety of nanostructural morphologies, including nanoparticles, nanowires, nanorings, nanotubes, nanowalls, and nanohelix[12] as shown in Figure 1.2. Their superior specific surface areas allow them to be utilized in many applications such as gas sensing, water remediation, biosensing, nanoelectronics, water splitting, and solar cells.[13,14,15,16,17]

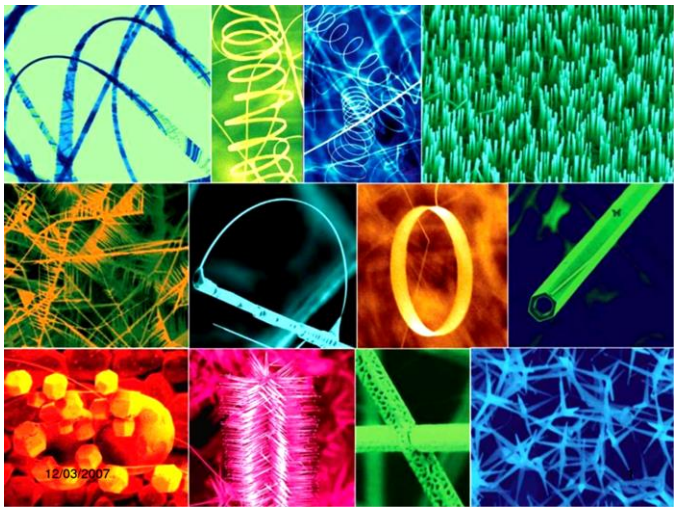

Figure 1.2 Various morphologies of ZnO nanostructured materials.[12§]

§ Reproduced with permission from: Wang, Z. L., Mater. Today 7, 26–33, 2004. Copyright (2004) by Elsevier.

1.3 Nanostructured Transparent Conductive Tin Oxide

Tin oxide (SnO_2) is another popular example of wide-band gap transparent conducting oxides. It is of great interest due to their optical and electrical properties, in addition to their much higher chemical stability compared to other TCOs, which is an essential property for many environmental applications. It is an n-type semiconductor material with a direct band gap of 3.6 eV, and it has the rutile crystal structure with a tetragonal unit cell (p42/mnm).[18]

Similar to other TCOs, SnO_2 has a visible transparency and high electrical conductivity due to the presence of oxygen vacancies that are responsible for electron generation. The presence of oxygen vacancies has been reported in bulk SnO_2.[19,20] Furthermore, their electrical conductivity could be optimized by controlling their oxygen deficiency and/or by doping with different ions. SnO_2 is also well known for its low UV degradation and high thermal stability, which is strongly preferred in photovoltaic applications.[21] Different deposition methods have been used for the preparation of SnO_2 nanostructured films, and they include sputtering, spray pyrolysis, and vapor deposition. Various one-dimensional nanostructures, such as nanobelts, nanowires, and many other hierarchal structures have been employed in various gas sensing and lithium battery storage applications as shown in Figure 1.3.[22,23,24,25,26,27]

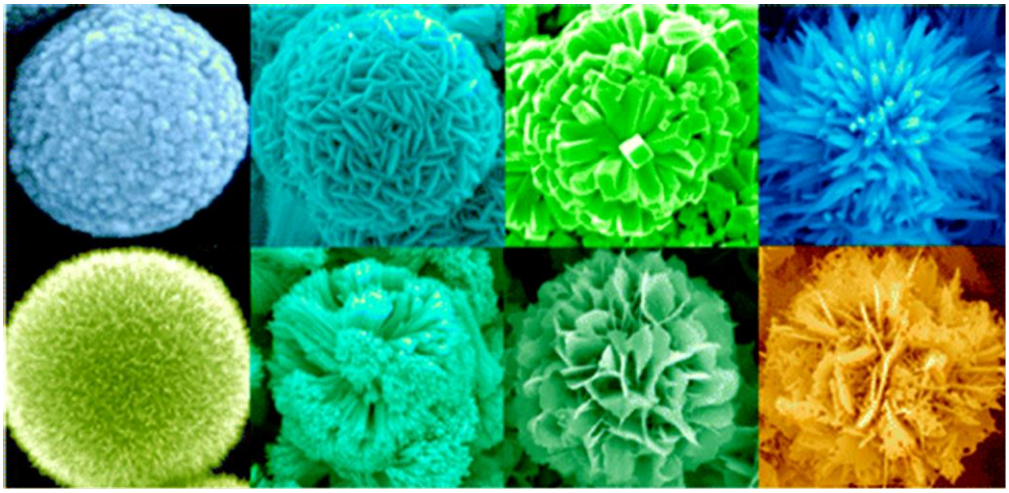

Figure 1.3 Morphologies of various SnO_2 nanostructures. [22**]

** Reproduced with permission from: Wang, H. K. and Rogach, A. L., Chem. Mater. 26, 123-133, 2014. Copyright (2014) by the American Chemical Society.

1.4 Preparation Methods of TCO nanostructures

A large number of techniques have been used for the synthesis of ZnO and SnO_2 nanostructures. They can be generally divided into physical vapor and chemical solution deposition methods.

1.4.1 Physical vapor deposition methods

Many ZnO and SnO_2 nanostructures have been prepared with high-temperature vapor phase growth, which involves reaction between the vapor phase of the desired metal and oxygen gas. Parameters such as the type of substrate, deposition temperature, and oxygen flow rate can be used to control their morphology, dimensions, and crystallinity. The growth mechanisms involved in these vapor deposition methods is either vapor-solid (VS) and/or vapor-liquid-solid (VLS) growth. Two of the most extensively used physical vapor deposition techniques for preparing TCO nanostructures are sputter deposition and pulsed laser deposition.

Sputtering technique is commonly used for large-scale production in industry, where solid targets are bombarded with energetic particles to eject atoms into the gas phase. There are different types of sputtering methods such as direct current (DC) sputtering, which was used, e.g., by Li et al. to obtain SnO_2 nanocrystalline films with different crystallite sizes, [28] and radio frequency (RF) sputtering, as performed, e.g., by Choopun et al. to obtain single-crystalline ZnO nanobelts with cross-sectional size of 10-50 nm and length of several micrometers at a pressure of 40 mTorr on a copper substrate.[29]

The other physical vapor deposition method used for TCO nanostructure preparation is by ablation of the target material of interest by laser irradiation to produce a plasma. Similar to other vapor deposition techniques, the material is vaporized, which enables either VS or VLS growth to form different morphologies on various substrates by controlling such parameters as target-to-substrate separation, gas flow rate, catalyst type, the substrate deposition temperature, and laser power.[30,31,32,33] Pulsed Layer Deposition (PLD) is used in this present work for SnO_2 nanostructures synthesis. However, with the need of lower-temperature fabrication process, many other wet-chemistry methods have emerged as viable alternatives.

1.4.2 Chemical solution deposition methods

Low-cost alternatives for ZnO and SnO_2 nanostructure synthesis compared to physical vapor deposition methods are the wet-chemistry methods, which are based on solution-phase growth. These methods offer a more tunable deposition process with fine control over many parameters under lower temperature growth condition. Among the large number of wet-chemistry techniques, sol-gel and electrochemical depositions are two of the more commonly used preparation methods for ZnO and SnO_2 nanostructures especially for photovoltaic applications.

Sol-gel method was initially developed in 1960s and commonly used for preparing photoanodes for dye sensitized solar cells. In a typical sol-gel process, the material of interest is dissolved in a liquid in order to bring it back as a solid in a controlled manner. The process begins with a sol formation, which is a liquid with insoluble colloidal particles. This is then followed by a gel development, induced by aggregation of the particles and building up of the continuous network.[34] Different semiconductor nanostructures with various morphologies have been prepared using the sol-gel template synthesis.[35,36,37,38,39] However, the main disadvantage of this method is the use of a large quantity of organic solvent, which becomes impractical for large-scale production in industry.

Electrodeposition is one of the oldest synthesis techniques for many metallic, bimetallic, and metal oxide materials that are found in many applications.[40] This technique offers a cost efficient process under a relatively low temperature condition, which is essential for practical large-scale production. A classical electrochemical cell consists of a three-electrode system that contains a working electrode (the substrate), a reference electrode, and a counter electrode (typically a platinum wire).[41] Silicon and conductive glass (glass coated with a thin film of ITO or FTO) are among the more common substrates used as the working electrodes due to their high conductivity and availability. Standard hydrogen electrode, saturated calomel electrode, and silver/silver chloride (Ag/AgCl) electrode are the typical reference electrodes.

Various approaches have been used for metal oxide electrodeposition.[42] Anodic electrodeposition is a simple one-step process that follows the reaction:

$$M^{n+}(aq) + mH_2O \rightleftharpoons M_{n2}O_n(s) + 2mH^+(aq) + ne^-$$

Another approach involves polarizing an electrodeposited metal layer to produce metal ions in an alkaline solution such as NaOH and KOH, in which the hydroxide ions would react with the metal ions to produce metal hydroxide on the substrate surface. Alternatively, nitrates can be used as the counter ions to facilitate the reduction reaction to form the hydroxyl ions in the following reaction:

$$NO_3^-(aq) + 7H_2O + 8e^- \rightarrow NH_4^+(aq) + 10\ OH^-(aq)$$

The hydroxyl ions so produced can then be combined with the metal ions to produce the metal hydroxide. The formation of metal hydroxide on the substrate is usually followed by a second step of dehydration reaction to produce metal oxide:

$$M(OH)_x(aq) \rightarrow MO(s) + H_2O(l)$$

Also, different parameters such as the electrolyte concentration, deposition temperature, and pH of the solution can be adjusted. All of these advantages make electrodeposition one of the most versatile and easy-to-implement synthesis techniques. In this present work, we employed electrodeposition method for growing ZnO and Cu_2O nanostructured thin films.

1.5 Surface Modification of TCO nanostructures

Modification of the surface of different TCO nanostructured materials has recently been studied extensively in order to provide further improvement of their chemical and physical properties appropriate for emerging applications.[43] Most surface modifications of transition metal oxides reported in literature have been carried out with post-processing techniques, including thermal treatment, laser irradiation, and melting impregnation methods.[44,45,46] However, different wet-chemistry methods that offer a more economical approach have been reported to improve TCO nanostructures properties. Some examples include electrochemical or solution processing such as dip coating of TiO_2 nonporous films into an alumina solution.[47, 48,49,50]

Noble metal nanoparticles such as platinum, palladium, gold, and silver have been widely used for enhancing TCO nanostructural properties due to their unique catalytic and plasmonic capabilities.[51, 52, 53, 54] Specifically, metal nanoparticles are employed due to their enhanced optical properties in the visible region for further improvement of the light harvesting capability in solar cells.[55] Briefly, the localized surface plasmon resonance of metal nanoparticles arises when small spherical metallic nanoparticle is excited by light (with a wavelength considerably larger than the size of the nanoparticle). A collective oscillation of the free conduction electrons occurs, where the electron density would change from one side of the nanoparticle to the other side. This redistribution of charge density would create an electric field inside and outside the metal nanoparticle with a direction that is opposite to that of the electric field vector of the light.[56] The resulting resonance between the oscillations and the incident light is known as the localized surface plasmon resonance, as illustrated schematically in Figure 1.4.

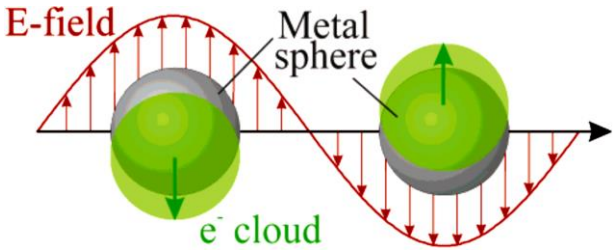

Figure 1.4 Plasmonic surface resonances in spherical nanoparticle when irradiated by light.[56††]

[††] Reproduced with permission: Kelly, K. L., Coronado, E., Zhao, L. L. and Schatz, G. C., J. Phys. Chem. B 107, 668-677, 2003. Copyright (2003) by the American Chemical Society.

A recent review study by Atwater et al. showed the emerging utilization of plasmonic for improved photovoltaics.[57] Different thin-film solar cell systems were explored, focusing on plasmonic light trapping by either light scattering or light concentrating. The light-trapping concept would generally help in reducing the required thickness of the absorber semiconductor material, which would introduce a newly designed solar cell systems with much lower cost. Reducing the active layer thickness would also improve the electrical characteristics of the solar cells due to the reduction of dark current with decreasing semiconductor thickness, which would in turn increase the cell efficiency. Another important factor is the enhancement of charge carrier collection, as the charge needs to only travel a smaller distance before being collected at the junction, which is an important advantage for semiconductor materials with low minority carrier diffusion lengths, such as Cu_2O, Zn_3P_2 and SiC.

Another approach for enhancing the properties of TCO nanostructures for photovoltaics, specifically in dye-sensitized solar cells (DSSCs), is by coating the surface of the TCO nanostructures with another metal oxides such as SiO_2, Al_2O_3 and MgO.[58,59, 60] These insulating oxides would work as a blocking layer to reduce the expected interfacial recombination pathways for improved performance. As explained by Palomares et al. in Figure 1.5, the main idea is to create a barrier layer for interfacial electron transfer processes within the DSSC active layer between TiO_2 and the dye molecules. In a typical DSSC, upon excitation of the dye molecule by light (d), the major electron transfer process occurs through electron injection from the excited state of the dye molecule into the conduction band of TiO_2 (b). However, the excited dye molecule may suffer from decay to their ground state (a), which can affect the process efficiency. The hole transporting material ($3I^-/I_3$ redox couple) is responsible for the dye regeneration process through its electron transfer in the film (e).[61] The role of the insulating layer is to minimize the possible recombination pathways occurring at the TiO_2/dye/electrolyte interface. The injected electrons may recombine with either oxidized dye molecules (c) or the oxidized redox couple (f).[62, 63]

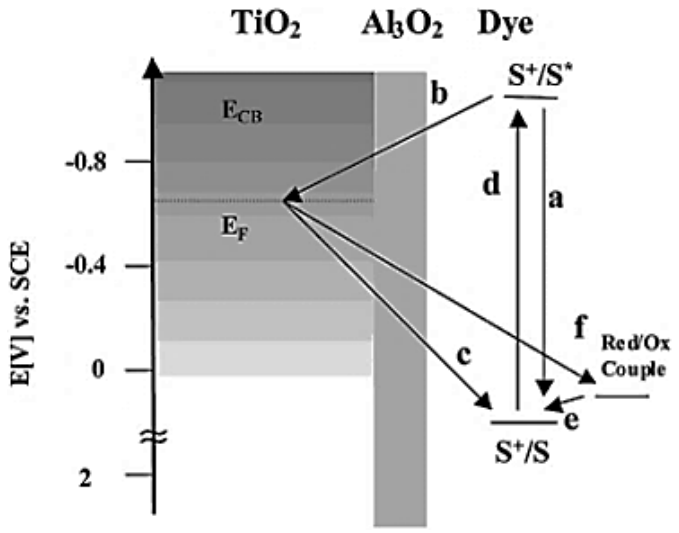

Figure 1.5 Schematic representation of electron transfer processes in dye-sensitized blocking-layer photoelectrode: photogeneration of the dye excited state (d), electron injection into the conduction band of TiO_2 (b), regeneration of the dye ground state by direct decay of the excited state to the ground state (a) and by electron transfer from the redox couple (e), and the charge recombination of injected electron with the oxidized dye molecules (c) and with oxidized redox couple (f).[63‡‡]

‡‡ Reproduced with permission from: Palomares, E., Clifford, J. N., Haque, S. A., Lutz, T., and Durrant, J. R., J. Am. Chem. Soc.125, 475-482, 2003. Copyright (2003) by the American Chemical Society.

1.6 Photovoltaic Applications

The depletion of conventional energy resources such as coal, crude oil, and natural gas has provided the driving force to look for some other alternatives. Since the evolution of solar cell industry in 1990, photovoltaics have rapidly attracted great attention in a number of research areas, all with the common goal to increase the photoconversion efficiency by advancing new material development and device fabrication. According to the European Renewable Energy Council, the demand of renewable energy such as biomass heat, geothermal heat, hydropower, wind power, and solar power have started to increase rapidly since 2010. As shown in Figure 1.6, the contribution of solar photovoltaics is expected to reach 25% in 2040 and to approach 65% in 2100.[64]

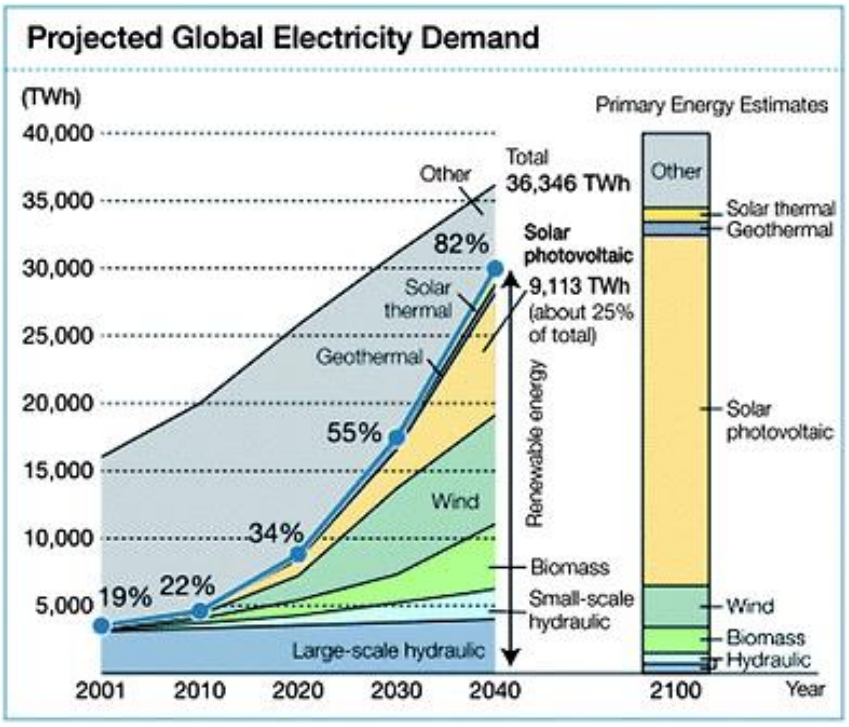

Figure 1.6 Projected global electricity demand based on Renewable Energy Scenario to 2040, published by the European Renewable Energy Council, and reports of the German Advisory Council on Global Change.[64§§]

[§§] Reproduced with permission from: Yu, M., Long, Y. Z., Sun, B. and Fan, Z., Nanoscale 4, 2783-2796, 2012. Copyright (2012) by the Royal Society of Chemistry.

1.6.1 Operating principles of solar cells

In general, the type of material, the number of junctions, and the device structure are used to classify the more common types of solar cells. For example, solar cells can be categorized as inorganic, organic, and hybrid materials according to their material types. A recent study by Kirchartz et al in 2015 also classified solar cells according to their mechanism of charge separation and charge collection. According to their discussion, some photovoltaic systems consist of an active layer, which is responsible for both photon absorption and electron and/or hole transport such as classical silicon based solar cells. On the other hand, some other solar cell systems have a material which is specifically designed for photon absorption and a different material for charge carrier transport. For example, in a DSSC, the dye molecules are the main absorber monolayer due to their high photon absorption in the visible region, while both the TCO nanostructured material and the liquid and/or solid state electrolyte serve as the media for the electron and hole transport.[65] We summarize below the basic processes involved in two of the most common solar cells: inorganic p-n junction solar cell and organic DSSC.

1.6.1.1 Inorganic p-n junction solar cells

The predominant solar cell device structures are p-n and p-i-n junction solar cells. The latter involves the addition of a thin layer of insulator of undoped intrinsic semiconductor (i) that is inserted between the p–type and n–type semiconductor materials.[66] An example of a p-i-n heterojunction structure is given by Meyers, who used a layer of n-CdS deposited on SnO_2-coated glass, followed by a layer of electrodeposited i-CdTe and a p-ZnTe layer at the end, yielding a p-ZnTe/i-CdTe/n-CdS solar cell.[67] Different p-n junction diodes have also been employed in many electronic devices, including light emitting diodes, bipolar junction transistors, and solar cells. The mechanism of a typical p-n junction inorganic solar cell is shown schematically in Figure 1.7. When an n-type material (with a high electron concentration) comes in contact with a p-type material (with a high concentration of holes), they form a p-n junction. Electrons would diffuse from the n-type material to the p-type side, and similarly excess holes would diffuse from the p-type to n-type material. An electric field at the junction is formed, resulting in a depletion region and a built-in potential. Under no external bias condition (Figure 1.7a), the majority charge carriers can diffuse across the depletion region. However, the minority charge carriers that reach the junction could also be swept across the depletion region due to drift. At equilibrium, the diffusion and the drift currents are equal and opposite for both carriers. On the other hand, these currents are not balanced under an external bias.

When the voltage is applied under the forward bias condition (Figure 1.7b), the electric field across the junction is decreased, which leads to an increase in the diffusion current and a smaller depletion layer. However, when a reverse bias voltage is applied (Figure 1.7c), the electric field across the p-n junction is increased, which consequently decreases the diffusion current and leads to a wider depletion layer.[68]

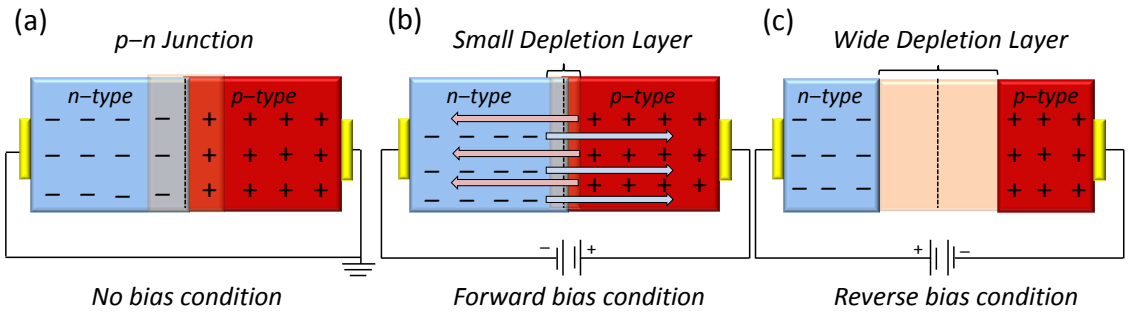

Figure 1.7 Schematic diagram of electron transport mechanism in a typical p-n junction solar cell under (a) no bias condition, (b) forward bias condition, and (c) reverse bias condition.

Recent studies have proposed new nanoarchitectures for building third-generation nanostructure-based solar cells.[69] For example; silicon nanocrystals with an average size of less than 7 nm have been embedded in a SiO_2 or Si_3N_4 matrix in order to take advantage of the quantum confinement effect. Such systems have been prepared by co-sputtering of silicon-rich layers interspersed with stoichiometric SiO_2 layers.[70, 71] Further studies of quantum dot tandem solar cells involving doping silicon quantum dots with boron or phosphorous have been reported to have excellent performance.[72,73] In addition, quantum dot solar cells including, CdS, PbS, Bi_2S_3, CdSe, and InP, that absorb light in the visible region have been employed in photovoltaics.[74] Vera-Marquina investigated annealed CdS nanostructured films for solar cell application because of their enhanced optical properties.[75] However, more abundant materials are generally preferred over these toxic materials in constructing environment-friendly photovoltaic devices. Lower-cost systems such as p-Cu_2O/n-Cu_2O homojunction and p-Cu_2O/n-ZnO heterojunction solar cells have been explored extensively in photovoltaics. McShane et al. studied the effect of junction morphology of the electrodeposited polycrystalline Cu_2O p-n homojunction solar cells with improved efficiency of 0.29% as shown in Figure 1.8.[76] According to their proposal, the p-n junction interface morphology

was expected to depend on the morphology of the p-Cu_2O film that is electrodeposited first. Different conditions used to prepare various morphologies, including the electrolyte composition and pH of the copper lactate solution, were investigated. The highest efficiency was achieved when a low concentration of 0.02 M $CuSO_4$ was used, which ensured a good coverage with uniform Cu_2O crystals and a surface morphology exposing only the (100) plane at the interface. On the other hand, a lower efficiency of 0.08% was obtained at a higher concentration of Cu solution at the same pH, which produced octahedral or cuboctahedral structure with both (100) and (111) planes at the interface. This difference of surface termination would affect the energy level, density, and distribution of interface states at the junction. In the case of the (100)-terminated p-Cu_2O layer, fewer surface states in the interband region were generated, which therefore led to minimized recombination loss at the interface and a higher performance.

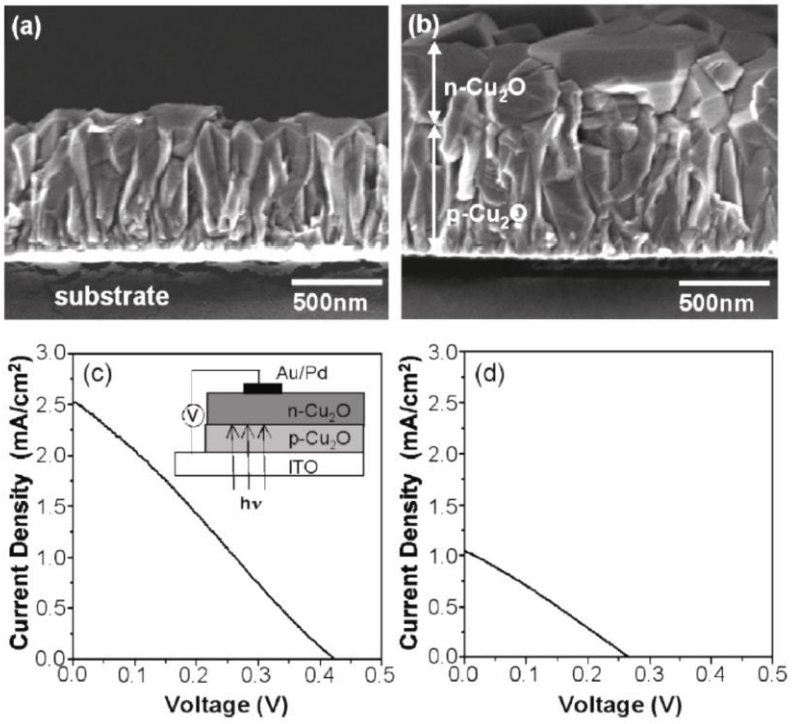

Figure 1.8 Cross-sectional SEM images of (a) p-Cu_2O(type-I) layer and (b) p-Cu_2O(type-I)/ n-Cu_2O homojunction. I-V curves of (c) p-Cu_2O(type-I)/ n-Cu_2O and (d) p-Cu_2O(type-II)/ n-Cu_2O

homojunction solar cells under 1 sun, AM 1.5 illumination. The inset shows a schematic assembly of the p-n Cu_2O homojunction solar cell. [76***]

Recently, many studies show the importance of one-dimensional nanostructured materials for energy conversion process including piezoelectric, thermoelectric, and solar energy harvesting.[77] As an example of a case study, we have chosen a recently published work to illustrate some of the current issues in using these nanomaterials for solar cell application. Chen et al. have succeeded in designing an ordered ZnO/Cu_2O nanoheterojunctions using square-patterned ZnO nanorod arrays that maximized their short current density of 9.89 mA/cm^2 and photon-to-electron conversion efficiency of 1.52%. The aim of their work was to enhance both the light absorption and the charge carrier collection using their properly designed nanostructure that would decrease the charge carrier traveling distance and thus minimize the undesired recombination loss. As shown in Figure 1.9a, their fabrication process was elaborate and it consisted of eight steps; starting with deposition of aluminum-doped zinc oxide and zinc oxide films on glass using radio frequency magnetron sputtering. This step was followed by spin coating a negative photoresist and exposing the substrate using two-beam laser interference lithography system.

Two different patterns of photoresist line and hole templates were obtained and then n-ZnO nanorods were deposited on the templates using a hydrothermal synthesis method. In the next step, the entire photoresist template was removed and a layer of p-Cu_2O was electrodeposited on top of the substrate. Finally, a gold contact was evaporated on the Cu_2O film as the counter electrode. The resulting AZO-ZnO glass covered with large-scale patterned photoresist template was examined optically (Figure 1.9b) and by electron microscopy (Figures 1.9c, 1.9d).

Three different cell structures were fabricated with no-pattern (B1), with line pattern (B2), and with square pattern (B3) of nanorod arrays, and they exhibited overall photon-to-electron conversion efficiencies (PCEs) of 0.67%, 1.34%, and 1.52%, respectively, as shown in Figure 1.10a. Their corresponding external quantum efficiency curves (EQE, Figure 1.10b) also showed enhancement in short-circuit current density, J_{sc}, as illustrated by the broadening of the EQE profiles from B1 to B3 due to more efficient light absorption and greater amounts of charge carrier produced in their active layers. The performance improvement of fabricated square pattern compared to no-pattern ZnO/Cu_2O solar cells is illustrated in Figure 1.10 c, d. For the non-patterned n-ZnO nanorods two-dimensional heterojunction, the photon and the minority carrier pathway were in the same

*** Reproduced with permission from: McShane , C. M. , Siripala , W. P. and Choi, K. S. , J. Phys. Chem. Lett. 1, 2666–2670, 2010. Copyright (2010) by American Chemical Society.

direction and carriers could not be collected effectively due to the larger photon absorption length than the minority carrier drift-diffusion length. On the other hand, for the patterened n-ZnO nanorods three-dimensional ordered nanoheterojunction, the heterointerface was parallel to the light absorption direction and carriers could be collected perpendicularly to the absorption direction, which minimized the conflict between light absorption and carrier collection.[78] Using a similar concept, we investigate, in the present work, the enhancement of our one-dimensional nanostructures with different morphologies to take advantage of their large junction area, better photon absorption and carrier separation/collection. While the ordered geometry and spacing of the aforementioned study helped in understanding the importance of the directed pathway required for effective charge collection, the entire process was complicated. In the present work, we show that we could achieve a comparable performance with significantly less complicated fabrication steps and laborious procedures, thus becoming more practical and less expensive in the eventual commercialization.

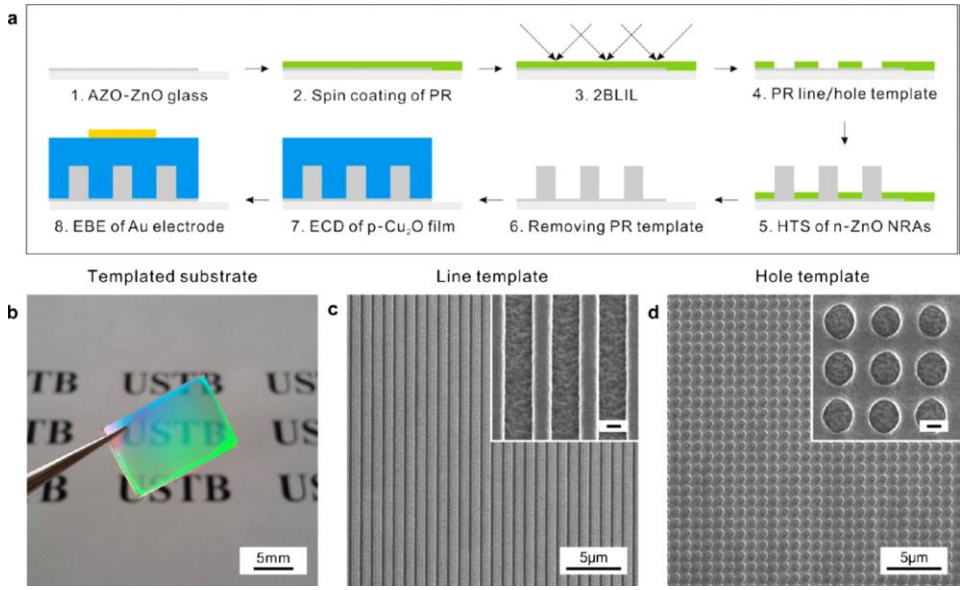

Figure 1.9 (a) Schematic of the fabrication sequence of nanoheterojunction solar cells with Cu_2O on ordered ZnO nanorod array (NRA). This involves deposition of aluminum-doped zinc oxide and zinc oxide (AZO-ZnO) films on glass using radio frequency magnetron sputtering, followed by spin coating a negative photoresist (PR) and exposing the substrate using two-beam laser interference lithography system (2BLIL). Two different patterns of photoresist line and hole templates are prepared and ZnO NRAs are deposited using hydrothermal synthesis (HTS). After removing the PR template, a Cu_2O layer is deposited by electrochemical deposition (ECD), followed by a gold layer on

the top using electron beam evaporation technique (EBE). (b) Optical image of an AZO-ZnO glass covered with patterned PR template. SEM images of the PR templates of (c) lines and (d) holes.[78] †††

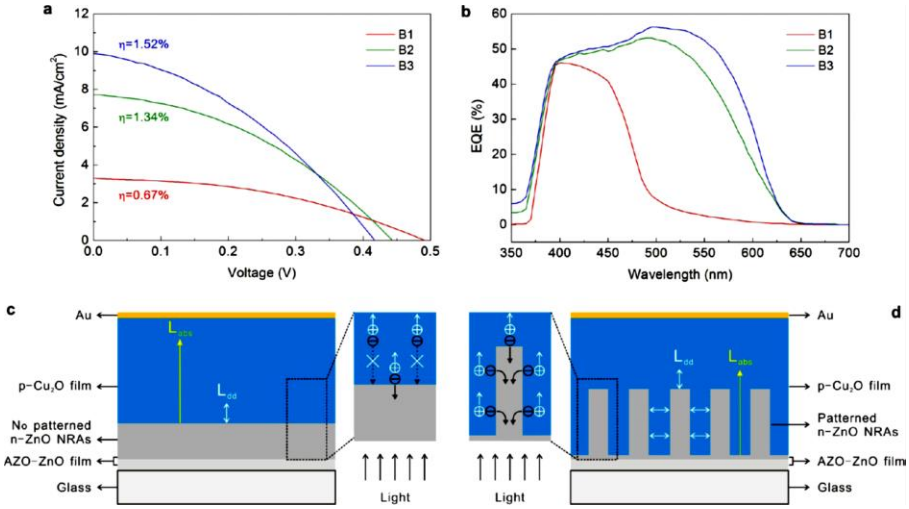

Figure 1.10 (a) Current density vs voltage curves and (b) external quantum efficiency (EQE) spectra of the metal-oxide solar cells based on the ZnO/Cu_2O heterojunctions shown in Figure 1.9. Schematics of the metal−oxide solar cells with (c) non-patterned n-ZnO nanorods two-dimensional and (d) square-patterned n-ZnO nanorods three-dimensional ordered ZnO/Cu_2O nanoheterojunction.[78] ‡‡‡

1.6.1.2 Organic dye-sensitized solar cells

Organic solar cells can be generally classified as polymer-based solar cell and dye-sensitized solar cell (DSSC). According to the type of electrolytes used, DSSCs can be divided into three types: (a) DSSC with a liquid junction electrolyte such as ionic liquid or other organic solvent, (b) DSSC with a quasi solid-state electrolyte such as a polymer electrolyte, and (c) DSSC with a hole-conducting electrolyte such as a p-type semiconductor, e.g. CuI, CuBr, or CuSCN.[79]

The general mechanism for DSSCs with a liquid electrolyte is summarized in Figure 1.11. Upon photon absorption, dye molecules are excited from their ground state to excited state. Electrons in the excited state are then injected into the conduction band of the semiconductor (typically TiO_2). These electrons are transported within the semiconductor material with diffusion toward the back

---

††† Reproduced with permission from: Chen, X., Lin, P., Yan, X., Bai, Z., Yuan, H., Shen, Y., Liu, Y., Zhang, G., Zhang, Z., and Zhang, Y., ACS Appl. Mater. Interfaces 7, 3216–3223, 2015. Copyright (2015) by the American Chemical Society.

‡‡‡ Reproduced with permission from: Chen, X., Lin, P., Yan, X., Bai, Z., Yuan, H., Shen, Y., Liu, Y., Zhang, G., Zhang, Z., and Zhang, Y., ACS Appl. Mater. Interfaces 7, 3216–3223, 2015. Copyright (2015) by the American Chemical Society.

contact (usually ITO), reaching the counter electrode (typically Pt) through the external circuit at the other end. The oxidized dye molecules diffuse through the tri-iodide liquid electrolyte solution where they get reduced and regenerated. Consequently, the electrolyte ions themselves are regenerated near the catalytic active counter electrode and the process repeats itself. The open circuit voltage of the DSSC (Figure 1.11) could be estimated from the potential difference between the Fermi level of the semiconductor material under illumination and the redox potential of the electrolyte. Different parameters, such as semiconductor material morphology, dye design, and the electrolyte properties, can all affect the DSSC efficiency.[79,80]

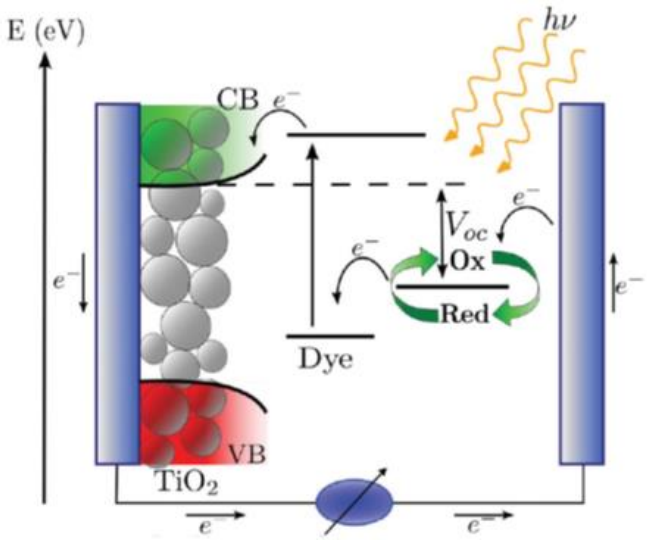

Figure 1.11 Schematic diagram of typical mechanism in a Dye-Sensitized Solar Cell.[80§§§]

There have been extensive studies employing TCO materials with different nanostructure morphologies as the photoanode in DSSC application. TiO_2 is considered the most mature TCO semiconductor used as the photoanode in DSSCs since the first DSSC fabricated by Gratzel and O'Regan in 199l.[81] Nanocrystalline films of TiO_2 have been used extensively, along with different types of commercially available ruthenium-based dyes such as N3, N719, N712, Z907, D149, and black dye.[82] The dye sensitizer must contain functional groups such as carboxylate or phosphate to ensure firm attachment of the dye molecules on the photoanode surface. In addition, the dye

§§§ Reproduced with permission from: Ronca, E., Pastore, M., Belpassi, L., Tarantelli, F., and De Angelis, F., Energy. Environ. Sci. 6, 183-193, 2013. Copyright (2013) by the Royal Society of Chemistry.

molecules should also have high absorption in the visible region.[83, 84, 85] Figure 1.12 shows some of the molecular structures of the commonly used ruthenium complexes including N749, N719, and Z907. In the present work, we have used both N719 and Z907, with maximum absorption at 536 and 542 nm, respectively as shown in Figure 1.13.

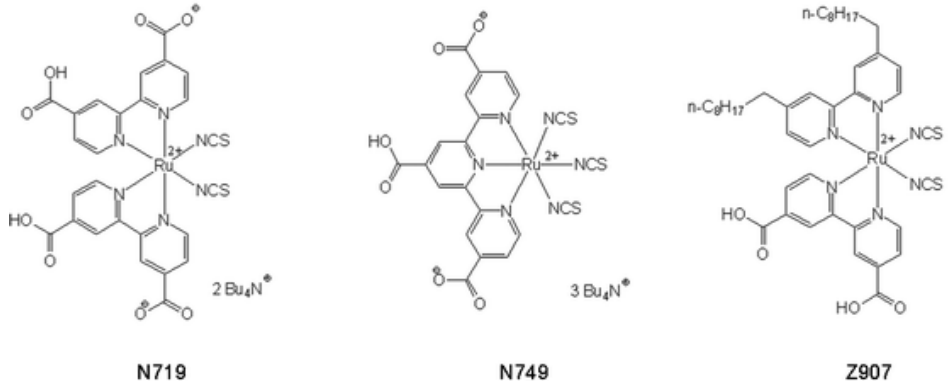

Figure 1.12 Molecular structure of the commonly used ruthenium complexes including N719, N749, and Z907.[82****]

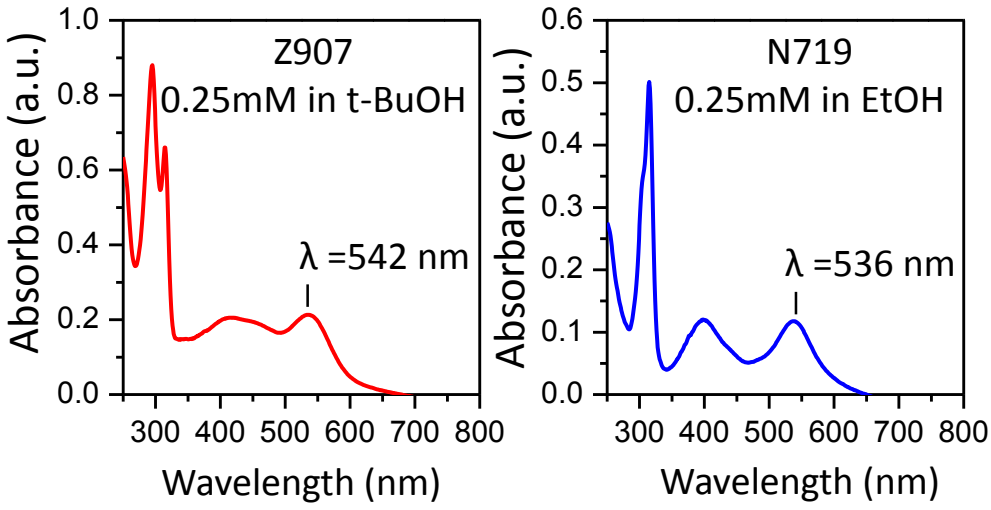

Figure 1.13 UV/Vis absorption spectra of Ru-based dyes Z907 and N719.

**** Reproduced with permission from: Zedler, L., Theil, F., Csáki, A., Fritzsche, W., Rau, S., Schmitt, M. Poppab, J., and Dietzek, B., RSC Adv. 2**,** 4463-4471, 2012. Copyright (2012) by the Royal Society of Chemistry.

Many one-dimensional and hierarchical TiO_2 nanostructured films have been utilized due to their higher specific surface area and preferential electron pathways for efficient charge collection.[86,87] Due to their similar band gap to that of TiO_2 and high absorbance in the UV/Vis region, ZnO and SnO_2 are also considered to be excellent semiconductor photoanodes for DSSC applications.[88] Furthermore, ZnO and SnO_2 have higher electron dynamics characteristics, including their higher electron mobility and larger electron diffusion coefficient, which make them better charge collectors. For instance, the electron mobility of bulk crystal for TiO_2 (1 $cm^2\ V^{-1}\ s^{-1}$) is significantly lower than that for SnO_2 (250 $cm^2\ V^{-1}\ s^{-1}$) and ZnO (300 $cm^2\ V^{-1}\ s^{-1}$).[89] Table 1.3 summarizes some of the more important properties of ZnO and SnO_2 compared to TiO_2.

Table 1.3 Summary of important properties of ZnO and SnO_2 compared to TiO_2.

Property	Crystal structure	Energy band gap (eV)	Electron mobility ($cm^2\ V^{-1}\cdot s^{-1}$)	Refractive index
TiO_2	Rutile, anatase, and brookite	3.0-3.2	0.1-4	2.5
ZnO	Rocksalt, zinc blende, and wurtzite	3.2-3.4	300	2.0
SnO_2	Rutile tetragonal	3.6-3.8	250	2.0

ZnO and SnO_2 are well known for the wide varieties of their nanostructures, which have been employed as photoanodes for DSSC application. In particular, their various highly branched morphologies with large specific surface areas and superior dye-loading capabilities are expected to produce higher photon absorption.[90,91] Recently, Kang et al. employed a novel tri-layered ZnO nanostructure shown in the schematic diagram (Figure 1.14a) and SEM image (Figure 1.14b) and they obtained a high efficiency approaching 3.21%. Three different DSSC structures based on different ZnO photoanode morphologies have been investigated, and these include (Cell 1, Figure 1.13c) mono-layered ZnO one-dimensional nanowire arrays, (Cell 2, Figure 1.13d) double layers of

nanowire arrays decorated with smaller ZnO microspheres, and (Cell 3, Figure 1.13e) triple layer structure consisting of a layer of hierarchical ZnO large microspheres on a one-dimensional nanowire array with smaller microspheres as the intermediate layer. The corresponding current density-voltage characteristic and the incident photon-to-electron conversion (IPCE) spectra showed that Cell 3 with the higher surface area tri-layered ZnO photoanode exhibited the highest light harvesting capability due to their higher dye absorption/loading and their excellent light scattering properties.[92] In the present work, we employ ZnO and SnO_2 nanostructures with similar high surface area as photoanodes and we show that comparable efficiencies can be achieved in DSSCs fabricated with less complicated device structures.

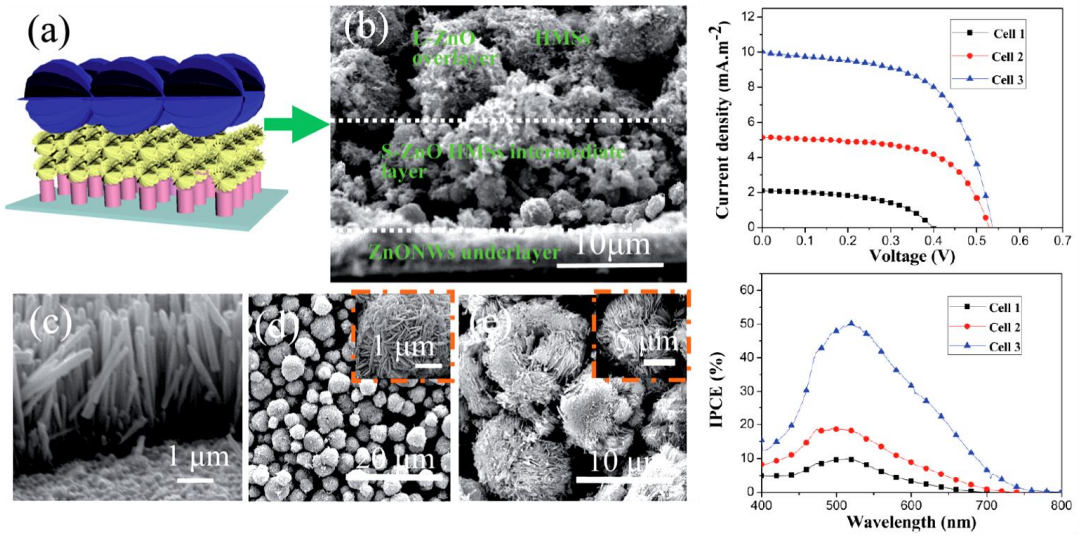

Figure 1.14 (a) Schematic diagram of the tri-layered ZnO photoanode. SEM images of (b) the tri-layered ZnO photoanode, (c) ZnO base layer of nanowires, (d) small ZnO hierarchical microspheres, and (e) large ZnO hierarchical microspheres. Right panels show their corresponding photocurrent density vs. voltage profiles and incident photon-to-electron conversion efficiency (IPCE) spectra of DSSCs based on different photoanodes.[92††††]

†††† Reproduced with permission from: Kang, X., Jia, C., Wan, Z., Zhuang, J., and Feng, J., RSC Adv. 5, 16678-16683, 2015. Copyright (2015) by the Royal Society of Chemistry.

1.7 Scope of Thesis

The general objective of the present work is to prepare nanostructured transparent conductive oxides with different nanostructured morphologies and to exploit their properties for photovoltaic applications. In this chapter (Chapter 1), we present a short introduction to TCO nanostructures and their unique properties. A brief literature review focusing on both the more common physical vapour deposition and chemical solution synthesis methods to produce ZnO and SnO_2 nanostructures is given. An overview about photovoltaics and the operating principles of two of the most common solar cells (inorganic p-n junction solar cell and organic DSSC) that are used in the subsequent Chapters is also presented. In Chapter 2, we briefly describe the experimental procedure used to synthesize TCO nanostructured materials and the characterization techniques used for studying their morphologies and crystal structures, and chemical-state composition properties. Different characterization techniques for investigating the optical, electrical, and photovoltaic properties of the fabricated devices are also given

We present our data in the next four chapters. In Chapter 3, we describe the synthesis of ZnO nanotubes, obtained by direct electrochemical deposition for the first time. We further investigate the delicate control of electrolyte conductivity needed in producing the desired morphology of these one-dimensional ZnO nanostructures, along with a detailed study of the resulting morphology, crystal structure, and chemical-state composition arising from manipulating other growth parameters, including electrolyte concentration, deposition temperature, and deposition time.

Chapter 4 presents the fabrication of low-cost p-Cu_2O/n-ZnO nanorod and nanotube heterojunction devices using an "all-electrodeposition" method. By electrodepositing ZnO nanorods or nanotubes as an active n-type TCO material, we construct a classical p-n junction solar cell by incorporating electrodeposited Cu_2O film as a p-type semiconductor material. Full characterization has been performed for the resulting solar cell performance, with emphasis on the performance correlation with the growth parameters of the prepared nanostructures.

In Chapters 5 and 6, we present studies of dye sensitized solar cells using photoanodes based on ZnO nanotubes and SnO_2 hierarchal nanostructures, respectively. The high surface areas of these ZnO and SnO_2 nanostructure are expected to produce enhanced dye loading capacities and improved charge carrier collection with much higher electron dynamics, when compared to typical TiO_2

photoanodes. We also perform additional modifications by loading metal nanoparticles to further maximize photon absorption in the visible region by taking advantage of their surface plasmonic effect. In addition, coating the as-grown nanostructures surface with an optimized passivation layer is used to minimize the undesirable recombination loss and to enhance their overall performance. Finally, we summarize, in Chapter 7, our conclusions and comment on future work.

Chapter 2
Experimental Details

In this chapter, we outline the experimental techniques used for synthesis and characterization of TCO nanostructured materials, as well as performance evaluation of prototype solar cells fabricated using the as-grown nanomaterials. A brief description of each of the relevant methods follows.

2.1 Electrochemical Methods for Synthesis and Characterization

2.1.1 Cyclic voltammetry (I vs V) and potentiostatic amperometry (I vs t) for synthesis of nanostructured materials

All samples are investigated and prepared by electrodeposition of metal ions from their freshly prepared primary electrolytes in a water bath kept at constant temperature using amperometry technique conducted in a three-electrode system. Amperometry generally refers to all electrochemical techniques in which a current is measured as a function of either time (potentiostatic amperometry) or applied electrode potential (voltammetry).[93] In our work, we perform potentiostatic amperometry where current is measured at a constant potential with variation of the deposition time for TCO nanostructure synthesis. An electrochemical station (CH Instruments 1140) is used is connected to an ITO/glass substrate as the working electrode and a platinum wire as a counter electrode, with the potential kept fixed with respect to an Ag/AgCl reference electrode, as shown in Figure 2.1. In an electrodeposition process, the standard potential of the metal ions of interest is applied to the working electrode in a primary electrolyte solution, which reduces the metal ions to their metallic structure. Supporting electrolyte such as KCl is added to enhance the conductivity of the primary electrolyte.

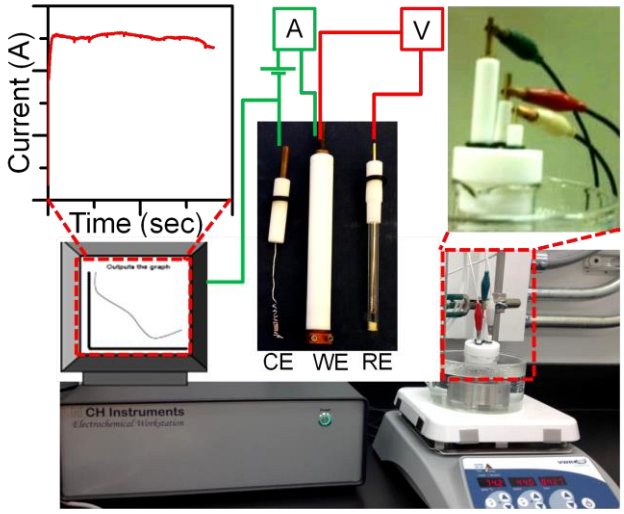

Figure 2.1 Photograph of an electrochemical station (CHI 1140) connected to a three-electrode electrochemical cell in a typical electrochemical deposition setup. The working electrode (WE) is the sample used for the electrodeposition, in the presence of a Pt wire counter electrode (CE) and an Ag/AgCl reference electrode (RE).

Prior to any deposition, the oxidation and reduction potentials of the primary electrolyte are determined by performing a current (I) vs potential (V) sweep in the cyclic voltammetry technique. In cyclic voltammetry (CV), the potential is increased linearly from an initial potential to a final potential (forward scan) and then decreased from the final potential back to the initial potential (reverse scan) while measuring the current, this cycle is then repeated as needed. For example, the measured cyclic voltammogram in a 10^{-3} mol L^{-1} $K_4[Fe(CN)_6]$ and 0.1 mol L^{-1} KNO_3 electrolyte used for determining the oxidation and reduction potentials of Fe ions is shown in Figure 2.2.[94,95] The oxidation potential is found at the first potential sweep going in the positive direction (forward scan), where the hexacyanoferrate(II) ions are oxidized to hexacyanoferrate(III) at the working electrode. In the following reverse sweep from positive to negative potentials, the hexacyanoferrate(III) ions formed in the forward scan are reduced back to hexacyanoferrate(II). Consequently, the standard electrode potentials at which any metal ions are reduced to their respective zero-valent metals can be determined from their corresponding CV profiles. In addition, electrolyte concentration, deposition temperature, and deposition time are experimental parameters that are varied according to different materials of interest. Details about specific experimental conditions are given in the experimental parts of Chapters 3-6, where applicable.

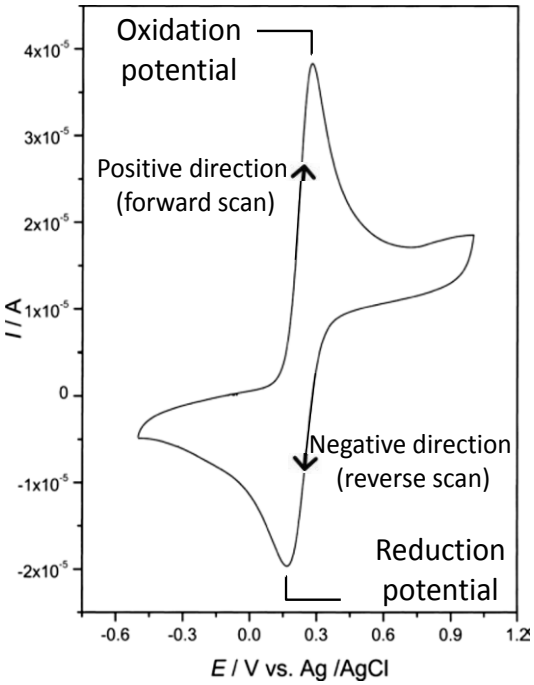

Figure 2.2 Cyclic voltammogram (fifth cycle) obtained in a solution containing 6.25×10^{-3} mol L^{-1} $K_4Fe(CN)_6$ and 0.5 mol L^{-1} KNO_3, with a scan rate of 20 mV s^{-1}. [95] ‡‡‡‡

2.1.2 Electrochemical impedance spectroscopy

Electrochemical Impedance Spectroscopy (EIS) is a powerful technique developed for characterization of electrical properties of different materials, including conductors, semiconductors and even insulators. [96] In general, EIS measures the dielectric properties of a medium as a function of frequency. In the case of an ideal resistor, the resistance can be calculated using Ohm's law in terms of the ratio between the voltage E and the current I, where R = E/I. However, in the real world there are different types of resistance for more complex systems, in which case we use impedance. The electrochemical impedance is calculated by measuring the current through the cell when an AC potential is applied at different frequencies, *f* (Hz). Typically, the current response to a sinusoidal potential is also sinusoid at the same frequency but with a phase shift. The change in potential E_t at time (t) is related to the maximum potential E_0 as a function of the radial frequency ω (radian/second), as follows:

‡‡‡‡ Reproduced with permission from: Scholz, F., and Bond, A. M. Electroanalytical Methods Guide to Experiments and Applications. 2nd, New York, Springer, 2010. Copyright (2010) by Springer.

$E_t = E_0 \sin(\omega t)$,

where, $\omega = 2 \pi f$.

On the other hand, the current at time t (I_t) is shifted in phase and is related to the maximum current (I_0) according to:

$I_t = I_0 \sin(\omega t + \phi)$, where φ is the phase shift.

Consequently, the impedance of the system (Z) is calculated as follows:

$Z = E_t / I_t = E_0 \sin(\omega t) / I_0 \sin(\omega t + \phi) = Z_0 [\sin(\omega t)/\sin(\omega t + \phi)]$,

where $Z_0 = E_0/I_0$. The impedance is also can be expressed as a complex number for calculating the real part (Z_{re}) and imaginary part (Z_{im}) of the impedance at different frequencies, where

$Z(\omega) = E/I = Z_0 \exp(j \phi) = Z_0 (\cos \phi + j \sin \phi)$, where $j = \sqrt{(-1)}$.

As different working electrodes are employed for photovoltaic application, the determination of electrical resistance of the nanomaterials deposited on the substrates is important to understanding the performance of the solar cells. Typical solar cells are commonly simulated as an equivalent circuit for better quantification of the effects of different parameters that are crucial for improving the cell performance. The most common model is the simplified Randles equivalent circuit model, which consists of a solution resistance (R_s), a double layer capacitor (C_{dl}), a charge transfer resistance (R_{ct}), and Warburg impedance element (Z_W). In this model, the double-layer capacitance is in parallel with the charge-transfer resistance, as shown in Figure 2.3.

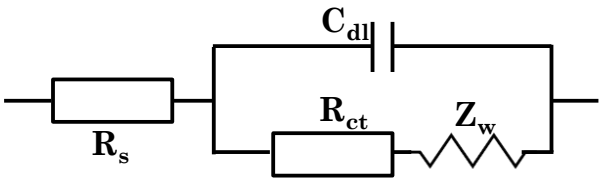

Figure 2.3 Schematic diagram of the simplified Randles equivalent circuit.

In any electrochemical cell, solution resistance is an important factor during the deposition process. The impedance of an electrochemical cell could be due to the solution resistance between the counter and reference electrodes or between the reference and working electrodes. There are many

parameters that affect and contribute to the solution resistivity (R_s) and they generally include electrolyte ion type, electrolyte concentration, and deposition active surface area.

In addition, as ions diffuse in an electrolyte solution, they could be adsorbed onto the electrode surface forming a double layer. The existence of this electrical double layer at the interface would separate the ions from the charged electrode by an insulating space, forming a capacitor (C_{dl}). Many parameters, such as ionic concentration, electrode potential, and impurity adsorption, could affect the magnitude of the capacitor.[97,98]

Another type of resistance that exists in the electrochemical cell is the charge transfer resistance (R_{ct}), which occurs when the electrons enter the electrolyte solution and the metal ions start to diffuse into the electrolyte after their dissolution according to: $M \leftrightharpoons M_n^+ + ne^-$. This type of resistance is our main interest in order to characterize the as-prepared photoanodes charge transfer process efficiency.

Finally, the Warburg impedance (Z_w) element represents the mass transfer resistance used in the equivalent circuit model. In contrast to electrolyte resistance (R_s) and double layer capacitance (C_{dl}), the Warburg impedance (Z_w) is a non-ideal circuit element as it changes with the frequency, ω. However, the identification of Z_w is difficult because it is always accompanied with the charge-transfer resistance and double-layer capacitance.

As the majority of electrochemical cells do not have a uniform current, leading to the urgent need for EIS mathematical representation that can be fitted theoretically to a simulated model. Nyquist plot is the conventional mathematical data representation for resistance quantification. Typically, the imaginary part of impedance Z_{Im} is plotted against the real part Z_{Re} at different values of frequencies ω. In a standard Nyquist plot, the semicircle portion at higher frequencies corresponds to electron transfer limited process, figure 2.3 shows the Nyquist Plot for an equivalent circuit with $R_{ct} = 100\ \Omega$, where the charge-transfer resistance can found by reading the real axis value at the high frequency intercept.[93]

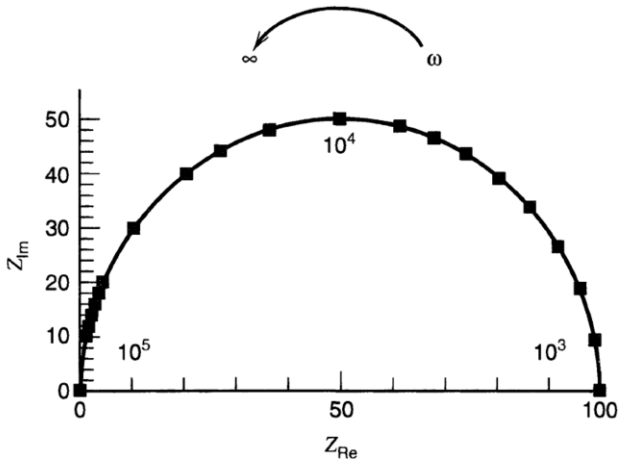

Figure 2.4 Nyquist plot for an equivalent circuit with R_{ct} = 100 Ω. [93§§§§]

[§§§§] Reproduced with permission from: Bard, A. J., and Faulkner, L. R. Electrochemical Methods: Fundamentals and Applications. 2nd, New York, John Wiley, 2001. Copyright (2001) by John Wiley.

2.2 Characterization of Physical Structures

The morphologies and crystal structural information of TCO nanostructures have been extensively studied by using several advanced materials characterization techniques.

2.2.1 Scanning electron microscopy

Scanning electron microscopy (SEM) is one of the major techniques used for surface morphology analysis.[99] Different models of Zeiss microscopes are used in this present work including, LEO FESEM 1530, Ultra Plus FESEM, and Merlin FESEM. Figure 2.5 shows the Zeiss Merlin microscope equipped with a field-emission electron source and a Gemini-II electron optics column. This state-of-the-art electron microscope is capable of high performance at an extremely low acceleration voltage and a high spatial resolution of less than 0.8 nm (at 20 kV). This microscope is also equipped with an EDAX Energy Dispersive X-ray Spectroscopy (EDS) system with a solid-state detector for elemental analysis of the near-surface (down to about 1-2 micrometers).[100] When an accelerated focused beam of electrons is scanned across the sample with a typical spot size of 1 nm, the secondary electrons (SEs), with kinetic energy less than 50 eV, so generated can be used to construct an image that closely reflects the surface morphology. Different types of secondary electrons (containing different surface information) can be detected by positioning a Everhart-Thornley type SE detector inside the electron column (in-lens detector) and outside the electron column (SE2 detector), which are sensitive to SE1 and SE2 electrons, respectively. SE1 and SE2 electrons are secondary electrons that are generated, respectively, directly upon a single high-energy incident electron impact and indirectly upon multiple electron collisions near the surface. The high-energy electrons can also interact much more directly with the sample, which lead to electronic excitations. The subsequent inelastically backscattered electrons (corresponding to incident electrons that suffer an energy loss and with kinetic energy greater than 50 eV) contain information about the excited electronic states and are therefore element-specific. The backscattered electrons are detected with an energy-filtered backscattered (EsB) detector. The high-energy electrons also excite the core-shell electrons to unoccupied electronic states in the sample. The subsequent de-excitation through a radiative decay pathway provides the basic principle of EDS. By detecting the X-ray emission at element-specific, characteristic photon energies, it is possible to quantitatively identify the elemental compositions of the sample.

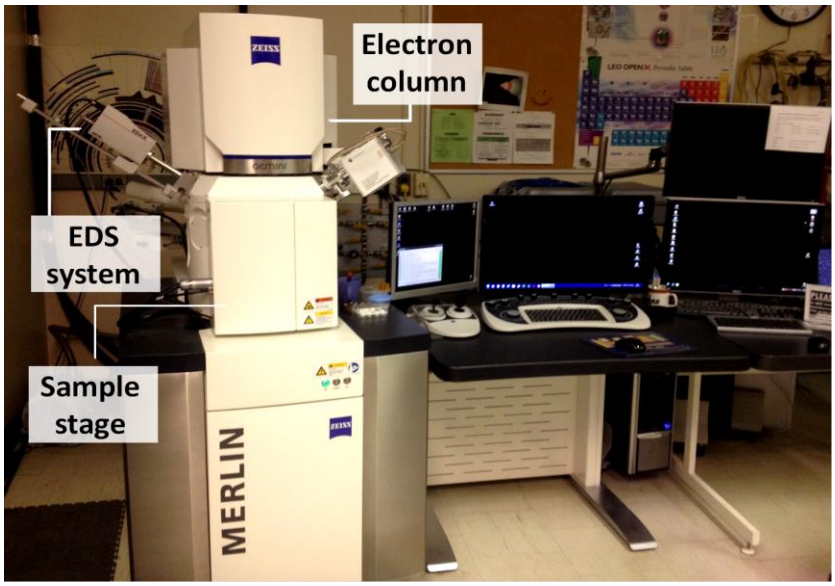

Figure 2.5 Photograph of the Zeiss Merlin field-emission scanning electron microscope, equipped with both in-lens and out-of-lens secondary electron detectors, an energy-selective backscattered (EsB) detector, and an EDAX energy-dispersive X-ray analysis system.

2.2.2 Helium ion microscopy

Helium ion microscopy (HIM) is a new type of scanning charged-particle-beam microscopy that is based on a high-energy, finely focused He^+ beam for surface morphology characterization.[101] Figure 2.6 shows a Zeiss Orion Plus microscope that is capable of an ultrahigh spatial resolution of 0.24 nm due to the short de Broglie wavelength of the helium ions. A proprietary gas ion source is used to generate a focused beam of He^+ ions by field ionization of He gas by a cryogenically cooled, atomically sharp tungsten tip at high bias (≈ 25 kV).[102,103] A special procedure is used to obtain the atomically sharp, trimer tip and the He^+ ions are formed at one of the three atoms in the trimer. The He^+ ion beam is accelerated, focused and directed to scan over the sample surface. The high energy He^+ ion impact produces secondary electrons, which are collected by an Everhart-Thornley detector to build up a HIM image. An additional microchannel plate detector is used to detect backscattered ions, which can be used to provide elemental contrast based on the atomic number of element in the sample. The advantage of HIM is the much shorter de Broglie wavelength of the He^+ ions compared to electrons (at the same kinetic energy), and is not affected by any diffraction effects, which is a limiting factor in most traditional SEMs arising from the wave-like properties of the electron. [101] This leads to not only significantly better spatial resolution but also considerably larger depth of focus.

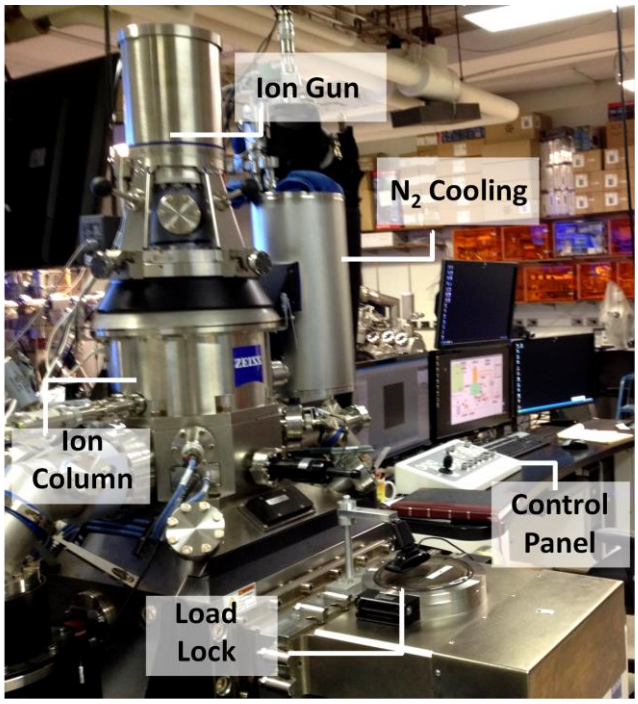

Figure 2.6 Photograph of a Zeiss Orion Plus helium ion microscope.

2.2.3 Transmission electron microscopy

Transmission electron microscopy (TEM) measurements have been performed for detailed crystal structure investigation and surface planes identification of TCO nanostructures.[104] In TEM, a high-energy (200 kV) electron beam interacts directly with the sample when it passes through an ultrathin specimen (usually less than 100 nm thick). In the present work, all the electrodeposited TCO samples have been scraped off from the substrates and transferred onto carbon TEM grids. Both bright-field, low-magnification and high-resolution TEM studies have been conducted by using a Zeiss Libra 200 MC microscope, shown in Figure 2.7.[105]

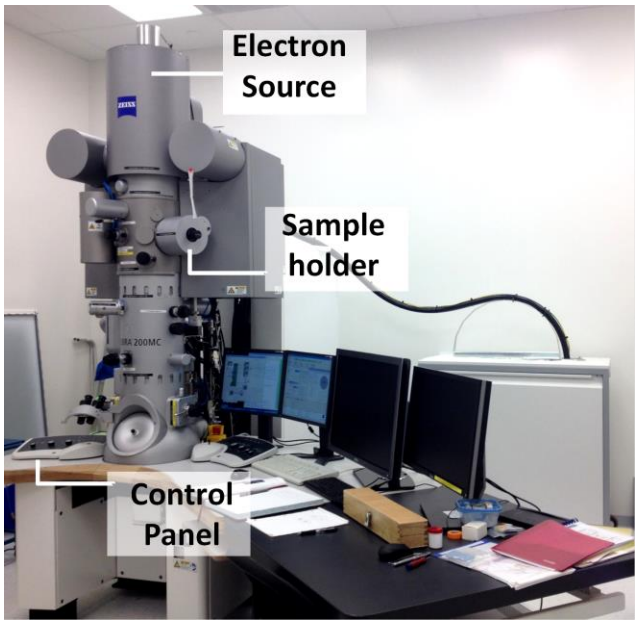

Figure 2.7 Photograph of a Zeiss Libra 200 MC transmission electron microscope.

2.2.4 X-ray diffraction crystallography

X-ray diffraction (XRD) is not a surface-sensitive technique but is a powerful tool for bulk crystallography as a hard X-ray beam could penetrate deep into the materials in order of micrometers.[106] In the present work, the as-prepared nanostructured films are usually present in a very small amount on top of the substrates (signals from the latter would overwhelm the diffraction patterns), a glancing-incidence geometry is needed in order to maximize the signal intensity of the nanostructured films and to minimize those from the substrates. This type of evanescent diffraction provides a penetration depth less than 100 nm, where the diffracted intensities are measured by scanning a detector in a plane parallel to the surface in the so-called in-plane diffraction mode.[107] With the incidence angle of the X-ray beam kept at a very shallow angle (close to the critical angle of the sample), the detector is swept over the 2θ angle. In the present work, we use glancing-incidence X-ray XRD in a PANalytical X'Pert Pro MRD diffractometer with Cu Kα radiation (1.54 Å) at an incidence angle ω less than 1° to determine the crystal structures of the nanostructured material, as shown in Figure 2.8. Although the ITO/glass substrate has very strong peaks, this configuration increases the detectable intensity of the nanostructured material significantly.

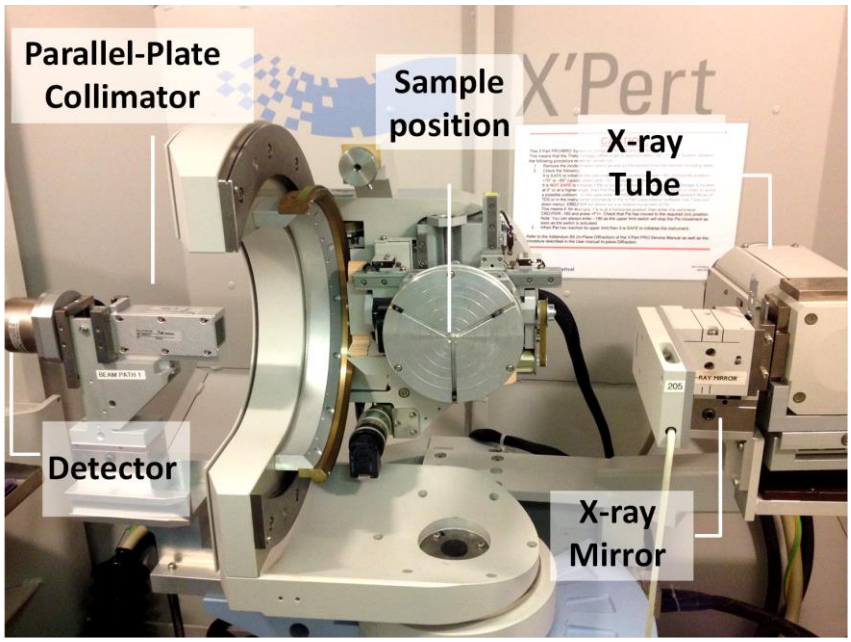

Figure 2.8 Photograph of the Panalytical X'pert Pro MRD X-ray diffractometer used for crystal structure characterization of the as-prepared nanomaterials. The instrument is set up in the parallel beam geometry with an X-ray mirror and a parallel plate collimator used for the incident and diffracted beam optics, respectively.

2.3 Chemical Composition and Elemental Analysis

Two major techniques have been used for chemical composition analysis of the as-prepared materials, and they are Scanning Auger Microscopy (SAM) and X-ray Photoelectron Spectroscopy (XPS).[108] The latter is also known as Electron Spectroscopy for Chemical Analysis (ESCA). Figure 2.9 illustrates schematically the basic processes involved in the production of characteristic X-rays (as detected in EDS in SEM), Auger electrons (as detected in SAM), and photoelectrons (as detected in XPS). In a typical SEM or SAM process, a high-energy beam of electrons is directed at the sample (Figure 2.9a) and the incident electrons are scattered elastically and inelastically. When the incident electron with a kinetic energy of (E_0) is scattered inelastically, the scattered electron would suffer an energy loss, resulting in a lower kinetic energy: $E_s = E_0 - E_{loss}$. If the energy loss suffered by the inelastically scattered electron is sufficiently large, an electron from a core level of the sample is ejected, creating an excited ionic state, in an electron-impact ionization process (Figure 2.9b). Two deexcitation pathways are possible for the excited ionic state. In a direct radiative decay or an X-ray emission process (Figure 2.9c), an electron from a higher energy level fills the core hole, releasing an

X-ray photon (corresponding to the difference in the two energy levels). In an indirect radiationless decay or Auger emission process (Figure 2.9d), an electron from a higher energy level fills the core hole while the energy release is sufficient to eject a second electron, called the Auger electron that carries the remaining excess energy. An excited ionic state can also be created by the absorption of an X-ray photon when the sample is bombarded by X-ray photons in a resonant photoabsorption process (Figure 2.9e). The subsequent deexcitation by emission of an electron from either the core or valence levels of the sample produces the photoelectron (Figure 2.9f).[109]

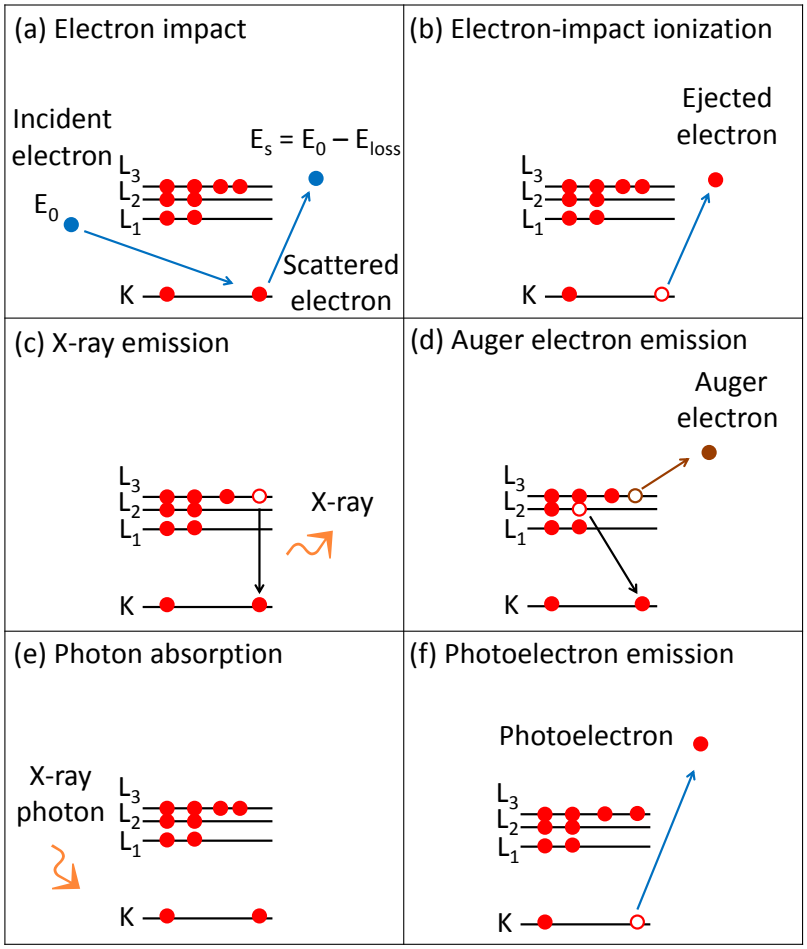

Figure 2.9 Schematic illustrations of (a) high energy electron impact process, (b) removal of an core-level electron leading to an excited ionic state, (c) deexcitation by characteristic X-ray emission, and (d) deexcitation by Auger electron emission, (e) resonant absorption of an X-ray photon and (f) deexcitation by emission of a photoelectron.

2.3.1 Scanning auger microscopy

A Thermo MicroLab 350 Microprobe, capable of a high lateral resolution of 5 nm in SEM mode and 15 nm in SAM mode, shown in Figure 2.10, is used to conduct SAM analysis. A focused beam of high-energy electrons is generated in a field-emission electron source coupled to an electron optics column. Upon high-energy electron impact ionization of the sample, an excited ion state with a core hole is created (Figure 2.9b), and the excited ion state undergoes deexcitation via Auger decay (Figure 2.9d). The emitted Auger electrons possess kinetic energies characteristic of the differences in the energy levels of the sample involved and can therefore be used as a fingerprint, similar to X-ray emission lines used in EDS (Figure 2.9c). The Auger spectrum is usually plotted in intensity derivative mode as a function of the kinetic energy of the detected electrons.[110] Auger electron spectra can be collected point by point over the entire sampling area of interest and the selected Auger features of interest can be used to construct elemental maps. As the kinetic energy of the Auger electron usually falls within 50 and 2000 eV, at which the inelastic mean free path is the shortest (~2 nm), SAM is therefore extremely surface-sensitive, in contrast to EDS (with a typical probe depth of 400-1000 nm).[111]

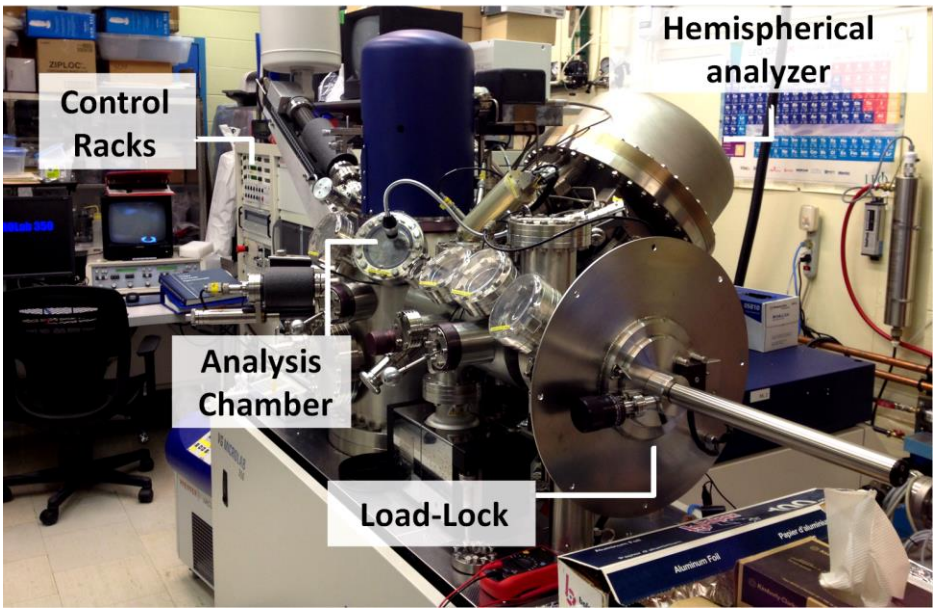

Figure 2.10 Photograph of a Thermo MicroLab 350 Microprobe used for elemental analysis of nanostructured materials.

2.3.2 X-ray photoelectron spectroscopy

The chemical-state compositions of nanostructured materials are analyzed by X-ray photoelectron spectroscopy (XPS) using a Thermo-VG Scientific ESCALab 250 Microprobe with a monochromatic Al K_α source (1486.6 eV), as shown in Figure 2.11. In XPS, a photon beam of monochromatic Al K_α radiation is focused onto the sample (Figure 2.9e), leading to the emission of photoelectrons from their surface (Figure 2.9f). The kinetic energy of the photoelectrons is measured by using a hemispherical electron energy analyzer. The corresponding binding energy is calculated using the Einstein equation, as follows:

$$E_{binding} = E_{h\upsilon} - (E_{kinetic} + \varphi)$$

where $E_{binding}$ is the binding energy of the electron, $h\nu$ is the energy of the X-ray photons (i.e. 1486.6 eV for Al K_α; h is the Planck's constant and ν is the light frequency), $E_{kinetic}$ is the kinetic energy of the photoelectron as measured by the analyzer, and φ is the work function dependent on both the spectrometer and the material.[112]

Because of the short inelastic mean free path of the photoelectrons with the kinetic energy range of interest (<10 nm), XPS is a very surface-sensitive technique. Using an Argon ion source to sputter away materials interleavingly between XPS spectral measurements, i.e. XPS depth profiling, it is possible to follow the chemical-state composition change as a function of sputtering depth and thereby in the depth direction in the near-surface region of the sample.

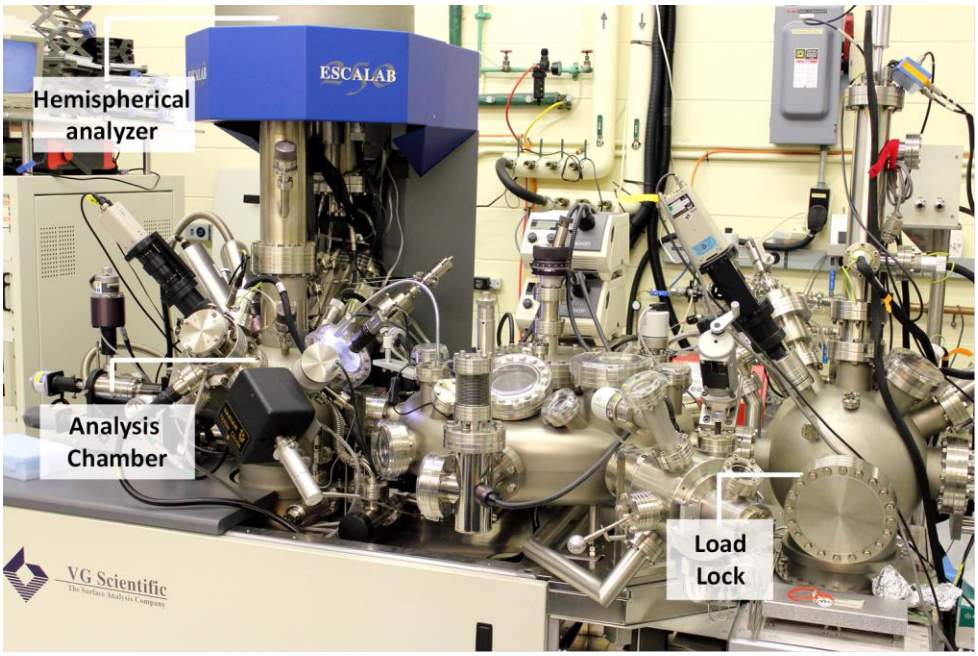

Figure 2.11 Photograph of the Thermo-VG Scientific ESCALab 250 Microprobe used for chemical-state quantification of nanostructured materials.

2.4 Characterization of Electrical and Optical Properties

2.4.1 Conductive atomic force microscopy

The prepared thin film topography and their diode behavior have been investigated by conductive atomic force microscopy (C-AFM) in an Asylum Research Cypher S-AFM microscope. In a typical C-AFM, the sample surface is scanned at a preselected sample-to-tip separation by using a conductive (Ti-Ir) tip, where a voltage is applied between the tip and the sample.[113] The current vs voltage curve so obtained would identify the as-grown diode electrical property of the material. A topography image is generated, which can give detailed information for identifying specific locations on sample surface with different conductivity. The main advantage of this technique is their high spatial resolution (<10 nm) with an excellent capability of measuring currents from ~1 pA to 20 nA, which can be used to identify any local shunting that may occur.[114]

2.4.2 Hall Effect measurements

For resistivity and carrier concentration measurements, a Hall effect measurement system (Ecopia HMS- 5300) employing the four-point probe method in a van der Pauw configuration is used, as shown in Figure 2.12.[115] Gold contacts are sputter-deposited by magnetron sputtering (with a current of 50 mA for 120 s) onto the corners of the electrodeposited nanostructured materials on ITO/glass substrates.

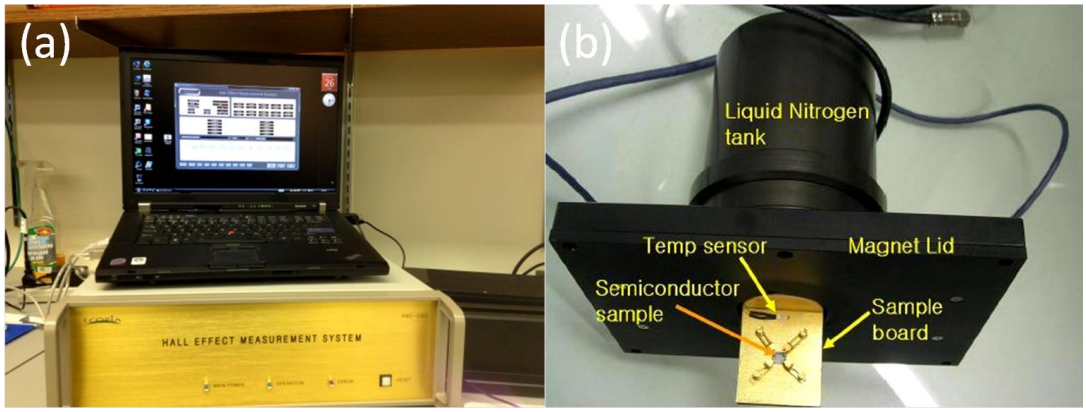

Figure 2.12 (a) Photograph of the Ecopia HMS-5300 Hall effect measurement system, (b) sample mounting fixture with upper cooling reservoir.

2.4.3 Ultra-Violet/Visible (UV/Vis) spectroscopy

The optical properties of the as-prepared materials including their light absorbance and reflectance are investigated by using a UV/Visible spectrophotometer (Perkin-Elmer Lambda 45) with a wavelength range of 190-1100 nm and a variable bandwidth of 0.5-4 nm, and with a monochromator for reducing stray light .[116] Maximizing the light absorbance is one of the important goals to achieving enhanced performance in photovoltaics. The light absorbance of any material can be calculated using, A= –log T, where A is the absorbance, and T is transmittance of the sample. The molar absorptivity is related to the concentration using the modified Beer-Lambert law: $A=\varepsilon cl$, where ε is molar absorptivity, c is the concentration, and l is the absorption path length of the sample. On the other hand, minimizing the amount of light reflected away from the surface can increase the solar cell efficiency. Many antireflection technologies have been introduced and they include coating the cell with antireflection materials or texturing the top surface of the cell to ensure light trapping within the cell until the light is fully absorbed.[117]

2.5 Measurement of Photovoltaic Properties

For performance evaluation of the fabricated solar cells, a combined testing instrument from PV Measurements Inc. that is capable of current-voltage measurement (IV-5) and quantum efficiency (QEX-10), shown in Figure 2.13, is used.

Figure 2.13 Photograph of a combined solar cell testing instrument from PV Measurements Inc. capable of current-voltage (I-V) characterisation with a solar simulator (IV-5, right) and a quantum efficiency measurement system (QEX-10, left).

The current-voltage characteristics, including the photon-to-electron conversion efficiency (PCE) are determined by using a Solar Cell I-V Testing System Model IV-5, equipped with a class ABA solar simulator for a continuous 10 cm × 10 cm illumination beam, an Air Mass (AM) 1.5 global spectral filter, and an irradiance monitor. Prior to the I-V measurement, the system is calibrated with a Si reference cell (PVM782 with a BK7 window), which is mounted on a vacuum test fixture TF5I (5 cm × 5 cm) for use with voltage probes and a provision to mount the irradiance monitor. The data is collected using a computer system running the PVM IV software, with a usable voltage range of ±2 V or ± 20V and current ranges of ± 1 μA to ± 1 A. Typically, silver paste and/or a sputter-coated gold film is employed to form the contacts, appropriate for the inorganic p-n junction device structures on hand.[118] For organic DSSCs, the typical procedure of device construction is performed, starting with dipping the prepared nanostructured TCO photoanodes in the dye solution for sufficient time to ensure efficient dye loading, and a thin film of Pt (200 nm thick) sputter-coated on ITO is used as the counter electrode. Both electrodes are sealed together using commercial hot-

melt sealing films (Meltonix, Solaronix SA, Switzerland) and liquid iodide/tri-iodide electrolyte is injected between the two electrodes for hole transfer and dye regeneration process.

The capability of a photovoltaic device to produce a voltage is often characterized by the I-V curve under two measurement conditions. First, when the cell is short-circuited under illumination, the maximum current of the cell so obtained is called the short-circuit current (I_{sc}). Second, under no current flow condition, the maximum voltage so obtained is called the open circuit voltage (V_{oc}). In addition, the fill factor (FF) of the cell corresponds to the ideal factor of diode behavior and it can be calculated using: $FF = V_{max} I_{max}/(V_{OC} I_{SC})$, where V_{max} and I_{max} are the voltage and current at maximum power. The maximum power point is calculated at the knee position of the I-V curve as $P_{max}= V_{OC} I_{SC}$ FF, which is the product of the current, the voltage, and the fill factor that gives the maximum power. These parameters are illustrated in Figure 2.14.[119] The photon-to-electron conversion efficiency (PCE) of a solar cell is calculated using the equation: PCE (%) = $V_{OC} I_{SC}$ FF / P_{in}, where P_{in} is the input power and is nominally set to 100 mW/cm^2.

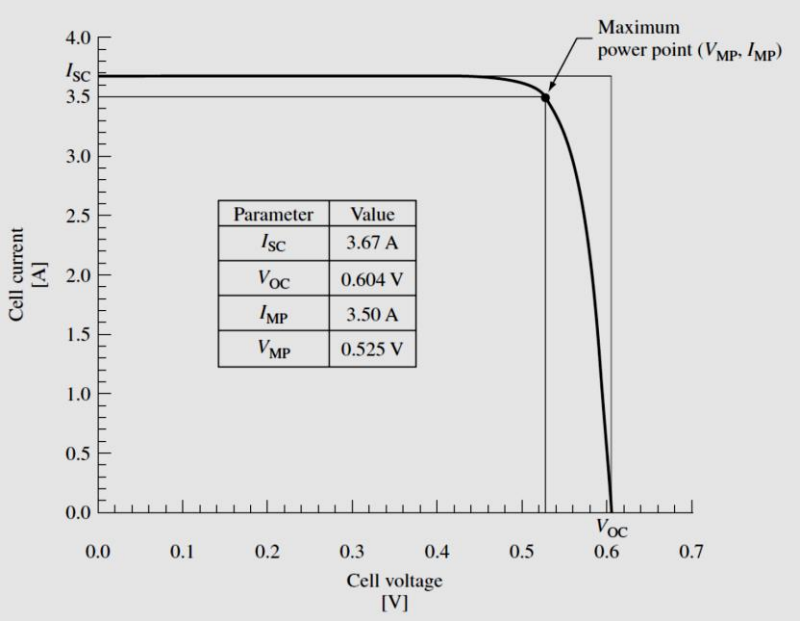

Figure 2.14 Current–voltage characteristic of a typical silicon solar cell. [119*****]

***** Reproduced with permission from: Luque, A. and Hegedus, S. Handbook of Photovoltaic Science and Engineering, 2nd, Chichester, Wiley, 2011. Copyright (2011) by John Wiley & Sons.

Another important technique used for solar cell characterization is the quantum efficiency (QE) measurement, which can be classified into two categories: external quantum efficiency (EQE) and internal quantum efficiency (IQE). EQE corresponds to the number of electron-hole pairs successfully collected per photon incident on the solar cell, while IQE is the number of electron-hole pairs successfully collected per photon absorbed by the solar cell, both as functions of wavelength. The two quantities are related to each other by the equation: EQE = (1-R) × IQE, where R is the light reflectance. The solar cell quantum efficiency measurement system (PV Measurement, Inc. QEX10) is equipped with an AC and/or DC measurement mode with voltage bias capability, which provides the ability to measure both external QE and internal QE simultaneously using specular reflection. For mounting the device for testing, a vacuum test fixture is used, along with a lab jack for raising and lowering the device under test on the z-axis to optimize beam focusing.[120] A typical EQE curve would follow a square step function of external quantum efficiency vs wavelength. The quantum efficiencies for most solar cells are reduced due to recombination loss and they are usually not measured below 350 nm, as shown in Figure 2.15.[121,122]

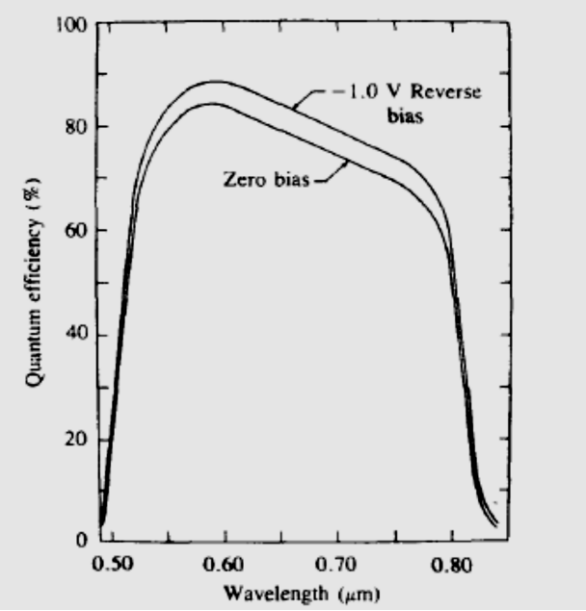

Figure 2.15 Spectral dependence of the quantum efficiency for an n-CdS/p-CdTe heterojunction, illustrating the contributions of collection function decreasing with increasing wavelength and increasing with applied reverse bias. [122†††††]

††††† Reproduced with permission from: Mitchell, K. W., Fahrenbruch, A. L. and Bube, R. H. J. Appl. Phys. 48, 4365-4371, 1977. Copyright (1977) by the American Institute of Physics.

Chapter 3

Effect of Electrolyte Conductivity on Controlled Electrochemical Synthesis of Zinc Oxide Nanotubes and Nanorods‡‡‡‡‡

3.1 Introduction

Over the past two decades, syntheses of nanostructured materials and their morphology control have remained one of the most active research areas with applications in many fields. Zinc oxide (ZnO) is one of the most promising n-type transparent semiconducting materials with a large direct band gap (3.37 eV) and a large exciton binding energy (60 meV) at room temperature. ZnO is also a bio-safe and biocompatible material.[123] Furthermore, ZnO is widely known for its diverse and versatile morphologies, including nanowires and nanorods,[124, 125] nanotubes,[126] nanobelts, [123] nanorings and nanobows,[127] nanohelixes,[128] nanosprings,[129] nanowalls,[130] nanodisks,[131] and nanopropellers.[132] Among these diverse ZnO nanostructures, nanotubes are particularly interesting. Nanotubes are often classified as one-dimensional object similar to nanowires and nanorods, [133] but the side walls making up the hexagonal cross-sectional shape of the nanotubes may be regarded as two-dimensional objects similar to the nanowalls and nanodisks.[134] This unique structure with not only large outer but also large inner surface areas, along with its optical transparency and direct band gap, make ZnO nanotubes an excellent nanomaterial for solar cell and other applications.

Several solution-based methods, including electrochemical and hydrothermal methods, have been used to synthesize ZnO nanotubes.[135,136,137,138,139,140,141,142,143,144] High-temperature methods such as chemical and physical vapor deposition have also been employed for fabricating low-dimensional nanostructured ZnO materials.[145,146,147,148] In contrast to the solution-based methods, vapor deposition is often limited by the types of compatible substrates and by the cost of large-scale production. Electrodeposition offers a simpler approach under lower-temperature conditions to producing ZnO nanostructured materials for many applications. In addition to low-temperature processing, the other advantages of electrodeposition are low equipment cost, scalability, and facile and precise control of

‡‡‡‡‡ This section is made from one of my publications: Abd-Ellah, M.; Moghimi, N.; Zhang, L.; Heinig, N. F.; Zhao, L.; Thomas, J. P.; Leung, K. T. Effect of Electrolyte Conductivity on Controlled Electrochemical Synthesis of Zinc Oxide Nanotubes and Nanorods. *J. Phys. Chem. C* 117, 6794–6799, 2013. Copyright (2013) by the American Chemical Society.

nanostructural morphology.[130, 133, 134] The general electrochemical growth in an aqueous solution is well understood in terms of a two-step mechanism: $Zn(OH)_2$ formation from Zn^{2+} and OH^- followed by dehydration of $Zn(OH)_2$ to ZnO.[149,150,151] The catalyst-induced growth of a variety of ZnO nanostructures on inexpensive substrates including indium tin oxide (ITO) coated glass or plastics by electrodeposition have already been established,[152,153,154] and their use has also been demonstrated in photovoltaic applications.[155,156,157] Recently, our group has demonstrated one-step, catalyst- and seed-layer-free electrochemical synthesis of ZnO nanostructures of both two-dimensional or 2D (nanowalls and nanodisks) and one-dimensional or 1D (nanospikes, nanobelts, nanopillars, nanowires) on ITO-glass substrates.[133, 134,158] In these electrochemical approaches, the supporting electrolyte is primarily used to increase the conductivity to a sufficient level to allow the deposition to proceed. Only one work has reported the effect of anions (Cl^-, NO_3^-, CH_3COO^-) on the electrodeposition of ZnO nanowires in a primary electrolyte with the same anions as the supporting electrolyte.[159] In particular, Elias et al. showed that the adsorption of different anions on the ZnO surface could lead to nanowires with different diameters, because these anions affect the O_2 reduction rate in the formation of $Zn(OH)_2$ and the subsequent dehydration of $Zn(OH)_2$ to ZnO.

In the present work, we employ supporting electrolytes with different anions at constant pH and investigate the importance of electrolyte conductivity as a means to control the different morphologies of the electrodeposits (nanorods vs nanotubes). We successfully produce ZnO nanotubes on ITO-glass, for the first time, by delicately manipulating the electrolyte conductivity. To date, there are a very limited number of studies on electrochemical synthesis of ZnO nanotubes. These methods require external O_2 bubbling[136], or two-step selective dissolution of ZnO nanorods[137], or a self-etching process involving over 2 hours of deposition.[160] Our method offers a direct, facile, catalyst- and seed-layer-free procedure, without the need for O_2 bubbling or any etching to produce the ZnO nanotubes. We further demonstrate the efficacy of these ZnO nanotubes as an active photoanode material in a dye-sensitized solar cell (DSSC) application.

3.2 Materials and Methods

ZnO nanostructures were electrodeposited on ITO-glass substrates at 70, 80, and 90º C in an aqueous solution (20 mL) of 0.5 mM $ZnCl_2$ mixed with a 0.1 M supporting electrolyte, at a constant pH (5-6). Three different supporting electrolytes with monovalent anions, including KCl, KNO_3 and $KClO_4$, and two supporting electrolytes with divalent anions, K_2SO_4 and $K_2C_2O_4$, were used for

nanotube and nanorod synthesis, respectively. The pH and conductivity of the electrolyte solutions were measured by using an Orion 4-Star Plus pH/conductivity dual meter. We employed a three-electrode electrochemical cell, with an ITO-glass working electrode, an Ag/AgCl reference electrode, and a Pt-wire counter electrode. Amperometry technique was conducted at –1.0 V vs Ag/AgCl for different deposition times in an electrochemical workstation (CH Instruments 1140). After deposition, the nanodeposits were rinsed thoroughly in filtered deionized water and stored in a nitrogen atmosphere to dry for at least 24 hours prior to characterization.

The surface morphologies of ZnO nanostructured films were examined by using Helium ion microscopy (HIM) in a Zeiss Orion Plus microscope and field-emission scanning electron microscopy (SEM) in a Zeiss LEO FESEM 1530 microscope. The corresponding crystal structures were characterized by glancing-incidence X-ray diffraction (XRD) using a PANalytical X'Pert Pro MRD diffractometer with Cu Kα radiation (1.54 Å) at an incidence angle ω of 0.6°. Transmission electron microscopy (TEM) measurement were performed on ZnO nanotubes and nanorods transferred onto holey carbon grids in a FEI Tecnai F20 microscope operated at 200 kV. The surface compositions of the ZnO nanodeposits were analyzed by X-ray photoelectron spectroscopy (XPS) using a Thermo-VG Scientific ESCALab 250 Microprobe with a monochromatic Al Kα source (1486.6 eV). In addition, using our ZnO nanotubes as the photoanode material, we constructed a typical DSSC device. The current-voltage characteristics were analyzed using a solar cell I-V measurement system (PV Measurements IV5) equipped with a class ABA solar simulator and an Air Mass (AM) 1.5 global spectral filter.

3.3 Results and Discussion

3.3.1 Material characterization

3.3.1.1 Morphology

Figure 3.1a and 3.1b compares the HIM images of ZnO nanorods and nanotubes obtained by electrodeposition at –1.0 V (vs Ag/AgCl) for 1 h at 80 °C in an electrolyte solution of 0.5 mM $ZnCl_2$ mixed with 0.1 M K_2SO_4 and 0.1 M KCl, respectively. The insets show close-up views of the top of the respective single nanostructures. Both the nanotubes and nanorods are found to be uniformly distributed and near-monosized, and have similar length (1.0–1.5 μm) and average diameters of 150 nm and 75 nm, respectively. The cross sections of the nanotubes and nanorods show a hexagonal

structure, consistent with the wurtzite crystal structure of ZnO, and their surfaces appear rough. We further employed HIM to ion-mill a nanotube at a slower scan rate with a higher ion current (2.2 pA for ion-milling vs. 0.5 pA for imaging) for 0, 180, and 480 s (Figure 3.1c-e, respectively), in order to examine the hole depth along the ZnO nanotube. The etching of nanotube indicates that the hole extends to the bottom of the nanotube, and the tube formation appears to begin in the early stage of growth. While these nanostructures are randomly oriented, a majority lie near-horizontally with respect to the substrate. Interestingly, the areal density of the deposited nanotubes is considerably lower than that of the nanorods. Given our deposition conditions are identical except for the nature of the supporting electrolytes; the supporting electrolytes therefore affect not only the formation of nanotubes and nanorods but also their numbers of nucleation sites. In separate experiments, we have repeated the deposition under the same conditions but with different supporting electrolytes of other monovalent anions (NO_3^-, ClO_4^-) and divalent anion ($C_2O_4^{2-}$). Deposition with monovalent supporting electrolytes gives nanotubes while that with divalent supporting electrolytes leads to nanorods, all with similar respective morphologies and areal densities as shown in Figure 3.1.

To investigate the underlying mechanism that drives the observed differences in morphology and nucleation density of the nanotubes and nanorods, we perform conductance measurements for the aforementioned electrolytes in a constant-pH acidic condition at room temperature. Equivalent conductance values are found to be similar for all supporting electrolytes with monovalent anions: Cl^- (62.8 S cm^2 mol^{-1}), ClO_4^- (59.1 S cm^2 mol^{-1}), and NO_3^- (59.2 S cm^2 mol^{-1}). However, considerably larger equivalent conductance values are observed for supporting electrolytes with divalent anions: SO_4^{2-} (207.6 S cm^2 mol^{-1}) and $C_2O_4^{2-}$ (207.4 S cm^2 mol^{-1}). This result indicates that the differences in ion diffusion (as reflected by the conductance values) have significant effects on the morphologies of the electrodeposits and their nucleation densities, i.e. less conducting electrolytes with monovalent anions give rise to less densely distributed nanotubes while more conducting electrolytes with divalent anions produce more densely packed nanorods. Our observation is in good agreement with our cyclic voltammetric and amperometric results for ZnO nanotubes and nanorods (not shown). These results confirm that the current is controlled by the nature and kinetics of the ion diffusion, both of which are strongly influenced by the state of the cathode surface and the adsorption of different anions on the ZnO surface. In other words, the highly conducting media enhance the diffusion of Zn^{2+} ions to the cathode surface and build up the (0001) plane, resulting in 1D nanorod

growth. In contrast, less conducting media hinder the ion diffusion and, together with the termination of the (0001) plane due to adsorption of monovalent anions, lead to the nanotube growth.

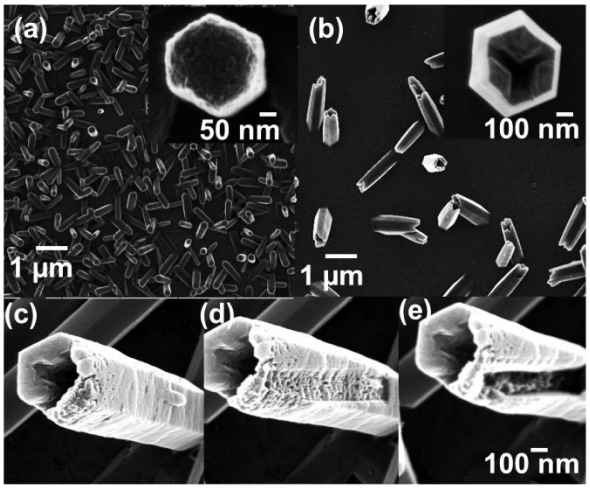

Figure 3.1 HIM images of (a) ZnO nanorods and (b) nanotubes electrodeposited on ITO-glass substrates at –1.0 V (vs Ag/AgCl) for 1 h at 80 °C in a 0.5 mM $ZnCl_2$ solution mixed with 0.1 M KCl and 0.1 M K_2SO_4, respectively. (c-e) Ion milling of a ZnO nanotube for 0, 180, and 480 s, respectively, to depict its hole depth.

We have also studied the effects of deposition time and temperature on the growth of nanorods and nanotubes. Our results for the nanorods have been reported elsewhere.[130] For nanotubes (Figure 3.2a-c), increasing the deposition time while maintaining the same deposition temperature increases the areal density but reduces their average length. These results suggest that the nucleation rate is faster than the growth rate, which reflects a progressive nucleation growth mechanism. For the same deposition time (60 min, Figure 3.2d-f), reducing the deposition temperature from 80 °C (Figure 2e) to 70 °C (Figure 3.2d) appears to decrease the average length slightly and increase the areal density. On the other hand, increasing the deposition temperature to 90 °C (Figure 3.2f) produces clustering of nanotubes over a smaller number of nucleation sites (i.e. a lower density) but with a similar average length to that of the nanotubes grown at 80 °C. This suggests that the kinetics of the hydroxide formation affect the length of the ZnO nanotubes and their nucleation morphologies (i.e. singles vs clusters). These vertically oriented nanotube flowers, with 50–100 nm in diameter and 1.0–1.2 μm in length for individual nanotubes, are excellent candidates as photoanode materials for solar cell applications.[161]

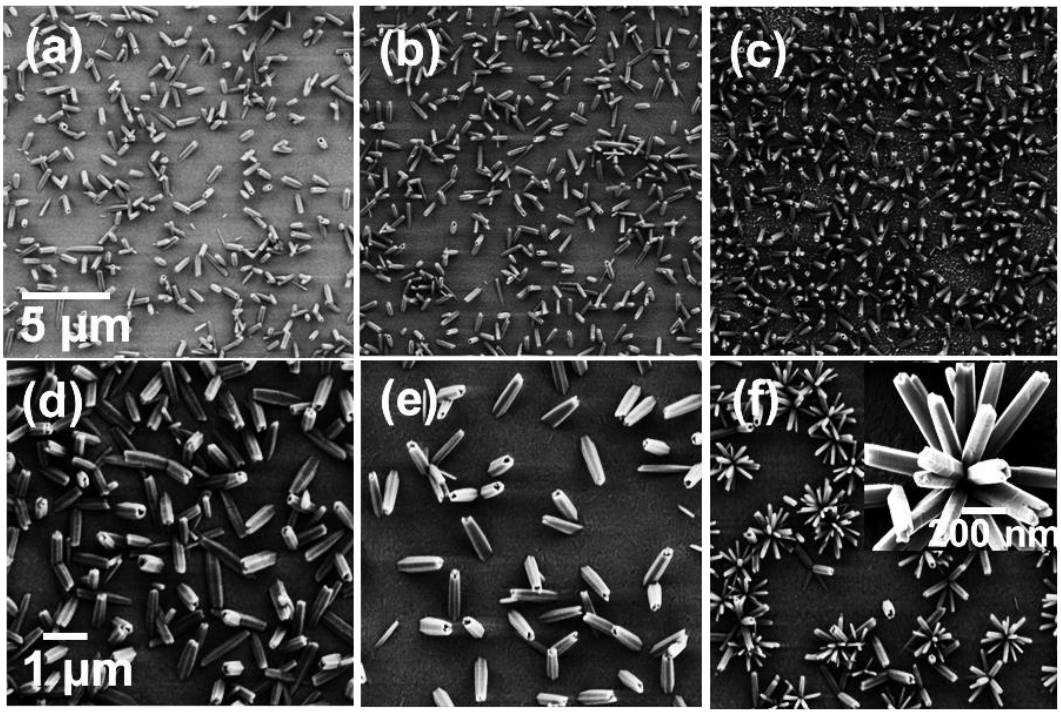

Figure 3.2 SEM images of ZnO nanotubes electrodeposited on ITO-glass substrates at –1.0 V (vs Ag/AgCl) in a 0.5 mM $ZnCl_2$ solution mixed with 0.1 M KCl at 80 °C for (a) 30, (b) 120, and (c) 150 min, and at (d) 70, (e) 80, and (f) 90 °C for 60 min.

3.3.1.2 Crystallography

Figure (3.3a) compares the glancing-incidence XRD patterns of electrodeposited ZnO nanotubes and nanorods obtained with different supporting electrolytes of monovalent (NO_3^-, Cl^-, ClO_4^-) and divalent anions (SO_4^{2-}, $C_2O_4^{2-}$). Despite the intense XRD peaks from the ITO substrate, we observe weaker XRD features due to the ZnO nanotubes and nanorods. These weaker XRD features are consistent with the hexagonal wurtzite structure in the reference pattern for ZnO powder (JCPDS 01-076-0704). In particular, the features at 31.7°, 34.4°, 36.2° and 56.5° are assigned, respectively, to the ZnO (100), (002), (101) and (110) planes, consistent with the most prominent XRD features in the reference powder spectrum. Among the four aforementioned ZnO features, the (0001) feature is the strongest for the nanorods, while the (0001) and (10 –11) features for the nanotubes are found to have very similar intensities. In our early work on 2D and 1D ZnO nanostructures, we also observe that the most intense ZnO feature corresponds to the (10 –11) plane for the 2D nanostructures (nanowalls and nanodisks) and to the (0001) plane for the 1D nanostructure

(nanowires).[130] The similarity in intensity found for the (0001) and (10 –11) features for the nanotubes therefore suggests that the nanotubes exhibit 2D-like characteristics similar to the nanowalls, which could be attributed to the nanotube walls.

On the other hand, the nanorods effectively follow the 1D growth, characteristics of the nanopillars reported earlier. [130] The intensity ratio of the (0001) to (10 –11) features for the nanorods (1.3) is larger than that for the nanotubes (0.9), which is consistent with the larger component of the (0001) plane for the nanorods than the nanotubes (with hollow center). However, the intensity ratio of the (0001) to (10 –11) features for the nanotubes (0.9) is found to be discernibly larger from that for the nanowalls (0.5), suggesting that there is a relative larger contribution to the (0001) feature for the nanotubes than that for the nanowalls. This could be explained by our proposed "blind nanotube" model, as illustrated in Figure (3.3d). In this growth model, initiation of ZnO growth begins by stacking hexagonal disks in the [0001] direction (i.e., perpendicular to the substrate) producing nanorods. As the growth continues in the less conducting electrolytes with monovalent anions, the termination rate of the (0001) plane could become faster than the $Zn(OH)_2$ formation rate. This produces growth with a higher contribution in the (10 –11) plane, which leads to the formation of ZnO hexagonal rings. Stacking of these hexagonal rings eventually produces the blind nanotube. On the other hand, the termination rates of the (0001) plane in the more conducting electrolytes with divalent anions are not sufficiently fast to overtake the $Zn(OH)_2$ formation rate. The growth therefore remains in the [0001] direction, forming the ZnO nanorods. The presence of these hexagonal disk-like and ring-like nanostructures is quite evident from the corresponding SEM images of nanotubes (Figure 3.3 b) and nanorods (Figure 3.3 c). Furthermore, our model is also consistent with our TEM measurement, along with their respective selected area electron diffraction (SAED) patterns, for a typical ZnO nanotube and a nanorod, as shown in Figure 3.3e and 3.3f, respectively. In particular, the SAED patterns for both nanotube and nanorod reveal a growth direction perpendicular to the (002) plane, i.e., along their respective length in the [0001] direction. The different growth orientations in the (100), (002), (101) and (110) planes in both nanotubes and nanorods are also found to be in good agreement with our XRD results (Figure 3.3a).

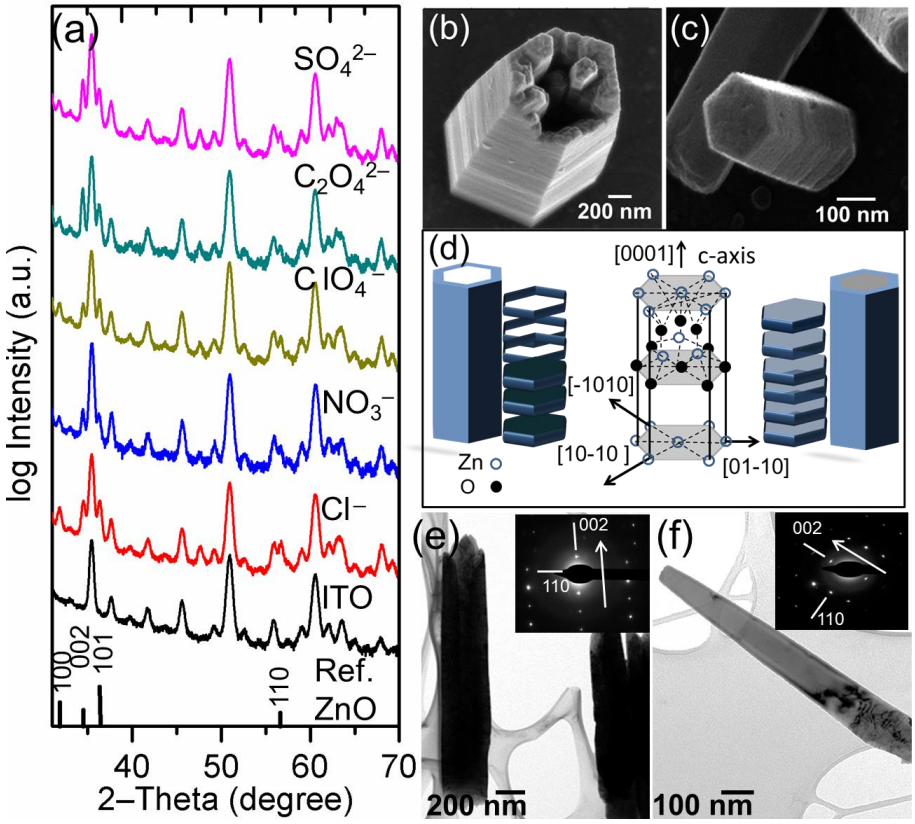

Figure 3.3 (a) Glancing-incidence XRD patterns, (b, c) SEM images, (d) growth models, and (e, f) TEM images, with the corresponding selected area electron diffraction patterns shown in insets, for as-electrodeposited ZnO nanotubes and nanorods obtained with supporting electrolytes with, respectively, monovalent (NO_3^-, Cl^-, ClO_4^-) and divalent anions (SO_4^{2-}, $C_2O_4^{2-}$).

3.3.1.3 Chemical-state compositions analysis

Chemical-state compositions are also determined for typical ZnO nanotubes and nanorods obtained with supporting electrolytes of Cl^- and SO_4^{2-} anions, respectively. Their corresponding depth-profiling XPS spectra shown in Figure 3.4 are found to be similar. Evidently, the Zn $2p_{3/2}$ feature observed near 1022.3 eV corresponds to Zn^{2+} oxidation state, consistent with ZnO. Further sputtering does not change the binding energy position of the Zn $2p_{3/2}$ feature but gradually reduces its intensity as shown in Figure 3.4a and 3.4d. On the other hand, as shown in Figure 3.4b and 3.4e, the two O 1s features found at 530.7 eV and 532.0 eV upon light sputtering of 60 s could be attributed to ZnO and to OH^- adsorbed on ZnO, respectively, which is in good accord with the literature.[162]

Additional sputtering evidently reduces the ZnO O 1s component without discernible reduction to the adsorbed OH^- O 1s component, indicating that OH^- adsorbed primarily on the perimeter of the ZnO nanostructures, as illustrated in Figure 3.4f. To investigate the importance of the termination effect provided by the anions, we also measure the Cl 2p and S 2p spectra for the respective nanotube and nanorod samples. For the nanotube sample, the presence of a weak but discernible Cl 2p feature (Figure 3.4c) confirms the termination of Cl^- ions in the growth mechanism for the nanotubes, as similarly found for other 2D ZnO nanostructures (e.g. nanowalls). The adsorption of Cl^- ions preferentially on the ZnO(0001) plane leads to a higher contribution in the (10 –11) plane, effectively producing 2D growth of the hexagonal ring as illustrated in Figure 3.4f. However, for the nanorod sample, the absence of S 2p (or Cl 2p) intensity for the as-deposited sample indicates that termination by such anion SO_4^{2-} (or Cl^-) does not occur for the 1D ZnO nanostructure growth, again consistent with earlier studies found for, e.g., nanowires.[130]

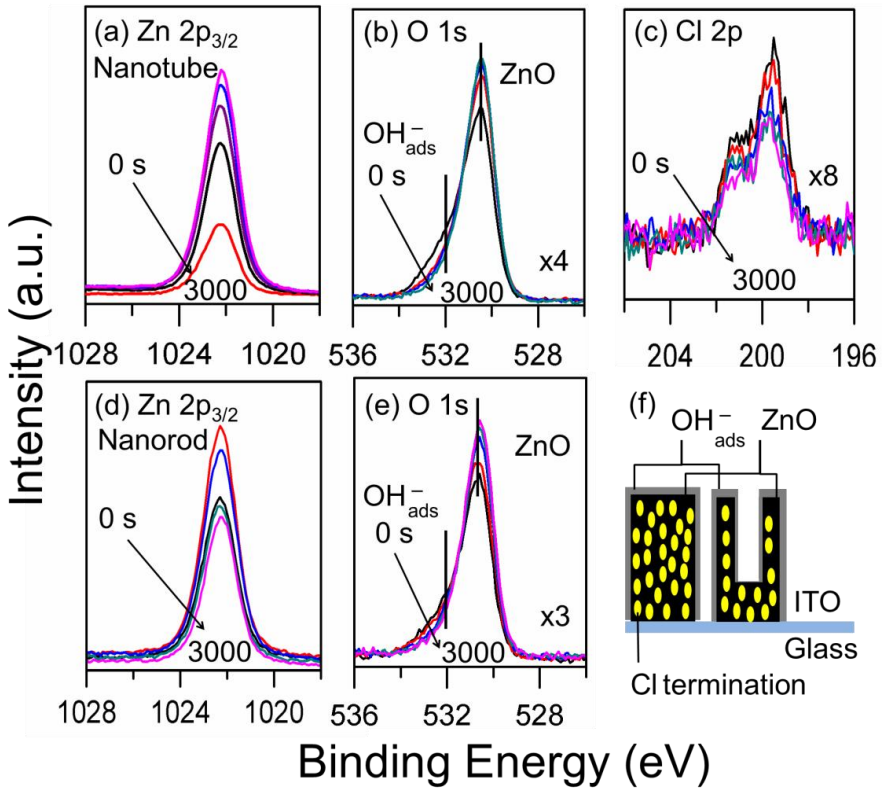

Figure 3.4 XPS spectra of Zn $2p_{3/2}$, O 1s, and Cl 2p regions collected for the as-prepared (a-c) ZnO nanotubes and (d, e) nanorods, respectively, and upon sputtering for 60, 900, 1800, and 3000 s. (f) Schematic diagram of the chlorine termination effect on the as-prepared ZnO nanotubes and nanorods on ITO-glass.

3.3.2 Growth mechanism

The electrochemical deposition of ZnO nanostructured materials from a $ZnCl_2$ solution with different supporting electrolytes is well understood according to the following reaction mechanism.[163] Following the dissolution of $ZnCl_2$: $ZnCl_2(aq) \rightarrow Zn^{2+}(aq) + 2Cl^-(aq)$, formation of the hydroxide ions can proceed via the following reaction:

$$2H_2O(l) + 2e^- \rightarrow H_2 \uparrow + 2OH^-(aq) \qquad (1)$$

$Zn(OH)_2$ is then formed from the Zn^{2+} and the hydroxide ions, following the reaction:

$$Zn^{2+}(aq) + 2OH^-(aq) \rightarrow Zn(OH)_2(s) \quad \textit{slow} \qquad (2)$$

Finally, dehydration reaction of $Zn(OH)_2$ leads to production of ZnO:

$$Zn(OH)_2 \rightarrow ZnO(s) + H_2O(l) \quad \textit{fast} \qquad (3)$$

It is well known that two-dimensional nanostructures of ZnO (e.g. nanowalls) are due to preferential adsorption of Cl^- (or any appropriate anion) on the (0001) plane, which leads to termination of growth in this direction and a higher contribution in the (10 –11) plane. Furthermore, the $Zn(OH)_2$ generation must be sufficiently slow to expose the effect of growth termination in the (0001) plane leading to 2D nanostructures. For example, for a $ZnCl_2$ electrolyte concentration of 50 mM, the Cl^- adsorption rate on the (0001) plane is higher than the ZnO growth rate on the same plane, which results in the formation of 2D nanowalls as shown in Figure (3.5a, inset). On the other hand, for a sufficiently low $ZnCl_2$ electrolyte concentration (5 mM), the Cl^- adsorption rate on the (0001) plane becomes insufficient to overcome the ZnO growth rate on the same plane, which leads to the formation of 1D nanorods as shown in Figure 3.5b.

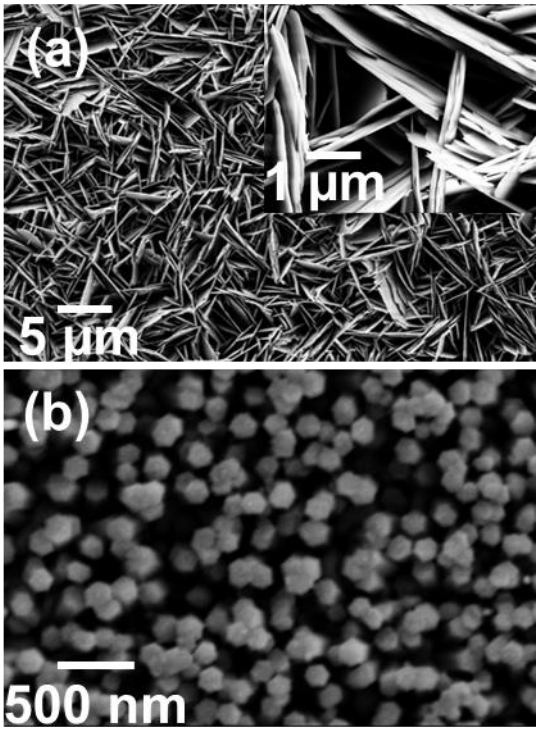

Figure 3.5 SEM images of (a) ZnO nanowalls and (b) nanorods electrodeposited on ITO-glass substrates at –1.0 V (vs Ag/AgCl) for 1 h at 80 °C in a 50 mM and a 5 mM $ZnCl_2$ solutions, respectively, each mixed with 0.1 M KCl.

For an even lower $ZnCl_2$ electrolyte concentration (0.5 mM), we show in Figure 3.1 that it is possible to obtain 1D nanorods and "pseudo 2D" nanotubes. By employing supporting electrolytes with the appropriate concentration to manipulate the overall electrolyte conductivity, we could achieve a fine balance between the $Zn(OH)_2$ generation rate and the Cl^- adsorption rate to create the pseudo 2D structure as exhibited by the nanotubes. Because the electrolytes contain the same amounts of Zn^{2+} and K^+ cations for all the depositions in the present work, the difference in the conductivity must come from differences in the anions of the supporting electrolytes. The limiting ion conductivity in water at 298 K (values given in parentheses) for the anions of our supporting electrolytes follow the order: ClO_4^- (6.73 mS m^2 mol^{-1}) < NO_3^- (7.14 mS m^2 mol^{-1}) < Cl^- (7.634 mS m^2 mol^{-1}) < $C_2O_4^{2-}$ (14.82mS m^2 mol^{-1}) < SO_4^{2-} anions (15.96 mS m^2 mol^{-1}).[164, 165] A highly conducting electrolyte is expected to enhance the diffusion of Zn^{2+} and therefore lead to a higher $Zn(OH)_2$ generation and subsequently a higher ZnO deposition. If the conductivity is sufficiently high to attain a higher ZnO growth rate than the Cl^- adsorption rate (as in the divalent anion case), then we obtain the expected

1D nanorod formation. However, if the conductivity is barely sufficient such that the ZnO growth rate is slightly lower than the Cl^- adsorption rate (as in the monovalent anion case), then the pseudo 2D nanotube formation would occur.

It is of interest to compare the present work with that of Elias et al., who reported the control of average diameters of nanowires by changing the electrolytes with anions Cl^-, SO_4^{2-}, and CH_3COO^-.[159] They suggested that the different adsorption rates of these anions (on the ZnO surface) result in different $Zn(OH)_2$ generation rates, which in turn affect the diameters of the nanowires. In the present work, our primary electrolyte is $ZnCl_2$ with the same concentrations for all the studies and we only change the supporting electrolytes. We therefore expect that the adsorption rate of the Cl^- anions is much more important than those anions from the supporting electrolytes. This is in contrast to the work of Elias et al., who selected both primary and supporting electrolytes to provide the same anions. The effect observed by Elias et al. cannot therefore be used to account for the differences in the morphologies between the nanorods and nanotubes.

Another plausible contributing factor to the mechanism is the common ion effect, which could possibly be operative for our KCl supporting electrolyte. In this case, the increase in the Cl^- (due to the KCl supporting electrolyte) cause an increase in the Zn^{2+} production that leads to more $Zn(OH)_2$ generation. At the same time, the adsorption rate of Cl^- is also expected to increase while maintaining the fine balance such that the ZnO growth rate is slightly lower than the Cl^- adsorption rate. In order to further investigate the common ion effect hypothesis, we prepare, in a separate experiment, different concentrations of the KCl supporting electrolyte. We observe that ZnO nanotubes can be produced when the KCl concentration is increased to 3.5 M (from 0.1 M). However, when KCl concentration goes above 4 M (with an equivalent conductivity of 193.5 mS m^2 mol^{-1}), only ZnO nanorods are obtained, which suggests that the common ion effect does not play a dominant role. This result instead confirms our earlier hypothesis that the electrolyte conductivity has a more prominent effect on the morphologies of the ZnO nanostructures.

3.3.3 Application to dye sensitized solar cell

ZnO has been demonstrated as the n-type semiconductor material for general photovoltaic applications.[166,167] Indeed, with its excellent optical transparency, a wide direct band gap, high electron mobility and electron diffusion coefficient, ZnO offers better characteristics than TiO_2 for constructing DSSCs.[90,168] ZnO nanotubes provide an obvious advantage due to their higher surface

area for DSSC application (with both inside surface and outside surface) than other 1D nanostructured materials such as nanorods (with just outside surface). The present work demonstrates that it is possible to control the diameter (100–200 nm) and length (1–1.5 μm) of the ZnO nanotubes with a narrow size distribution by electrodeposition, therefore producing an optimized size regime for DSSC application. In the present work, we prepare a DSSC using a standard procedure.[166] The working electrode is obtained by soaking the as-prepared ZnO nanotubes (supported on an ITO-glass substrate) in a 0.3 mM solution of commercial dye (Z907, purchased from Solarnix) for 12 hours, while a Pt thin film (200 nm thick) sputter-deposited on the ITO-glass substrate is used as the counter electrode. A redox couple electrolyte (I/I^{-3}) is then sandwiched between the working and counter electrodes. Under AM1.5 illumination, our DSSC exhibits a typical short circuit current density (J_{sc}) of 11.51 mA cm^{-2}, an open circuit voltage (V_{oc}) of 687.75 mV, a fill factor (FF) of 22%, and overall photon conversion efficiency (PCE) of 1.6% as shown in figure 3.6. This efficiency is comparable to the performance of DSSCs based on ZnO nanotubes deposited by ALD technique (1.6 %)[169] and by the two-step procedure (electrodeposition followed by chemical etching) (1.18 %).[170] The lower efficiency found in the latter work could be due to the defects created along the nanotubes during the etching process, which leads to less efficient dye loading.

A recent review paper indicates that different morphologies of ZnO-based DSSCs with different dyes can show efficiencies ranging from 1.5 to 7.5%.[168] Further modifications may be possible for enhancing the porosity and roughness of the ZnO nanotube surface in order to improve the dye loading. For example, annealing is found to not just improve the crystallinity, but also enhance the material porosity, as shown in our earlier study on ZnO nanowalls. In particular, the post-annealed nanowalls appear to become perforated with distinct nanograins as part of the nanowall frame.[171] Upon annealing, the perforated morphology expected of these ZnO nanotubes could significantly enhance the performance of the photoanode in DSSCs, because of their larger surface area available for absorbing the dye sensitizer. Further control of the aeral density and dimension of the ZnO nanotubes would allow us to optimize the performance of ZnO-based DSSCs.

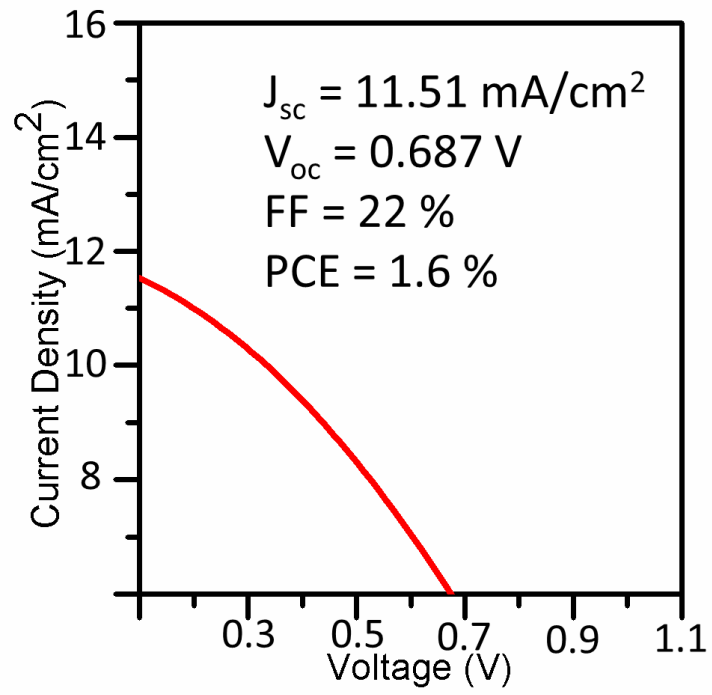

Figure 3.6 J-V characteristics under AM 1.5G illumination of a DSSC based on a ZnO nanotube photoanode.

3.4 Conclusion

ZnO nanotubes have been synthesized on ITO-glass substrates for the first time by using a one-step, catalyst- and seed-layer-free electrodeposition method without O_2 bubbling or any etching. We show that the morphology of the ZnO nanostructures (i.e. nanotubes vs nanorods) can be controlled by varying the supporting electrolyte with different anions. As finely controlled by manipulating the supporting electrolytes with different anions, solution conductivity is found to play a more prominent role in producing the nanotube morphology. We also illustrate that these ZnO nanotubes could be used as active photoanode materials in DSSCs that offer respectable efficiency.

Chapter 4

Enhancement of Solar Cell Performance of Cu_2O/ZnO-nanotube Heterojunction Device

4.1 Introduction

Renewable energy is a rapidly growing field in the past two decades. Photovoltaics provide one of the most promising green energy generation technologies, because of its economic viability and environmental sustainability. To date, silicon-based solar cells are the most mature technology, with the highest photon-to-electron conversion efficiency (PCE) exceeding 20%. Recently, the use of other emerging materials, such as CdTe and GaN, has produced nearly equivalent performance. However, less toxic, more abundant alternative materials and potentially lower-cost manufacturing methods for these solar cells remain elusive, yet highly desirable in the marketplace.[172,173]

Many other organic and inorganic materials have been introduced recently with relatively high PCE performance. One of the more promising, low-cost heterojunction inorganic solar cell systems involves the construction of a typical p-n junction device by depositing a p-type Cu_2O thin film onto an n-type ZnO film on an ITO-glass substrate. In addition to its advantages of low-cost and material abundance, this system offers the preferred atomic arrangement at the junction interface with low lattice mismatch (only 7.1%) at the interface between ZnO(001) and Cu_2O(111) planes.[174] With a large direct band-gap (3.37 eV), a large exciton binding energy (60 meV), and a high electron mobility (120 $cm^2\ V^{-1}\ s^{-1}$), ZnO is considered an excellent candidate as an n-type transparent semiconducting material at room temperature for photovoltaic application. On the other hand, cuprous oxide (Cu_2O) is an inexpensive p-type metal-oxide semiconductor, with unique optical and magnetic properties and a direct band gap of 2.1 eV.[175] The p-type conduction property of Cu_2O is due to the formation of Cu vacancies and delocalized holes after the removal of copper atoms from the lattice through oxidation [$Cu_{lattice}(I) \rightarrow Cu^0 + h^+$].[176]

Several high-temperature and low-temperature methods, including hydrothermal,[177] thermal oxidation,[178] reactive magnetron sputtering[179] and electrodeposition,[180,181,182,157] have been used to synthesize Cu_2O films. The fabrication of typical p-Cu_2O/n-ZnO heterojunction solar cells also includes a number of mixed methods, such as sputtering aluminum-doped ZnO film onto electrodeposited Cu_2O thin films,[183] and depositing ZnO thin films on high-quality thermally oxidized

copper sheets.[184] With precise control of the deposition parameters, electrodeposition could provide high-quality films with several notable advantages, including material stability due to favorable low-temperature deposition conditions, better crystallinity, and higher conductivity. Electrodeposition also offers complete filling of any physical voids among the nanostructures, which greatly improves the quality of coating of the absorber film for solar cell application.[185] Several electrochemical studies have focused on the construction of p-Cu_2O/n-ZnO planar and nanostructured film architectures. While the conversion efficiency of typical electrodeposited p-Cu_2O/n-ZnO heterojunction solar cells could theoretically be as high as 18%, the maximum efficiency reported to date using electrochemical deposition method is only less than 1.5%.[186,187,188] This could be due to the creation of interface defects during the sequential electrodeposition process, which could lead to higher recombination by interfacial traps and to limited open-circuit voltage with low built-in potential arising from the misalignment between p-type and n-type materials.[189]

Many studies have concentrated on optimizing the synthesis of the Cu_2O film, which acts as the main absorber layer, as the key to enhancing the performance of p-Cu_2O/n-ZnO heterojunction solar cells. In addition to the importance of the synthesis method that invariably affects the electrical properties of the prepared films; different supplementary approaches have also been used to improve the efficiencies of Cu_2O for photovoltaic applications. For example, surface passivation of Cu_2O films with hydrogen or cyanide ions, rapid quenching of Cu_2O films to room temperature after the oxidation process at high temperature, and vapor deposition of a Cu_2O buffer layer have all been attempted in an effort to reduce recombination loss by eliminating the interfacial trap states.[190] Another important approach to improve the p-n junction performance is by optimizing the film thicknesses of both p- type and n-type materials. Recently, the effects of growth parameters for optimizing the crystallinity and thickness of Cu_2O thin films on ZnO nanorod solar cells were investigated, but the best PCE so obtained was only 0.33%, with an open-circuit potential (V_{OC}) of 0.15 V, a short-circuit current density (J_{SC}) of 7.03 mA/cm^2 and a fill factor (FF) of 0.33.[181] Another study showed that the limited performance of electrodeposited Cu_2O/ZnO planar heterojunction solar cells could be due to the critical minority carrier length, suggesting that only photogenerated carriers within the top 430 nm region in a 1600 nm thick absorber layer would likely be collected.[191] Many studies have therefore focused on nanostructure-based systems to minimize the electron transport lengths. One-dimensional nanostructures have been employed successfully to improve J_{SC} due to their higher junction areas and more direct pathways that lead to better charge carrier collection. However,

the limited V_{OC} continues to be more problematic for these systems. As pointed out in a recent study, engineering of the optimal spacing between the one-dimensional nanostructures that is required for efficient charge collection and of the minimum thickness needed for the formation of full built-in potential to inhibit any unwanted recombination loss remains to be very difficult.[192] However, this latter work has succeeded in enhancing the V_{OC} by optimizing the Cu_2O thickness (3 μm) for the planar junction device structure with respectable values of V_{OC}, J_{SC}, and PCE of 0.35 V, 3.7 mA/cm^2, and 0.6 %, respectively. While increasing the absorber thickness for radial junction device structure did not affect their V_{OC}, the low V_{OC} value (~ 0.2 V) was attributed to the presence of local shunting and inhibition of depletion layer formation. In contrast, an increase in V_{OC} up to 0.51 V has been demonstrated for solar cells consisting of a Cu_2O thin film on sparsely deposited ZnO nanorods, confirming that higher V_{OC} values could be achieved for nanostructure-based radial junction devices.[185] In addition, the earlier study has suggested that higher conductivity of the absorber material and better quality of the junction interface and device geometry are required to further improve the performance.[192]

Here, we investigate several techniques to enhance the V_{OC} and J_{SC} values of Cu_2O/ZnO solar cells based on ZnO nanotubes (ZnO-NTs) and nanorods (ZnO-NRs). By employing high-surface-area tubular nanostructures that we obtain by direct electrodeposition,[193] we produce a higher junction area and reduce undesirable recombination loss. Our synthesis method does not lead to a high defect density that is commonly generated in other methods, particularly those that require etching of electrodeposited nanorods to create the tubular nanostructures.[175] Another factor that is responsible for the low V_{OC} commonly found in other Cu_2O/ZnO systems is the low electron mobility of the electrodeposited Cu_2O film. Our remedy here is to perform a simple post-annealing step that would reduce the grain boundaries and decrease the surface defects. An improvement in the conductivity of the electrodeposited Cu_2O film is also achieved, along with a remarkable reduction in their reflectance, which would make the Cu_2O film also an excellent anti-reflectance layer. Finally, a thick ZnO seed layer is electrodeposited prior to the growth of the one-dimensional ZnO nanostructures to ensure the full built-in potential formation and to minimize any leakage current pathway. We show that these techniques produce greatly enhanced open-circuit voltages for both solar cells based on nanotubes (0.66 V) and nanorods (0.71 V), while the resulting short-current density (2.42 mA/cm^2) and the overall PCE (0.8%) for the former have been effectively doubled that of the latter (1.15 mA/cm^2 and 0.4%, respectively).

4.2 Materials and Methods

A typical p-n junction solar cell was constructed as follows. Prior to any deposition step, the ITO/glass substrates was polarized by applying a 10mA/cm^2 current for 60-120 s in 1 M NaOH in order to create a higher density of nucleation sites and therefore subsequently as-grown materials.[153] A seed layer of ZnO was first electrodeposited in an electrolyte of water and ethanol in a 3:1 volume ratio to eliminate any pinhole that could result in shorting across the junction.[192] Electrodeposition was then performed for n-type ZnO nanotubes or nanorods as described in our earlier work (as discussed in Chapter 3),[193] and this was followed by electrodeposition of p-type Cu_2O thin films. Cuprous oxide thin films were electrodeposited, either on pristine ITO-glass substrates for initial characterization or on ZnO nanostructures supported on ITO-glass substrates for solar cell fabrication, in an aqueous solution of 0.4 M cuprous sulphate pentahydrate (Sigma-Aldrich, 98%) and 3 M lactic acid (Sigma-Aldrich, 98%) held at 60 °C by potentiostatic amperometry at –0.4 V (vs Ag/AgCl) for 600 s. The pH of the alkaline medium was adjusted to 12 by addition of 4 M NaOH with constant stirring during deposition. To examine the effect of post-annealing, the as-grown films were then annealed at 200, 300, and 400 °C for 30 min. Complexing Cu^{2+} with lactate ion could stabilize the Cu^{2+} ions in the alkaline media, allowing them to diffuse through the electrolyte. Cu^{2+} was then reduced to Cu^{+} following the reaction:[194,195] $2Cu^{2+} + 2OH^{-} + 2e^{-} \rightarrow Cu_2O + H_2O$. For the aforementioned device work, a thicker Cu_2O film obtained with 900 s electrodeposition was used to ensure complete coverage of the ZnO nanostructures supported on the substrate. For all sample preparation, we employed a three-electrode electrochemical cell, with an ITO-glass working electrode, an Ag/AgCl reference electrode and a Pt-wire counter electrode, in an electrochemical workstation (CH Instruments 1140). After deposition, the as-prepared samples were rinsed thoroughly in filtered deionized water and stored in a nitrogen atmosphere to dry for at least 24 h prior to characterization.

The surface morphologies of copper oxide thin films were examined by helium ion microscopy (HIM) in a Zeiss Orion Plus microscope and by field-emission scanning electron microscopy (SEM) in a Zeiss Merlin microscope. The corresponding crystal structures were characterized by glancing-incidence X-ray diffraction (XRD) using a PANalytical X'Pert Pro MRD diffractometer with Cu Kα radiation (1.54 Å) at an incidence angle of 0.6°. In addition, their surface compositions were analyzed by X-ray photoelectron spectroscopy (XPS) using a Thermo-VG Scientific ESCALab 250 Microprobe with a monochromatic Al Kα source (1486.6 eV). The Cu_2O

thin film topography and their diode behavior were investigated by conductive atomic force microscopy (AFM) in an Asylum Research Cypher microscope with the imaging current collected using a Ti-Ir tip. For resistivity and carrier concentration measurements using the four-point probe method in a van der Pauw configuration (Ecopia HMS-5300), gold contacts were sputter-deposited by magnetron sputtering with a current of 50 mA for 120 s on the four corners of the Cu_2O film. Their reflectance was measured using a Perkin-Elmer Lambda 35 or 1050 UV/Vis spectrometer. Elemental analysis across the cell junction interface was studied by scanning Auger microscopy (SAM) in a Thermo MicroLab 350 Microprobe. The current density vs voltage (J-V) characteristics were analyzed by using a solar cell measurement system (PV Measurements IV5) equipped with a class ABA solar simulator and an Air Mass (AM) 1.5 global spectral filter. Prior to the J-V measurement, the system was calibrated using a Si reference cell (PVM782 with a BK7 window).

4.3 Results and Discussion

4.3.1 Pristine electrodeposited Cu_2O thin films and their electrical and optical properties

Cu_2O has been extensively studied because of their unique properties for photovoltaic application. [184,187, 196,197,198] In particular, electrodeposited Cu_2O films exhibit high photoelectrochemical stability and excellent electronic properties among other metal oxides.[199,200] Figure 4.1a shows the SEM images of Cu_2O octahedral structures obtained by electrodeposition in an alkaline solution of copper lactate for 600 s. For a thicker Cu_2O film (obtained by 900 s electrodeposition), the film appears continuous with half pyramidal structures, likely due to merging of the octahedrons with a larger film thickness without a notable effect on their surface morphology upon post-annealing at 200°C, as shown in the HIM images of Cu_2O film after and before the annealing step in (Figure 4.1b, inset). It should be noted that HIM provides better surface morphology contrast due to the considerably less divergent helium ion beam when compared with the electron beam employed in SEM. Figure 4.1c shows the glancing-incidence XRD patterns of the as-electrodeposited thicker Cu_2O film (obtained by 900 s (Figure 1b, inset) and upon annealing to 200, 300, and 400 °C for 30 min. In addition to the XRD peaks from the ITO substrate, we observe the strong Cu_2O (111) feature at 36.4° and the weaker Cu_2O (200) feature at 42.3° for the as-deposited Cu_2O sample and upon the 200°C anneal, in good accord with the reference pattern of the cubic (FCC) crystal structure of Cu_2O. However, upon annealing to 300°C, the weak feature at 35.5°

normally attributed to ITO appears more intense, which can be caused by additional contribution from an emerging CuO (002) feature at the same 2-theta position. Along with the emergence of the CuO (111) feature at 38.7° and the concomitant intensity reduction of the Cu_2O (110) feature at 29.0° and Cu_2O (200) feature at 42.3°, these changes indicate the conversion of Cu_2O to CuO. Further annealing at 400°C leads to emergence of other weaker CuO features such as the (110) plane at 32.6°, which further confirms nearly complete conversion of Cu_2O to CuO upon the 400°C anneal.

Figures 4.1d and 4.1e show the depth-profiling XPS spectra of the Cu $2p_{3/2}$ and Cu LMM regions, respectively, for the as-prepared 900-s Cu_2O film. Evidently, the Cu $2p_{3/2}$ feature near 932.6 eV corresponds to the Cu^+ oxidation state; consistent with Cu_2O. [111] The missing Cu^{2+} feature near 933.7 eV supports the absence of CuO (Figure 4.1d). Since the Cu 2p binding energies for both Cu_2O and metallic Cu are essentially the same, we examine the Cu LMM Auger region (Figure 4.1e). The Cu LMM peak observed near 569.5 eV confirms the presence of Cu^+ oxidation state rather than that for Cu^0 (expected at 568.0 eV). Except for the gradual reduction in intensity, sputtering does not change the peak positions of the Cu $2p_{3/2}$ and Cu LMM features, confirming the purity of Cu_2O nanostructures without any core-shell architecture with the shell containing, e.g., CuO or metallic Cu. These results are consistent with our XRD data for the as-deposited Cu_2O thin film (Figure 4.1c).

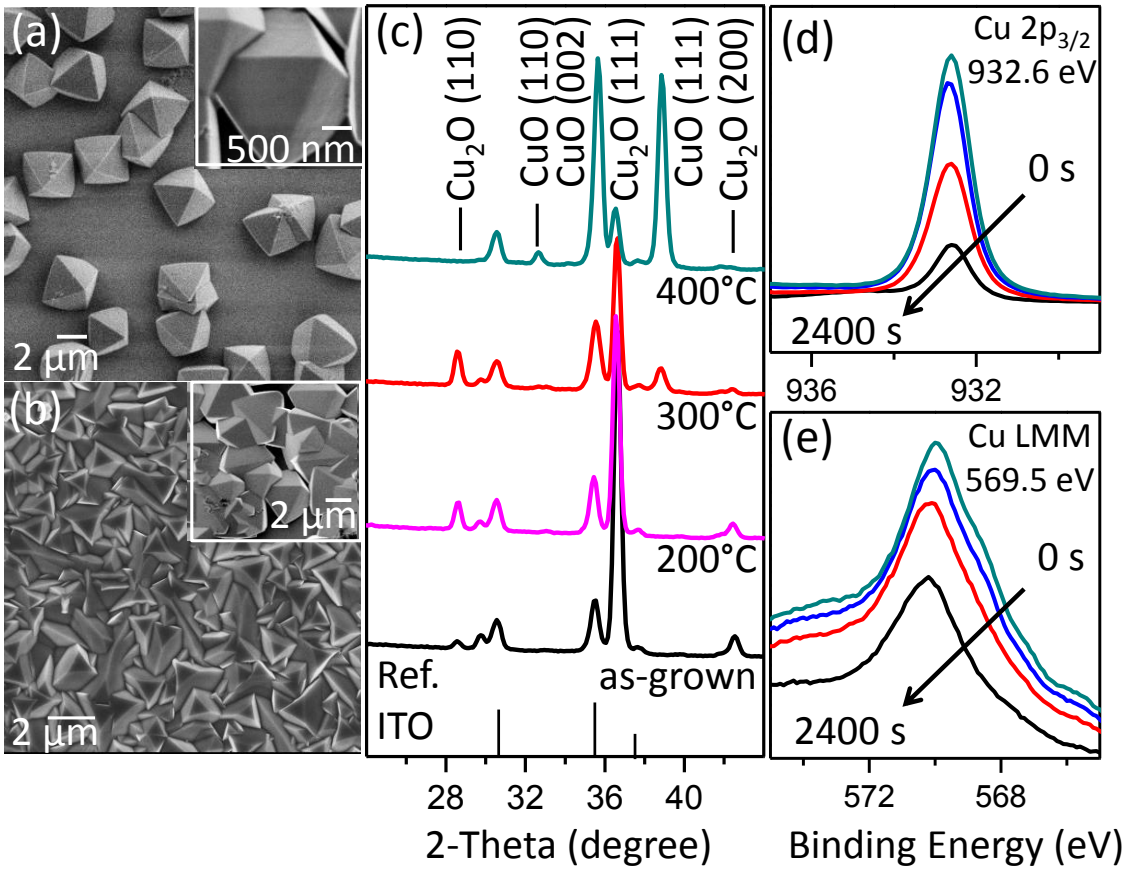

Figure 4.1 (a) SEM image of a Cu_2O film electrodeposited for 600 s at room temperature, with a magnified view of their octahedral structure shown in inset, and (b) HIM image of a thicker Cu_2O film electrodeposited for 900 s at room temperature followed by annealing at 200°C, with a magnified view of the as-deposited film before annealing shown in inset. (c) Glancing-incidence X-ray diffraction patterns of the as-deposited Cu_2O film in (a) and upon annealing to 200, 300, and 400°C for 30 min, with individual features assigned in accord with the reference profiles for Cu_2O (JCPDS 030653288) and CuO (JCPDS 030652309). The reference profile for the ITO substrate (JCPDS 010894596) is given as a bar graph. XPS spectra of (d) Cu $2p_{3/2}$, and (e) Cu LMM regions collected for the Cu_2O film in (a) and upon sputtering for 0, 200, 500, and 2400 s.

One of the main challenges in the Cu_2O/ZnO solar cell system is the low charge carrier concentration with lower mobility in the Cu_2O absorber layer. Here, we improve the electrodeposited Cu_2O thin film by simple annealing in order to enhance its conductivity with a larger charge carrier concentration. [Since annealing is performed on the whole device (discussed below), the annealing process could also affect the underlying ZnO nanostructured and seed layer films. The effect of annealing at different temperature on the as-deposited ZnO films has been investigated in earlier studies, [201,202,203] with most of which focusing on higher annealing temperature above 400°C and only a few on annealing temperature below 500°C [204]]. In the latter work, the influence of lower-range annealing temperature on ZnO and Aluminum doped ZnO (AZO) films grown onto a glass substrate using sol-gel spin coating method was investigated. The effect of increasing the annealing temperature from 100 to 400°C has proven to improve the crystallinity and the optical transmittances in the ZnO and AZO films, while minimizing oxygen vacancy defects at the grain boundaries. Figure 4.2a shows the topographical image of the electrodeposited 900-s Cu_2O film post-annealed at 200°C for 30 min. The conductive AFM image is consistent with the half pyramidal morphology found for the thicker film in the HIM image (Figure 4.1b, inset). Their corresponding current-voltage curve shown in Figure 4.2b exhibits a typical diode behavior with the film conductivity up to a few nA at different potentials. Three selected measurement locations on the sample were investigated, and the corresponding current-voltage curves all show the repeated cycling of the diode behavior but with various intensities likely due to different surface roughness arising from slight thickness variation of the nanostructured Cu_2O film. Figures 4.2c and 4.2d depict the carrier concentration and resistivity of the as-prepared film as a function of the post-anneal temperature, respectively. Evidently, the film post-annealed at 200°C exhibits the highest charge carrier concentration (1.0×10^{14} cm^{-3}, Figure 4.2c) and the lowest resistivity (8.3 μΩ cm, Figure 4.2d). This demonstrates that post-annealing at 200°C could significantly improve the photovoltaic performance.

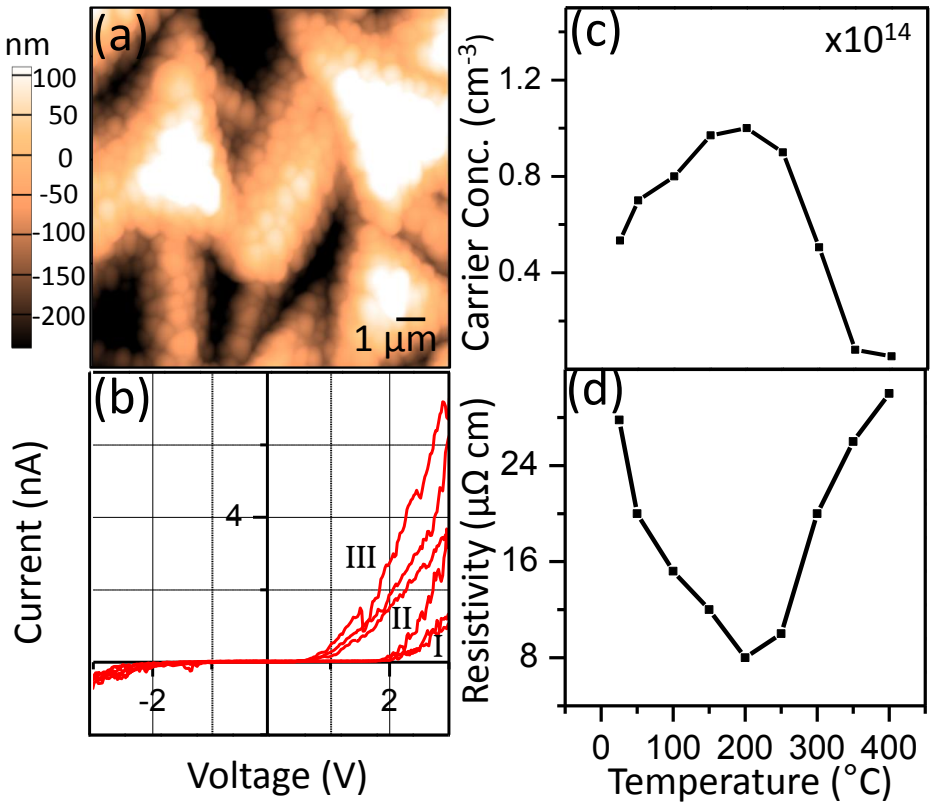

Figure 4.2 (a) Conductive AFM topographical image of a thicker Cu_2O film as electrodeposited for 900 s, and (b) the corresponding current-voltage profile exhibiting typical repeated diode behavior for three different locations on the sample. Hall-effect measurements of (c) carrier concentration and (d) resistivity of the thin film (obtained by 900-s electrodeposition) before and after annealing at different temperatures from room temperature to 400°C for 30 min.

The reflectance spectra for the as-grown and the 200°C post-annealed films, shown in Figure 4.3a, appear similar to each other, except for the notable reduction in magnitude for the reflectance of the latter (12.5% at 560 nm) when compared to the former (17.5% at 540 nm). The generally higher reflectance magnitudes in the 500-800 nm range found for these two films indicate their superior anti-reflectance property, which is important to solar cell application. A discernible red shift in the reflectance spectrum is observed for the films post-annealed at 300°C and 400°C with cut-off above 700 nm, which is likely due to the presence of CuO structures. Figure 4.3b shows the respective Tauc plots, which relate the absorption coefficient α to the band gap E_g through the equation: $(h\nu\alpha)^{1/n} = A(h\nu - E_g)$, where h is the Planck's constant, ν is the photon frequency, A is a proportional constant,

and n describes the nature of the transition of the material that can be either direct or indirect and/or allowed or forbidden.[205] The acquired reflectance R is converted to the Kubelka-Munk function, $F(R) = (1-R)^2/(2R)$, which is proportional to the absorption coefficient. By plotting $[h\nu \bullet F(R)]^2$ against the photon energy hν (in eV or in 1239/λ with wavelength λ in nm), we estimate the band gap values for the as-prepared film (2.29 eV) and films post-annealed at 200°C (2.21 eV), 300°C (1.74 eV), and 400°C (1.60 eV) (Figure 4.3b). These values support the presence of pure Cu_2O, with a theoretical band gap of 2.1 eV, for the as-prepared and 200°C-annealed films.[206] The lower band gap values (and the corresponding higher cut-off wavelengths above 700 nm) found for the films post-annealed at 300 and 400°C confirm the presence of CuO mixed with Cu_2O.

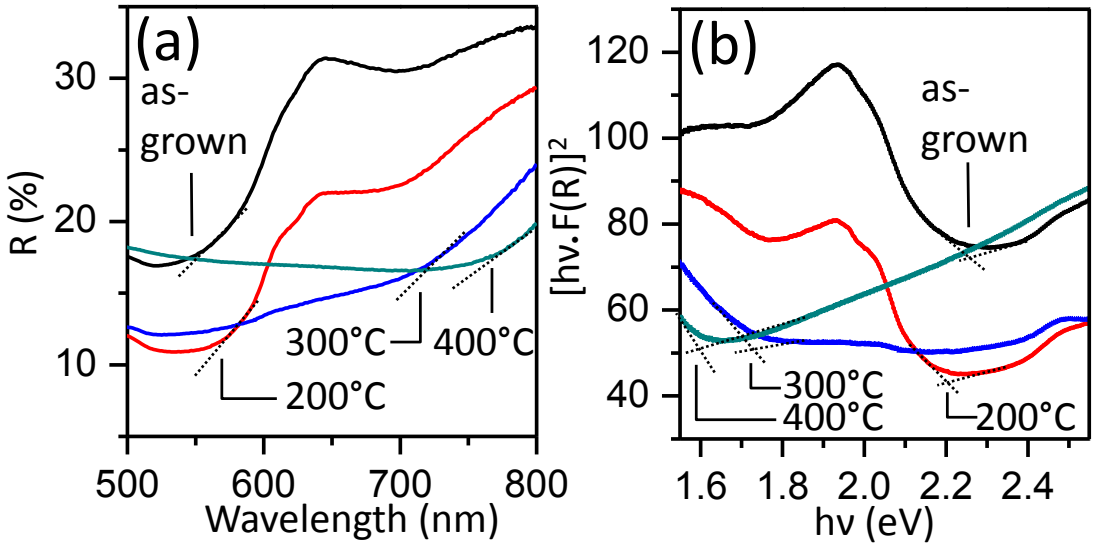

Figure 4.3 (a) Reflectance (R%) spectra and (b) the corresponding Tauc plots illustrating the bandgap estimation for the 900-s electrodeposited Cu_2O film before and after annealing to 200, 300 and 400°C.

4.3.2 Nano-heterojunction solar cell structure and their photovoltaic properties

Many studies have shown the major challenges encountered in fabricating Cu_2O/ZnO planar junction solar cell systems, especially due to their short charge carrier collection length that is limited by the low electron mobility in Cu_2O.[191] Many nanosystems have been proposed to obtain a higher junction area and more direct pathways of charge diffusion within the absorber layer by using one-dimensional ZnO nanostructures to further improve their charge collection.[185] The importance of optimizing both the ZnO seed layer thickness and the nanostructure length is investigated in an earlier study in order to minimize the leakage current and the interface area that limits their V_{OC} values.[189] However, these are not the only factors responsible for device performance. The thickness of the absorber layer could also play an important role, as suggested in a recent study that showed the open-circuit voltage, short-circuit current density, and consequently their overall PCE performance as functions of the Cu_2O thickness for both planar junction and radial junction solar cells.[192]

Here, we succeed in optimizing the performance by employing a Cu_2O layer with the appropriate thickness in the device structure. The ratio of built-in potentials at the junction interface of the n-type (V_n) and p-type materials (V_p) can be estimated by applying the Poisson's equation: $V_n/V_p = N_p\varepsilon_p/(N_n\varepsilon_n)$, where N_n (N_p) and ε_n (ε_p) are, respectively, the carrier concentration and the absolute permittivity of the electrodeposited n-type ZnO (p-type Cu_2O) film.[192] Since the highest charge carrier concentration from our Hall effect measurements is obtained for the Cu_2O film after annealing at 200°C is 1.0×10^{14} cm^{-3}, the thickness of the depletion region in the absorber layer (x_p) required to ensure a built-in potential as high as 0.7 V is approximately 2.5 µm, according to the equation: $V_p = ½\ qN_px_p^2/(2\varepsilon_p)$, where q is the electron charge. We have therefore electrodeposited a 2.5-µm thick Cu_2O film to completely encase the ZnO nanotubes or nanorods (with typical length of 1-1.5 µm and diameter of 200-500 nm) grown on top of a 500-nm thick ZnO seed layer. Figures 4.4a and 4.4b show the cross-sectional HIM images of both Cu_2O/ZnO-NT and Cu_2O/ZnO-NR solar cells, with the insets depicting the surface morphologies of these one-dimensional ZnO nanostructures before the Cu_2O film electrodeposition. Figure 4.4c shows the higher junction area expected for the Cu_2O/ZnO-NT cell structure compared to the Cu_2O/ZnO-NR cell, due to the inside surface of the nanotube. Figure 4.4e shows the cross-sectional SEM image across the entire Cu_2O/ZnO-NT/ITO device structure. The corresponding Auger electron spectrum of the entire image (Figure 4.4d) indicates the presence of both Cu LMM peak at 922 eV and Zn LMM peak at 997 eV. We also collect the Auger electron spectra at four different locations across the cell structure, as marked on

their corresponding SEM image shown in Figure 4.4e. These spectra confirm the highest Cu content at the top layer of the cell (Point 1), and reduced Cu content with the emergence of Zn at the junction area near the p-type absorber layer (Point 2). At the junction area around the nanostructures and near the ZnO seed layer (Point 3), a stronger Zn LMM peak and a weaker Cu LMM peak are observed. Finally, the absence of any Cu and Zn features is observed at ITO/glass substrate (Point 4).

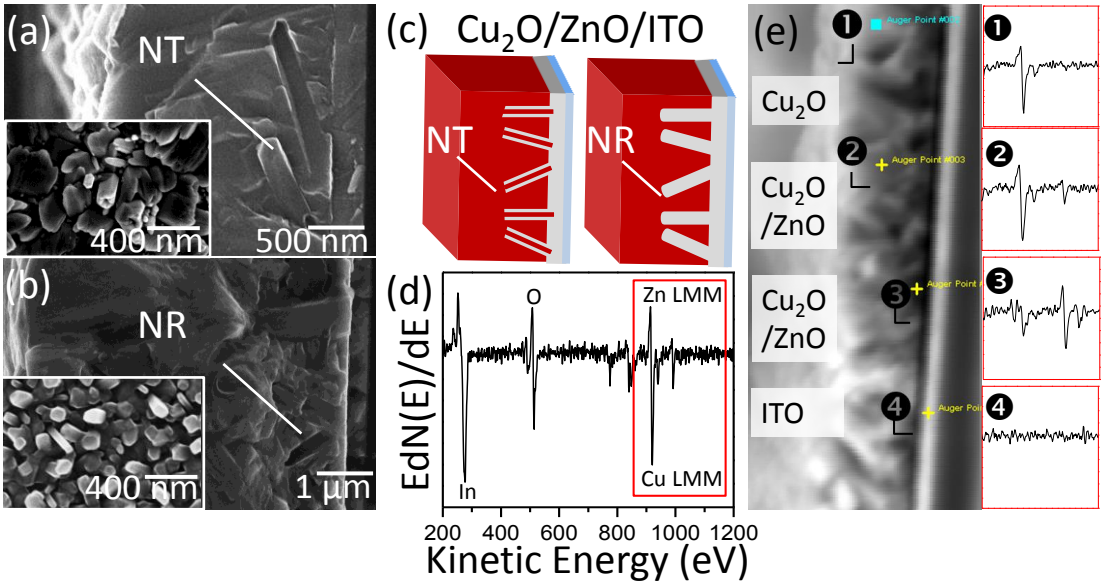

Figure 4.4 Cross-sectional HIM images of (a) Cu_2O/ZnO-NT and (b) Cu_2O/ZnO-NR solar cells, with insets depicting the electrodeposited ZnO nanostructures before the deposition of the 2.5-µm thick Cu_2O film. (c) Schematic diagrams of the Cu_2O/ZnO-NT and Cu_2O/ZnO-NR cell structures. (d) Auger electron spectrum and (e) cross-sectional SEM image of the junction area of the Cu_2O/ZnO-NT cell and the Auger electron spectra over selected energy region [red box in (d)] of the junction area at four different sample locations: (1) Cu_2O surface, (2) Cu_2O/ZnO junction, (3) Cu_2O/ZnO junction near to the ZnO NT, and (4) the ITO/glass substrate

Figures 4.5a shows the schematic diagrams of our optimized Cu_2O/ZnO-NT and Cu_2O/ZnO-NR heterojunction device structures. This optimal device structure consists of a 2.5-µm thick Cu_2O film encasing ZnO NTs or NRs, with typical lengths of 1-1.5 µm and diameters of 200-500 nm, on a 500-nm thick ZnO seed layer grown on an ITO/glass substrate. A gold contact is also sputter-coated on the Cu_2O film for evaluating the device performance. The corresponding energy band diagram of the whole device is also shown in Figure 4.5a. Figure 4.5b shows the photovoltaic current density vs

voltage (or J-V) curves for the Cu_2O/ZnO-NT and Cu_2O/ZnO-NR cells. When compared to V_{OC} of 0.59 V reported for other cells made up of Cu_2O on sparse ZnO NRs,[23] the present value (0.71V) represents the highest V_{OC} reported to date for this type of Cu_2O/ZnO-NR cells under no vacuum conditions. This may be due to the new configuration of the ZnO nanostructures grown on top of the ZnO seed layer, which ensures the full built-in potential at the absorber layer with thickness of 2.5 μm. In addition, the Cu_2O/ZnO-NT cell exhibits a much higher J_{SC} (2.40 mA/cm^2) than the Cu_2O/ZnO-NR cell (1.12 mA/cm^2), which is in good accord with the larger junction area and better charge carrier collection property observed for junction devices based on tubular nanostructures. However, the V_{OC} of the Cu_2O/ZnO-NT cell (0.66 V) is lower than that of the Cu_2O/ZnO-NR cell (0.71V), which may also be due to some additional recombination loss within the larger junction interface.

External quantum efficiency (EQE) measurements have also been performed for the Cu_2O/ZnO-NT and Cu_2O/ZnO-NR cells. As shown in Figure 4.5c, the EQE of the two devices are similar in magnitude at wavelength below 350 nm, but significantly different at longer wavelengths. The high EQE profile for the Cu_2O/ZnO-NR cell below 460 nm could be correlated with its high open circuit values, this could be due to the higher charge collection efficiency of the photogenerated charges near the interface of the radial junction.[207] As shown in an earlier study for improving the Cu_2O/ZnO radial heterojunction solar cell, the optical depth of the Cu_2O absorber layer is less than 150 nm for wavelength below 460 nm, indicating that all photons are absorbed near to the interface and can be easily collected by radial compared to planner junction. However, at longer wavelengths the optical depth increases up to many microns where the photogenerated charge carriers are too far from interface.[208]

On the other hand, the decrease of the EQE profile is consistent with the lower V_{OC} value (0.66V) in wavelengths below 460 nm for the Cu_2O/ZnO-NT cell compared with Cu_2O/ZnO-NR cell; this could be related to a possible additional recombination process loss at the higher junction area. Alternatively, for longer wavelengths above 460 nm, photons would be able for a deeper penetrating in the absorber layer; consequently the EQE values are more affected by the bulk Cu_2O properties and would therefore be independent of the open-circuit voltage with a discernible broadening of the EQE profile for the Cu_2O/ZnO-NT cell compared to the Cu_2O/ZnO-NR cell.[209] The observed broadening would result a better matching with the AM 1.5 solar spectrums at longer wavelengths that would consequence a higher J_{SC} and an improved overall PCE. The enhanced photocurrent production value

of the Cu_2O/ZnO-NT cell is consistent with our measured current density-voltage characteristic parameters as shown in Figure 4.5b. However, the short-circuit current density (less than 3 mA/cm^2) is still limited and considerably lower than the theoretical value (15 mA/cm^2) expected from Cu_2O/ZnO heterojunction. This is likely due to the poor charge carrier collection efficiency and the possible defects with interfacial electronic traps created on ZnO nanostructure films after the subsequent electrodeposition of Cu_2O films at highly alkaline electrolyte, all of which would limits the device performance. The large room for improvement calls for additional effort to better optimize the vertical alignment and spacing among the nanostructures, which may lead to better charge carrier collection and higher short-circuit current density.[192] Further work is therefore needed in optimizing the spatial, geometrical and orientational arrangement of the nanostructures on the support by using nanotemplating and nanolithography techniques, in order to facilitate better charge collection and to enhance their overall performance.

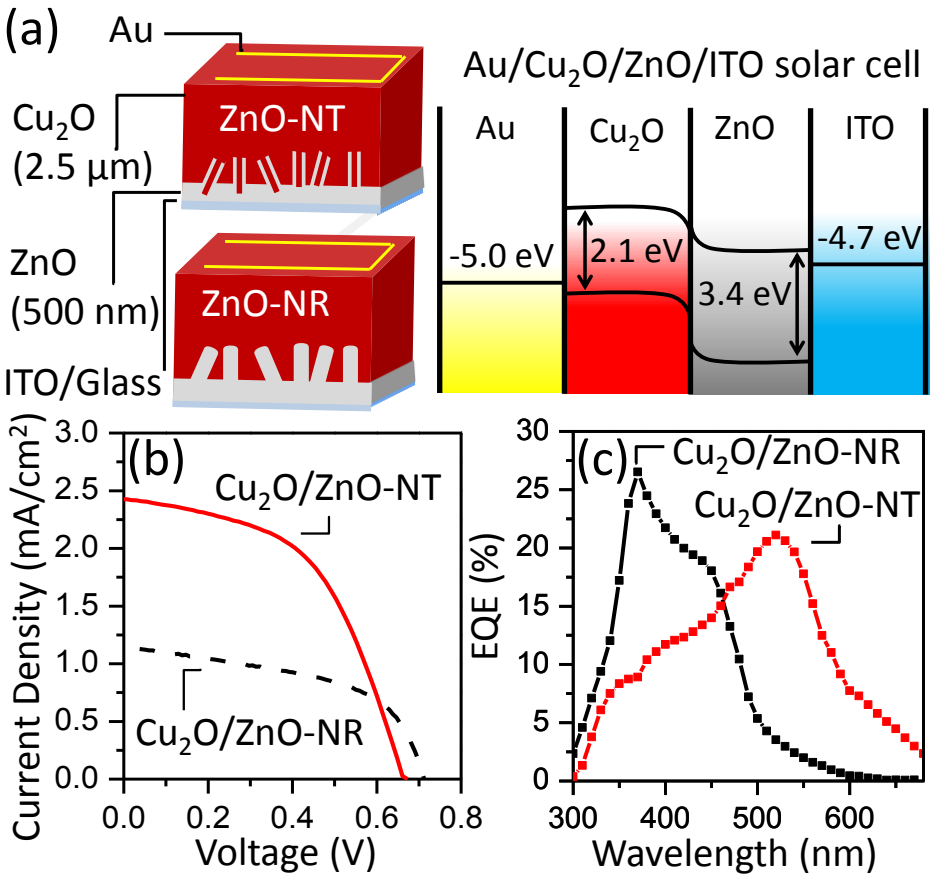

Figure 4.5 (a) Schematic diagrams of Cu_2O/ZnO-NT and Cu_2O/ZnO-NR solar cell structures, with their optimized layer thicknesses in parentheses, along with their corresponding energy band diagram. (b) Current density vs voltage curves and (c) external quantum efficiency (EQE) spectra of the Cu_2O/ZnO-NT and Cu_2O/ZnO-NR solar cells.

4.4 Conclusions

Nanoscale material manipulation is an attractive approach to improve the solar energy harvesting and to achieve more efficient photon-to-electron conversion for inorganic heterojunction photovoltaic devices. A heterojunction solar cell composed of a n-type ZnO nanostructured thin film (of nanotubes or nanorods) and incorporated with a p-type Cu_2O thin film of appropriate thickness is obtained by using a facile electrodeposition method. The open-circuit voltage is enhanced by post-

annealing the p-type Cu_2O nanostructured film at 200°C to obtain a better crystallinity and a higher conductivity, and by optimizing the film thickness to assure the full built-in potential across the junction interface. Furthermore, tubular ZnO nanostructures grown on the top of a sufficiently thick ZnO seed layer prevents any leakage pathway and improves their interface quality, which consequently increases their open-circuit voltages. Synthesis of the tubular nanostructure by electrodeposition also helps to minimize the recombination loss expected from undesirable defects in these tubular structures prepared by other means, such as etching of nanorods. Enhanced short-circuit current density is also observed for these tubular nanostructures due to their superior junction surface area and better charge carrier collection efficiency, and this consequently leads to better overall performance.

Chapter 5

Plasmonic Gold Nanoparticles for ZnO Nanotubes Photoanode in Dye Sensitized Solar Cell Application

5.1 Introduction

Nanoplasmonics is a rapidly growing research field that exploits enhancement of concentrated optical energy on the nanoscale in nanostructured metal systems arising from their surface plasmon modes.[210,211,212,213] Recently, gold nanoparticles (GNPs) have been introduced to different materials to improve their sensing, photocatalytic, and optical properties.[214,215,216] One of the major applications that take advantage of their improved light absorption capability specifically in the visible region is photovoltaics.[217,218,57,219] Surface modification with plasmonic nanoparticles was first introduced to photovoltaics for enhancing inorganic thin-film solar cells, particularly by compensating the loss of absorption with reduction in the absorber thickness.[220,221,222,223,224] Furthermore, GNPs have been used in both polymer-based and dye-based organic photovoltaics to provide a significant improvement in their performance.[225,226,227,228,229]

In a typical dye-sensitized solar cell (DSSC), the dye molecules adsorbed on the photoanode surface are the main photon absorber that can be excited, which results in the injection of their excited electrons into the conduction band of the semiconductor material. The injected electrons are easily transported from the photoanode via the back contact (usually made up of a transparent conductive oxide material) to the Pt counter electrode. The process can be repeated by simple regeneration of the dye molecules using a redox couple ($3I^-/I_3^-$) liquid electrolyte, followed by reduction of the electrolyte with the catalytically active Pt electrode.[81] Au-SiO_2 core-shell NPs have been used as plasmonic light harvesting antenna on a TiO_2 NP photoanode for liquid and solid-state based DSSCs. An improved efficiency approaching 1.95% (from 1.05%) was obtained for the N719 dye with the ($3I^-/I_3^-$) liquid electrolyte in a liquid-based DSSC. [230] An efficiency enhancement approaching 2.2% (from 1.2%) was also obtained when the Z907 dye was employed for solid-state based DSSCs.[230]

Recently, ZnO has been used as an alternative n-type semiconducting photoanode material for DSSCs, because of its similar bandgap, higher electron dynamics, and versatile nanostructural morphology relative to TiO_2.[168,231,232,193] Further modifications have been performed by mixing with other nanostructured metal oxides (such as TiO_2 and SnO_2) or with metallic NPs (including Au and

Ag) for improving their charge carrier and absorption properties for DSSC application.[233,234,235,236] Coating of vertically aligned ZnO nanorods with GNPs using an "all-hydrothermal" method was reported to increase the photon conversion efficiency from 0.7% to 1.2%, along with an increase in its open-circuit voltage from 0.50 to 0.63 V.[237]

Here, we develop a successive electrodeposition procedure to decorate with GNPs the high-surface-area ZnO NTs, also obtained by direct electrodeposition, and demonstrate its advantage as an effective DSSC photoanode. As electrodeposition is capable of preparing high-quality nanomaterials with better crystallinity and minimum lattice mismatch, the resulting enhanced interface quality could also improve the contact of GNPs on the ZnO NT surface. This leads to lower resistance for better electron conduction that is important for advanced electronic device applications. The GNP particle size can be easily optimized with different concentrations of $AuCl_3$ in $NaClO_4$ mixed with 0.1 M KCl electrolyte, while its areal density can be controlled by the deposition time at a selected $AuCl_3$ concentration (1 mM). Our results illustrate the many advantages of our all-electrochemically-grown GNP/ZnO-NT photoanode, as provided by their better capacity for dye loading and higher charge transport inherent in the one-dimensional, high-specific-surface-area ZnO NTs, and by the pronounced enhancement in their absorption due to surface plasmonic effect of the GNPs. With the Schottky barrier build up at the Au/ZnO interface, a higher electron density is also obtained at the ZnO conduction band due to the reduction of electron-transfer resistance and minimization of recombination loss by blocking the back electron transfer from ZnO to the electrolyte or/and the dye molecules. An almost 28% increase in the overall efficiency from 4.7% for pristine ZnO-NT DSSC to 6.0% for GNP/ZnO-NT DSSC can be achieved.

5.2 Materials and Methods

For all sample preparation, we employed a three-electrode electrochemical cell, with an ITO-glass working electrode, an Ag/AgCl reference electrode, and a Pt-wire counter electrode in an electrochemical workstation (CH Instruments 1140). The preparation of ZnO NTs on ITO-glass substrates by electrochemical deposition has been discussed in detail elsewhere (as discussed in Chapter 3).[193] Briefly, delicately controlling the electrolyte conductivity with different mono and divalent supporting electrolytes in the same 0.5 mM $ZnCl_2$ primary electrolyte, we showed that it was possible to manipulate the growth mechanism and to obtain directly electrodeposited ZnO nanotubes. Gold nanoparticles were then electrodeposited on ZnO NTs in an aqueous solution of 1 , 5, or 10 mM

$AuCl_3$ dissolved in 0.1 M $NaClO_4$ and 0.1 M KCl by potentiostatic amperometry (at –1 V vs Ag/AgCl) at room temperature for 60 s. After deposition, the as-prepared samples were rinsed thoroughly in deionized water and stored in a nitrogen atmosphere to dry for at least 24 hours prior to characterization.

The surface morphologies were examined by using helium ion microscopy (HIM) in a Zeiss Orion Plus microscope and field-emission scanning electron microscopy (SEM) in a Zeiss Merlin microscope. Bright-field low-resolution and high-resolution transmission electron microscopy (TEM) studies were performed by using a Zeiss Libra 200 MC microscope on GNP/ZnO-NT nanostructures scraped off from the substrate and transferred onto a lacey carbon TEM grid. The corresponding crystal structures were characterized by glancing-incidence X-ray diffraction (XRD) using a PANalytical X'Pert Pro MRD diffractometer with Cu Kα radiation (1.54 Å) at an incidence angle of 0.6°. The surface compositions of the GNP/ZnO-nanodeposits were analyzed by X-ray photoelectron spectroscopy (XPS) using a Thermo-VG Scientific ESCALab 250 Microprobe with a monochromatic Al Kα source (1486.6 eV). Cyclic voltammetry and electrochemical impedance spectroscopy were performed in 10 mM $K_3Fe(CN)_6$ in a PBS solution (pH = 7.4) using the same electrochemical workstation. The optical properties were investigated by using a Perkin Elmer Lambda 1050 UV/Vis spectrometer.

Typical DSSCs were fabricated using a standard procedure.[166] After the preparation of GNP/ZnO-NT on an ITO-glass substrate, the photoanode was annealed at 130°C for 30 min to improve their dye loading property and their contact with the substrate. The working electrode was constructed by dipping the resulting GNP/ZnO-NT photoanode in a 0.5 mM solution of commercial dye N719 (purchased from Sigma Aldrich) for 2 h. The counter electrode was obtained by sputter-coating a Pt thin film (200 nm thick) on another ITO-glass substrate. A redox ($3I^-/I_3$) couple electrolyte was then sandwiched between the working and counter electrodes to create the DSSC. The current density vs voltage (J-V) characteristics were analyzed using a solar cell I-V measurement system (PV Measurements IV5) equipped with a class ABA solar simulator and an Air Mass (AM) 1.5 global spectral filter. Prior to the J-V measurement, the system was calibrated using a Si reference cell (PVM782 with a BK7 window).

5.3 Results and Discussion

5.3.1 Characterization of GNP/ZnO-NT photoanode

Figure 5.1 shows the SEM images of ZnO NTs electrochemically grown on an ITO-glass substrate with and without subsequent electrodeposition of GNPs for 60 s. The resulting ZnO NTs are typically 1-1.5 μm long and 200-500 nm in diameter (Figure 5.1a). Different gold electrolyte concentrations have been used for electrodepositing GNPs to obtain different nanoparticle size. At the lowest concentration of 1 mM employed in the present study (Figure 5.1b), homogenous coverage of GNPs on both the inside and outside surfaces near the tip of the ZnO NT is observed. These GNPs also exhibit a fairly uniform spatial distribution on their surface along the length of the nanotube, with an average particle size of 12 nm. Increasing the electrolyte concentration to 5 mM (Figures 5.1c, 5.1d) produces a higher aerial density and larger GNPs with an average size of 20-50 nm along the entire ZnO NT length. At the highest concentration of 10 mM (Figures 5.1e, 5.1f), we observe even larger GNPs with average size over 50 nm. Interestingly, the larger GNPs (> 30 nm) obtained with the latter two concentrations also tend to agglomerate on the surface along the length of the ZnO NT, leading to high or even complete coverage of the ZnO NT surfaces, in contrast to that found for the lowest concentration (1 mM). As GNPs could also be electrodeposited on a pristine ITO-glass substrate (i.e. without any ZnO NTs), a seed layer of ZnO is pre-electrodeposited prior to the growth of the ZnO nanostructures to ensure that pristine ITO-glass or GNPs on ITO-glass is not involved in the photovoltaic process.

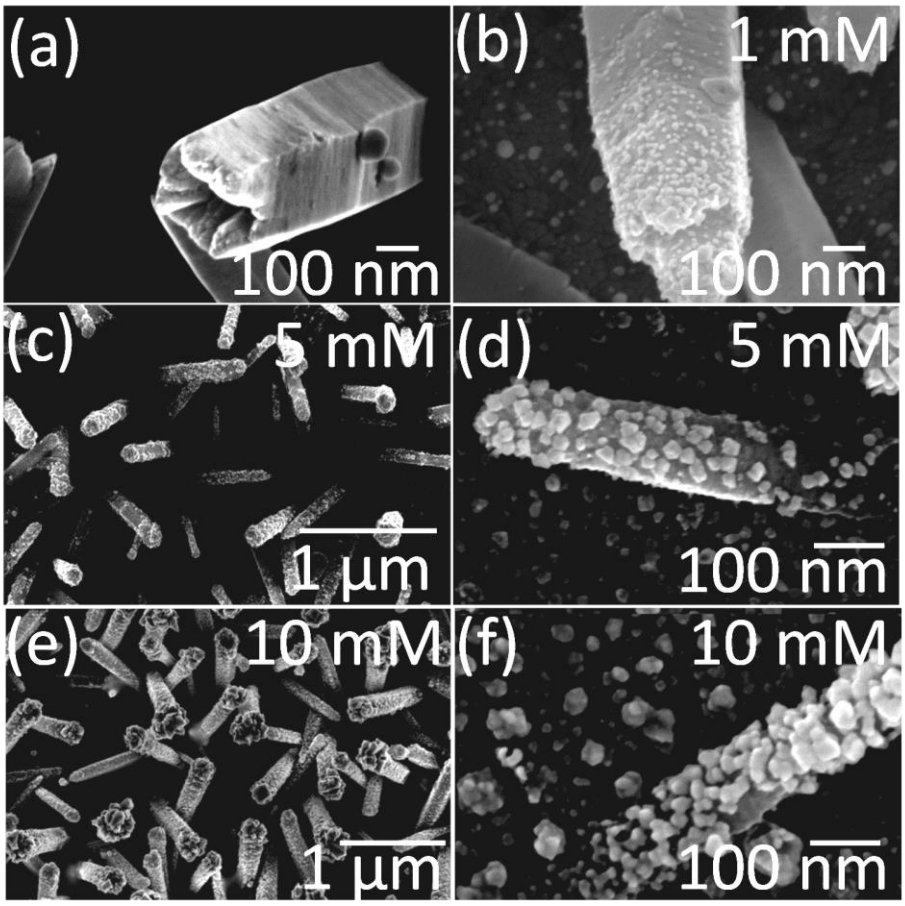

Figure 5.1 SEM images of (a) pristine ZnO-NT, and GNP/ZnO-NT obtained by GNP electrodeposition in (b) 1 mM, (c, d) 5 mM, and (e, f) 10 mM $AuCl_3$ electrolytes, all mixed with 0.1 M $NaClO_4$ and 0.1 M KCl supporting electrolyte, at room temperature.

Taking advantage of the higher surface contrast and the superior depth of focus of helium ion microscopy, we study the aerial density of GNPs grown on the ZnO NT surfaces, which can be easily increased by increasing the deposition time. As illustrated by the HIM images for GNPs obtained with the 1 mM $AuCl_3$ electrolyte solution, the aerial density of GNPs on ZnO NT is significantly higher for 300 s (Figure 5.2b) than that for 30 s (Figure 5.2a) and that the spatial distribution of GNPs remains uniform on the NT surface. Energy dispersive X-ray elemental analysis has been performed on the GNP/ZnO-NT samples obtained with GNP deposition time of 30, 60, 120, 200, and 300 s. Figure 5.2c inset shows that a higher relative intensity of Au peak for the GNP (with respect to the relatively constant Zn and O peak intensities) is obtained for the 300-s deposition, thus confirming the increase of GNP areal density with increasing deposition time. However, the higher deposition time

(> 300 s) is also found to slightly decrease in their light absorbance in the visible region, as shown in their UV/Vis absorption spectra in Figure 5.3, which is likely due to particle aggregation. To maximize the total surface area of GNPs in order to facilitate maximal loading of the dye in the DSSC fabrication, we select the GNP/ZnO-NT sample deposited with a near-monolayer coverage of the smallest GNPs but with the largest aerial density, i.e. that obtained by the 300-s deposition (Figure 5.2b).

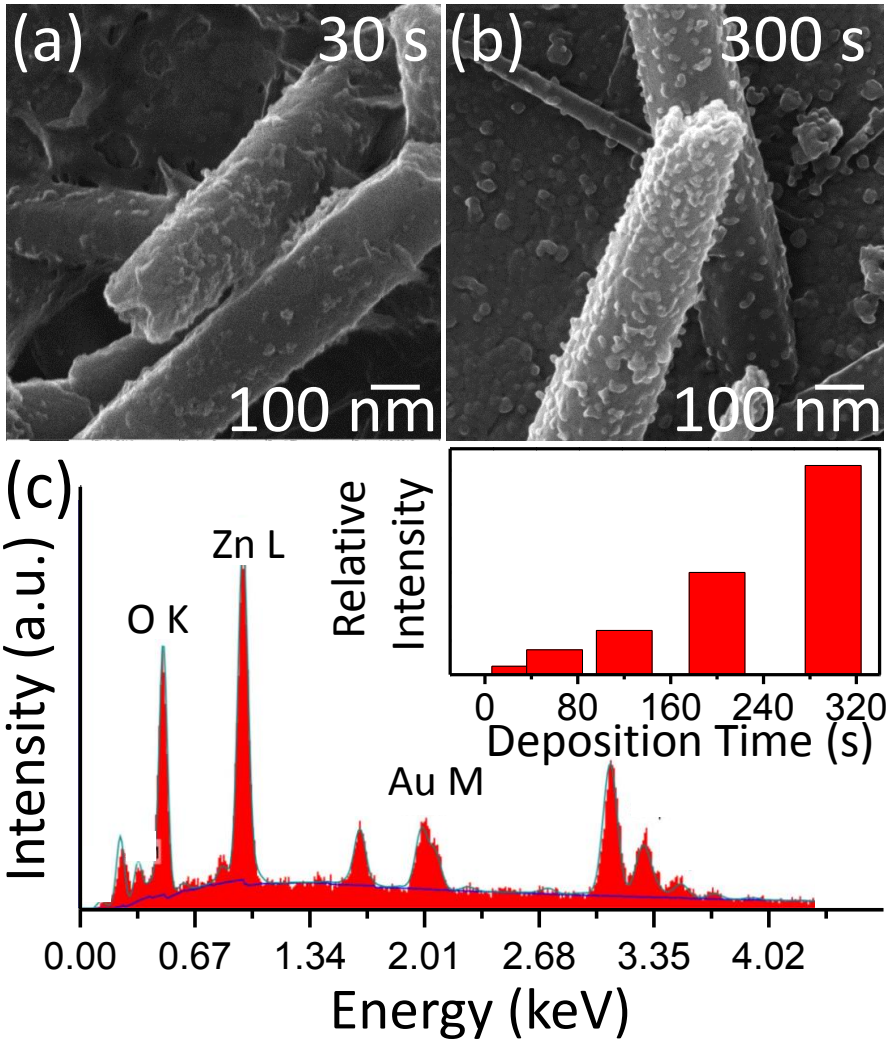

Figure 5.2 HIM images of ZnO nanotubes electrodeposited with Au nanoparticles in 1 mM $AuCl_3$ electrolyte for (a) 30 s and (b) 300 s. (c) Energy dispersive X-ray spectrum for the ZnO nanotubes decorated with gold nanoparticles obtained by 300-s deposition, with the inset depicting the relative intensity change of Au M emission feature with respect to Zn L feature for gold nanoparticle deposition of 30, 60, 120, 200, and 300 s.

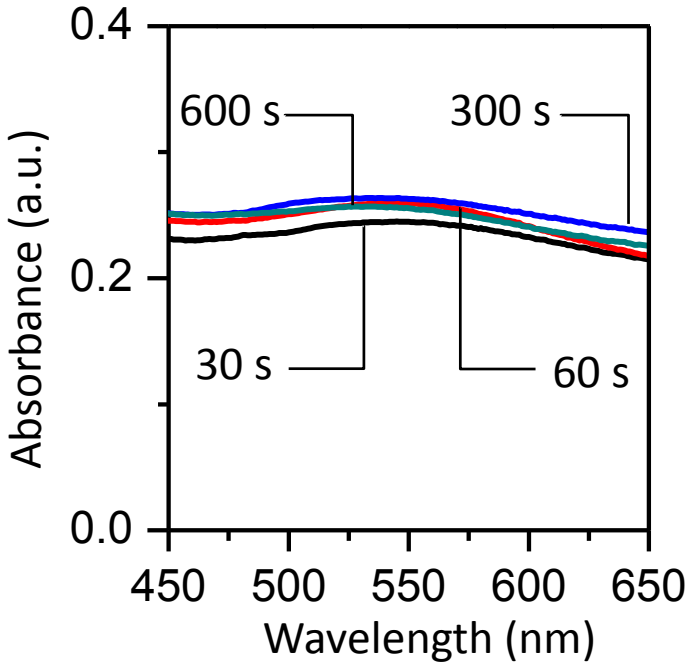

Figure 5.3 UV/Vis absorbance spectrums of GNP/ZnO-NT photoanodes at different deposition time of 30, 60, 300, and 600 s, show the similar absorbance at deposition time (> 300 s) at the visible regime.

The low-magnification TEM image for the GNP/ZnO-NT photoanode shown in Figure 5.4a confirms the existence of the GNPs as-electrodeposited on the ZnO-NT surface with a particle size distribution of 4-22 nm and an average size of 12 nm (Figure 5.4a, inset). The corresponding high-resolution TEM images for ZnO NT (Figure 5.4b) and GNP (Figure 5.4c) reveal sharp fringes with respective spacings of 0.25 nm and 0.24 nm, which are in good accord with the respective interplanar separations for the ZnO(101) and Au(111) planes. This is also in good agreement with the glancing-incidence XRD pattern of the GNP/ZnO-NT photoanode shown in Figure 5.4d. Despite the strong XRD peaks from the ITO substrate, we observe well-defined Au XRD features for (111) at 38.1°, (200) at 44.3°, (220) at 64.5°, and (311) at 77.5°, which are consistent with the reference pattern for the face centered cubic structure of Au (JCPDS 030652870). The weaker peaks at 31.7°, 34.4°, 36.2°, 47.5° and 56.6° correspond, respectively, to the (100), (002), (101), (102) and (110) planes of ZnO, in good accord with the reference pattern for the hexagonal wurtzite structure of ZnO (JCPDS 010790206). The higher intensity ratio for ZnO(101) to ZnO(100) found for the ZnO NTs relative to that for ZnO powder (as shown in the reference pattern) indicates a preferred ZnO growth direction

along the [101] direction. Similarly, the higher intensity ratio for Au(111) to Au(200) observed for the GNPs than that for the Au reference reflects preferential growth along the [111] direction for these GNPs, which is likely due to the good lattice match between the Au(111) and ZnO(101) planes.

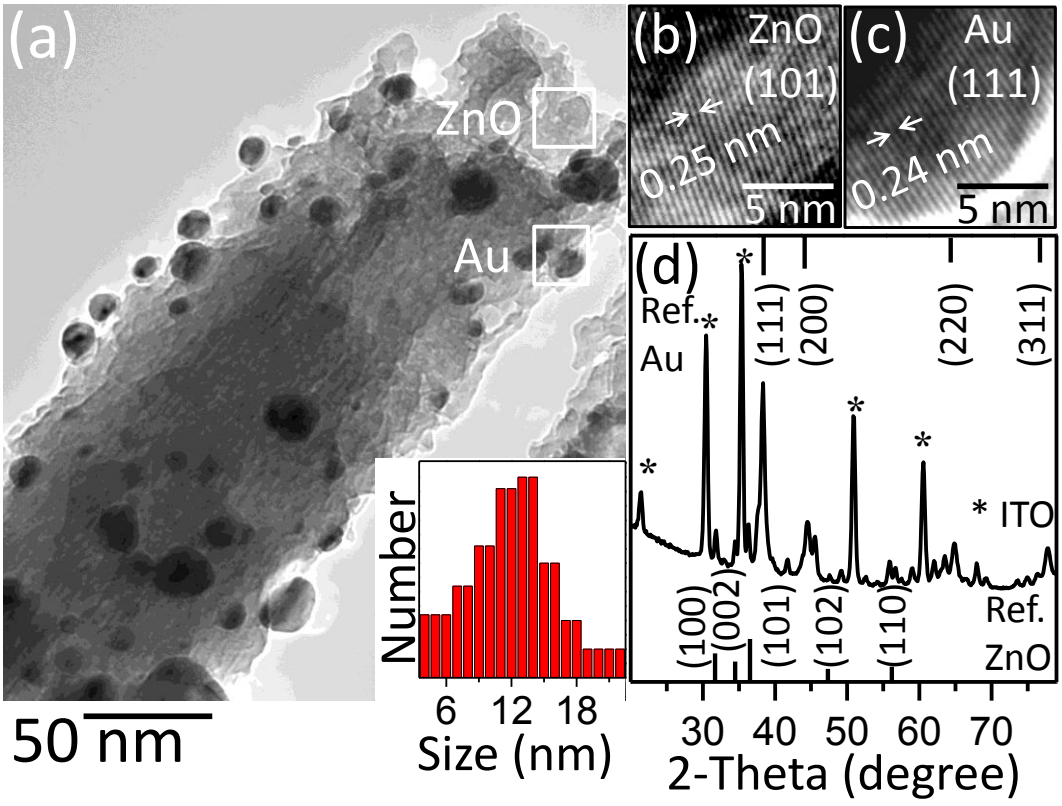

Figure 5.4 (a) Low-magnification TEM image of GNP/ZnO-NT, and high-resolution TEM images of (b) selected ZnO-NT and (c) GNP regions, revealing the respective fringe spacings for ZnO(101) and Au(111). (d) Glancing-incidence X-ray diffraction pattern of the GNP/ZnO-NT on ITO/glass substrate, along with the reference patterns for wurtzite ZnO (JCPDS 010790206) and FCC Au (JCPDS 030652870). The diffraction features for ITO are marked by asterisks.

Figure 5.5 shows the XPS chemical-state composition analysis for the GNP/ZnO-NT photoanode. The Zn $2p_{3/2}$ peak near 1021.8 eV corresponds to the Zn^{2+} oxidation state of ZnO (Figure 5.5a), while the O 1s peak at 530.2 eV and the weak shoulder at 531.1 eV can be attributed to ZnO and $Zn(OH)_2$, respectively (Figure 5.5b). The metallic form of the GNPs is confirmed by the presence of the Au $4f_{7/2}$ ($4f_{5/2}$) feature at 83.8 eV (87.5 eV) (Figure 5.5c). [162,238]

Further electrochemical characterizations for GNP/ZnO-NT photoanode have also been performed using 10 mM $K_3[Fe(CN)_6]$ in a 10 mM PBS (pH = 7) at room temperature, and the results are compared with those for pristine ZnO-NT photoanode (i.e. without any GNP deposition). The cyclic voltammograms shown in Figure 5.5d indicate that both oxidation and reduction currents for GNP/ZnO-NT are considerably larger than those for pristine ZnO-NT. In the electrochemical cell, electrons enter the electrolyte solution and the metal ions start to diffuse into the electrolyte upon dissolution. The rate of charge migration depends on the charge-transfer resistance inside the electrolyte solution. When ZnO NTs are decorated with GNPs, significant enhancement in both oxidation and reduction currents can be observed. The higher current at a fixed potential found for the GNP/ZnO-NT photoanode is due to a lower charge-transfer resistance, when compared to pristine ZnO-NT. Further confirmation is obtained from electrochemical impedance spectroscopy for both photoanodes. Figure 5.5e shows Nyquist plots for the GNP/ZnO-NT and pristine ZnO-NT photoanodes. The near-linear part at low frequency represents the diffusion-limited process, while the diameter of the semicircle at higher frequency is generally related to the underlying electron-transfer limited process. Using an equivalent circuit that includes the electrolyte resistance between the working and reference electrodes (R_s), Warburg impedance (Z_W), double-layer capacitance (C_{dl}) and the charge-transfer resistance (R_{ct}) to model the observed curves, we determine R_{ct} values for the GNP/ZnO-NT and pristine ZnO-NT photoanodes. [239] The smaller charge-transfer resistance for the GNP/ZnO-NT photoanode (1.60 kΩ) than that for the pristine ZnO-NT photoanode (1.98 kΩ) indicates a more efficient charge-transfer process for the GNP/ZnO-NT photoanode than the pristine ZnO-NT photoanode. The enhanced charge-transfer process confirms that the formation of Schottky diode at the Au/ZnO interface is having a significant effect on the photovoltaic performance.

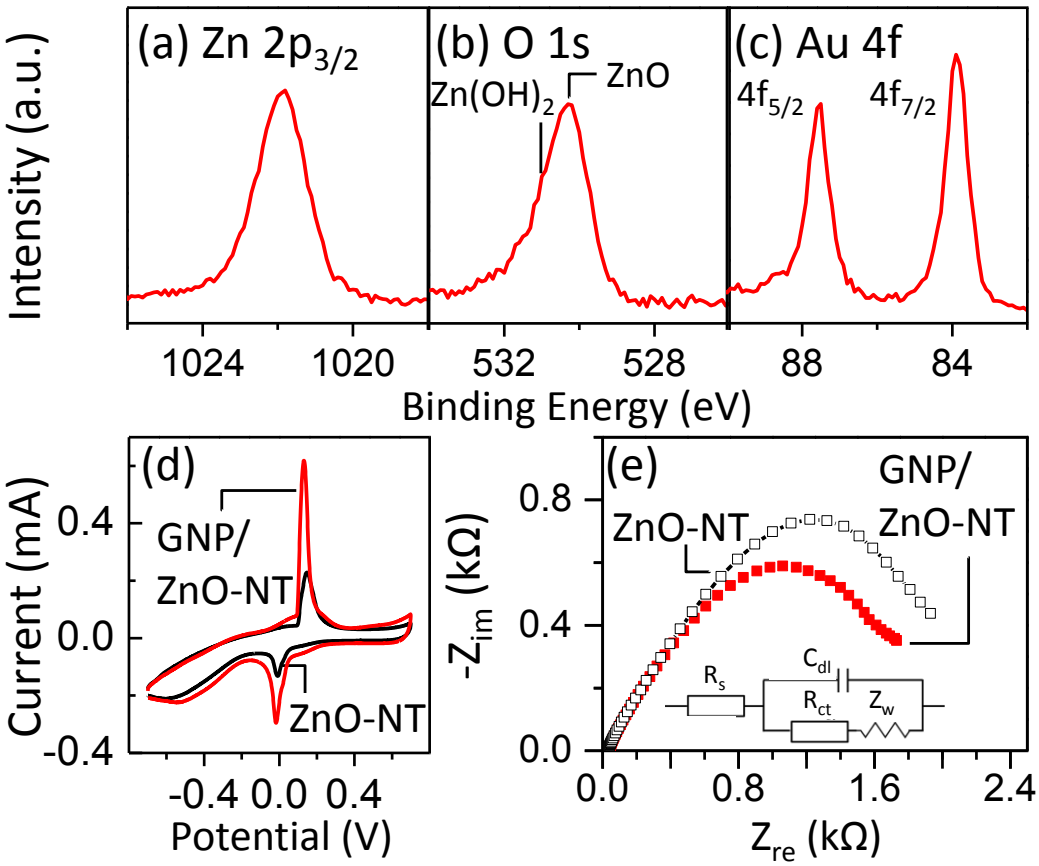

Figure 5.5 XPS spectra of (a) Zn $2p_{3/2}$, (b) O 1s, and (c) Au 4f regions for the GNP/ZnO-NT photoanode. (d) Cyclic voltammograms, and (e) Nyquist plots for the GNP/ZnO-NT and pristine ZnO-NT photoanodes, with an inset of their equivalent circuit model.

5.3.2 Comparison of photovoltaic performance of GNP/ZnO-NT vs pristine ZnO-NT photoanodes

Using the GNP/ZnO-NT photoanode and pristine ZnO-NT photoanode, we construct four different cell structures with and without the dye loading step. To investigate the cell performance, we first examine the photon absorption efficiencies of the two photoanodes. Figure 5.6a compares their UV-Vis absorption spectra, which show 25 % higher photon absorption for the GNP/ZnO-NT relative to pristine ZnO photoanode after dye loading. In Figure 5.6b, we compare the current density vs voltage performance of the solar cells constructed with the GNP/ZnO-NT and pristine ZnO-NT photoanodes in the absence of the N719 dye. Evidently, the short-circuit current density, open-circuit voltage, fill factor and photon conversion efficiency of the pristine ZnO-NT cell have increased, respectively, from 0.07 mA/cm^2 to 1.5 mA/cm^2, from 0.187 V to 0.385 V, from 0.27 to 0.49, and from 0.004% to 0.028% for the GNP/ZnO-NT cell. The higher photon absorption as a result of plasmonic effect introduced by the GNPs is therefore responsible for the discernible enhancement in the solar cell performance (even without the dye). Figure 5.6c shows that upon loading with the N719 dye, the short-circuit current density has increased from 10.4 mA/cm^2 for the pristine ZnO-NT cell to 13.1 mA/cm^2 for the GNP/ZnO-NT cell. The corresponding photon conversion efficiency has also increased from 4.7% for the former to 6.0% for the latter. This is a direct result of the higher photon absorption provided by the GNPs.

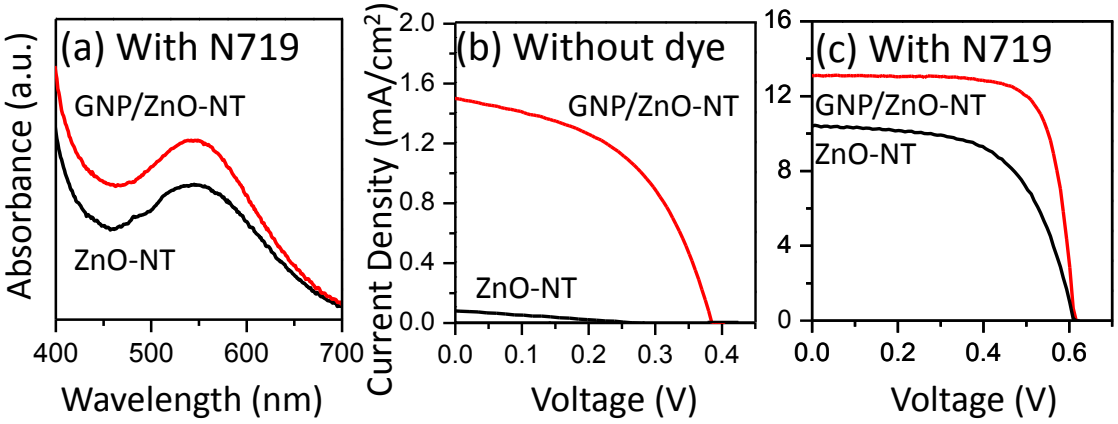

Figure 5.6 (a) UV-Vis absorption spectra of GNP/ZnO-NT and pristine ZnO-NT photoanodes with N719 dye, and the current density vs voltage curves for solar cells constructed from GNP/ZnO-NT and pristine ZnO-NT photoanodes (b) without and (c) with N719 dye.

The size dependence of the plasmon absorption of gold nanoparticles has been studied in earlier work, which showed that plasmonic Au NPs with an average particle size greater than 16 nm could provide a bigger enhancement at longer wavelength, while smaller NPs of 10 nm in size would have better absorption at shorter wavelength, especially in the visible regime. [240] The size dependence of the plasmon absorption of GNPs has also been investigated. Another study has also shown that smaller plasmonic silver nanoparticles, with an average diameter less than 25 nm in the intrinsic size regime, would exhibit an increased plasmon bandwidth. [241] In accord with these reports, our present results show that the best performance is observed for smaller GNPs (less than 25 nm) while GNPs larger than 30 nm have led to poorer cell performance. This is likely caused by the agglomeration of the larger GNPs, which reduces the total illumination area of the exposed surfaces of the NPs, and by filling of the ZnO tubular structures, which results in poor dye loading. In addition, smaller GNPs would produce a greater shift in the Fermi level due to the small electron accumulation in the GNPs. This is in contrast to the larger, agglomerated GNPs, which would require a larger electron build-up to cause an upward shift of the Fermi level and therefore a higher recombination loss of the accumulated electrons with the oxidized redox electrolyte and/or dye species (the process mechanism of which will be discussed below). Consequently, this would produce a lower photocurrent [242,243] and poorer overall performance as shown in Figure 5.7.

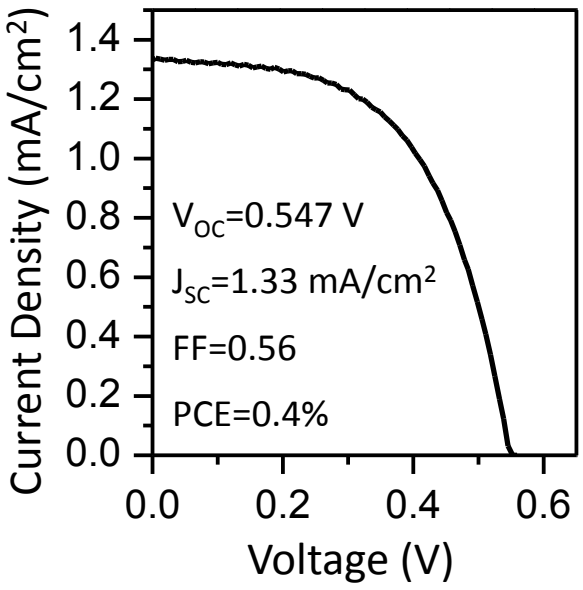

Figure 5.7 Current density vs voltage characteristic of GNP/ZnO-NT based DSSC with agglomerated GNPs obtained by using a high concentration of 10 mM $AuCl_3$ electrolyte.

The photon-to-electron conversion mechanisms using the GNP/ZnO photoanode without dye and that loaded with the N719 dye are shown schematically in Figure 5.8. The presence of GNPs would enhance photon absorption in the visible region. As for the case of GNP/ZnO photoanode without dye shown in Figure 5.8a, electrons are injected from the Au Fermi level to the conduction band (CB) of ZnO upon light illumination, which is responsible for the photocurrent so produced. On the other hand, when the GNP/ZnO photoanode loaded with the N719 dye (Figure 5.8b), electron injection into the ZnO conduction band could occur in two routes. The electrons generated from the photo-excited dye molecules, via a highest occupied molecular orbital (HOMO) to lowest unoccupied molecular orbital (LUMO) transition, could be transported directly to the ZnO conduction band. Alternatively, the generated electron could also be transferred indirectly to the deposited Au NPs first and then onto the ZnO NT surface. As a result of their electrons accumulation at the Au energy level, the Au Fermi level would be shifted upward toward the ZnO conduction band and hence resulting in buildup of a potential barrier at the metal/semiconductor interface. In addition, the existence of Schottky barrier would enhance the device performance due to the blockage of the back electron-transfer from the ZnO conduction band to the GNPs, [240] which would reduce the recombination loss that may occur between charge carriers (electrons) and any oxidized species of the redox electrolyte or dye molecules. The GNP/ZnO-NT system so constructed therefore provides a more efficient charge-transfer process with enhanced light absorption, thus leading to a better overall performance of GNP surface-modified photoanode. [214] Future work could be performed to optimize the vertical arrangement with fixed spacing of the nanostructures using nanotemplating and nanolithography techniques, in order to increase the charge collection property and to further enhance the overall performance. An additional step of coating the gold nanoparticles with a passivation layer of appropriately optimized thickness to prevent them from acting as charge recombination centers could also improve their overall efficiency.

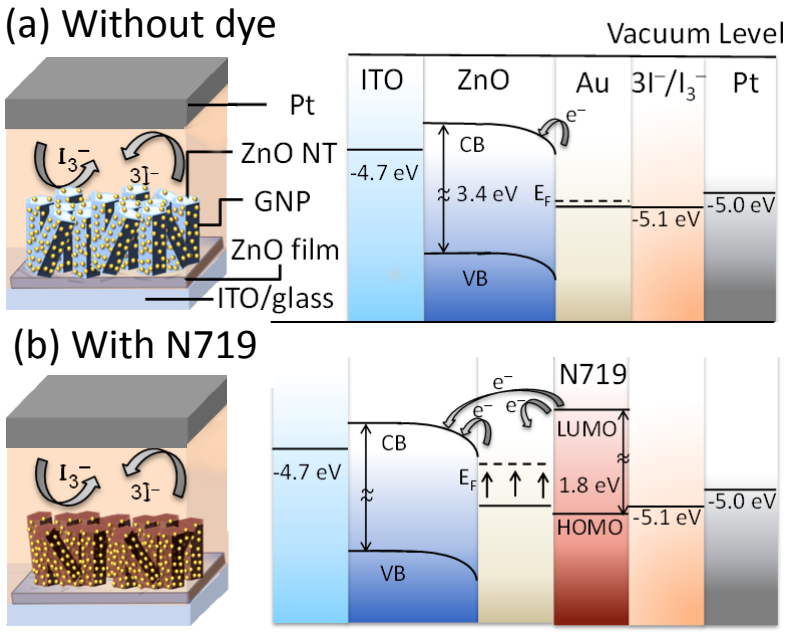

Figure 5.8 Schematic diagrams of the device architectures and corresponding energy band diagrams for solar cells constructed from GNP/ZnO-NT photoanode (a) without and (b) with N719 dye, illustrating the photon-to-electron conversion mechanisms.

5.4 Conclusions

By taking advantage of the plasmonic effect, appropriately sized GNPs electrodeposited on ZnO-NTs have provided significant enhancement to their performance in DSSC application. Here, we illustrate that two main enhancements could be achieved by an all-electrodeposition approach. First, a simple, direct electrodeposition technique has been used to deposit ZnO nanotubes, which provide a distinctly higher total surface area (with both inside and outside tubular surfaces) for superior dye loading. Second, electrodeposition is also used to control the deposition of GNPs of appropriate size that would manifest the plasmonic effect to maximize the optical improvement observed in the visible region. The formation of the interfacial Au/ZnO Schottky barrier also blocks the back electron-transfer from ZnO conduction band to the GNPs, thereby reducing the recombination loss involving oxidized dye and/or electrolyte molecules. These enhancements have led to an excellent photon conversion efficiency of 6%, with an open-circuit voltage of 0.61 V and a fill factor of 0.75.

Chapter 6

Hierarchical Tin Oxide Nanostructures for Dye-Sensitized Solar Cell Application[§§§§§]

6.1 Introduction

Dye-Sensitized Solar Cells (DSSCs) are promising devices for conversion of solar energy to electricity since the ground-breaking work of Gratzel.[81] During the last two decades, a massive amount of work has been done on TiO_2-based DSSCs, the photon-to-electron conversion efficiency (PCE) of which has been improved significantly, reaching as high as 10%. Recently, the use of alternative transparent conductive oxides, such as ZnO and SnO_2, have been reported for DSSC applications, due to their excellent optical transparency, wide direct band gap, high electron mobility, and large electron diffusion coefficient.[232,244] However, earlier studies have shown that ZnO could suffer from its lower chemical stability and dye loading capacity, which makes it less attractive as a photoanode in DSSC applications.[245] In contrast, SnO_2 has lower UV degradation characteristic with a band gap of 3.8 eV and generally better stability. One major challenge of SnO_2 is the faster recombination rate due to higher electron transport dynamics and low open circuit voltage (~400 mV), which limits the overall PCE.[246,247] Consequently, further modifications have been introduced on the surface of SnO_2 nanowires by decorating with TiO_2 nanoparticles[247] or coating with a compact thin film of MgO as a passivation layer. The latter has been shown to reduce the loss resulting from the recombination of electrons injected to SnO_2 with acceptors in the electrolyte.[246,247,248,249] Furthermore, in order to reduce the charge carrier recombination rate, which is partly due to the charge hopping transport mechanism in classical nanoparticle films, quasi one-dimensional nanostructures with direct pathways have been employed to improve the charge collection efficiency.[250] However, those structures generally have a lower surface area, which results in lower dye loading efficiency. Therefore, many hierarchical nanostructures have been introduced instead, in order to increase the surface area, which should improve the charge collection efficiencies and the overall performance of the DSSC.[231,251,252] In the present work, we employ the pulsed laser deposition

[§§§§§] This section is made from one of my publications: Abd-Ellah, M.; Bazargan, S.; Thomas, J. P.; Rahman, M. A.; Sirvastava, S.; Wang, X.; Heinig, N. F.; Leung, K. T. Hierarchical Tin Oxide Nanostructures for Dye-Sensitized Solar Cell Application. *Adv. Electron. Mater.* 2015. Copyright (2015) by Wiley.

(PLD) technique to produce novel SnO_2 hierarchical nanostructures by introducing NiO to create new nucleation sites. This process induces the growth of nanobelt side branches off the nanobelt main trunk to produce a highly branched structure with a much higher surface area. In addition, we achieve further tuning of the open circuit voltage (V_{OC}) by simple surface passivation treatment of these hierarchical SnO_2 nanostructures with uniform coating of an MgO layer, with thickness appropriately optimized. A 10-fold enhancement in the PCE of the hierarchical SnO_2 nanostructured sample with MgO passivation (to 4.14%) relative to that of a pristine SnO_2 nanobelt sample is observed.

6.1 Materials and Methods

SnO_2 nanostructures were prepared in a PLD system with an excimer laser source (248 nm) operating with a fluence of 350 mJ/pulse and a repetition rate of 10 Hz. A detailed description of our catalyst-assisted PLD system used for depositing SnO_2 nanobelts has been given elsewhere.[253] Indium tin oxide (ITO) coated glass substrates were sonicated in acetone and then in isopropanol, each for 10 min, followed by thoroughly rinsing with Millipore water before use. Following our earlier work, [31] gold nanoislands were created on these substrates by post-annealing a thin (<10 nm), sputter-coated layer of gold for 1 h.

Deposition targets, composed of pure SnO_2 and of SnO_2 mixed with 5 wt% NiO, were prepared by mixing and grinding appropriate amounts of respective powders in a mortar and pestle for 20 min, followed by pressing the powders under 20 MPa and sintering them for 24 h at 900 °C. Laser ablation was then performed at a substrate temperature of 500 °C in 400 mTorr of Ar for 90 min, using the respective targets of pristine SnO_2 and of NiO-mixed SnO_2 (designated here as NiO-SnO_2). The morphologies of the resulting SnO_2 nanostructured films were studied by using field-emission scanning electron microscopy (SEM) in a Zeiss Ultra Plus microscope. The crystal structures were characterized by glancing incidence X-ray diffraction (GIXRD) using a PANalytical X'Pert Pro MRD diffractometer, configured with a mirror incident beam optics and 0.27° parallel plate collimator on the diffracted beam optics, at an incidence angle of 0.6°. Bright-field low-resolution and high-resolution transmission electron microscopy (TEM) studies were performed by using a Zeiss Libra 200 MC microscope on hierarchical nanostructures scraped off from the substrate and transferred onto a lacey carbon TEM grid.

The surface areas of the samples were estimated by desorption experiments. Commercial dye solutions (Z907, Solarnix) with different concentrations were prepared and their UV-Vis absorption

spectra were collected. Using the Beer-Lambert law, we constructed a calibration curve based on the absorbance of different dye concentrations at different wavelengths (λ). We also calculated the molar absorption coefficient of the dye to be 4.205 m^2/mol at a fixed λ_{max} = 542 nm. Both dye-loaded pristine SnO_2 and NiO-SnO_2 samples were each placed into a 10 mM solution of KOH (pH 13) to desorb the dye. The concentrations of the desorbed dye were determined by UV-vis spectroscopy and the amount of dye loading was calculated. [170] The as-prepared nanostructures was passivated by further surface treatment of dipping in a hot ethanolic $Mg(CH_3COO)_2$ solution of three different concentrations (20, 60, and 120 mM) for one minute at 70 °C. A passivated shell layer of MgO covering the nanostructures (with thickness depending on the $Mg(CH_3COO)_2$ concentration) was then generated by annealing in air at 500 °C for 90 min.[248]

In the present work, we prepared a DSSC using a standard procedure as follows. The photoanode was obtained by soaking the as-prepared SnO_2 or NiO-SnO_2 nanostructures (supported on an ITO-glass substrate) in a 0.3 mM solution of the Z907 dye for 72 h. A Pt thin film (200 nm thick) sputter-deposited on the ITO-glass substrate was used as the counter electrode. A redox couple electrolyte (I^-/I_3^-) was then sandwiched between the photoanode and the counter electrode. The corresponding electrical parameters were characterized by using a solar cell current-voltage characterization system (PV Measurements IV5) equipped with a class ABA solar simulator and an Air Mass 1.5 global spectral filter. Prior to the current-voltage measurement, the system was calibrated using a Si reference cell (PVM782 with a BK7 window).

6.2 Results and Discussion

6.2.1 Growth mechanism of hierarchical SnO_2 nanostructures

The SEM images in Figure 6.1 show the different morphologies of pristine SnO_2 nanobelts PLD-grown by using a SnO_2 target, highly branched hierarchical nanostructures grown by using a NiO-SnO_2 target, without and with passivation by MgO (the latter is denoted as MgO/NiO-SnO_2). The pristine SnO_2 tapered nanobelts, with typical lengths of 30-70 μm and widths of 5-30 nm, as grown on an ITO substrate pre-decorated with Au nanoislands are found to be in random orientation (Figure 6.1a). A sharp tip with a gold nanoparticle at the top of a nanobelt is observed. Interestingly, the structure changes completely into a hierarchical nanostructure (Figure 6.1b, 6.1d) when using a NiO-mixed SnO_2 target. The resulting side branches are 50-100 nm long, with an Au nanoparticle at the top of each of the tapered nanobelts. The roughened surface of the main nanobelt trunk and the

addition of the side branches found for the NiO-SnO_2 nanostructure (Figure 6.1d) are clearly quite different from the pristine SnO_2 nanobelt sample (Figure 6.1a). We do not observe any further branching of the nanobelt side branches. The absence of any further branching confirms the important role of NiO, since the side branches need to achieve a certain diameter in order for the concentration of surface NiO to sufficiently impact the gold mobility as discussed in detail below.

These NiO-SnO_2 hierarchical nanostructures have considerably larger surface area than the pristine SnO_2 nanobelts, and therefore they are an excellent candidate for use as a photoanode for DSSC application. To further improve performance, we perform MgO passivation of these highly branched Ni-SnO_2 nanostructures, which results in a fine uniform coating of a thin MgO layer (Figure 6.1c, 6.1e) with much smoother surface. Evidently, the ultra-small features are found to be preserved after the surface treatment, which suggests the viability of fabricating hybrid devices based on these hierarchical nanostructures by using this process.

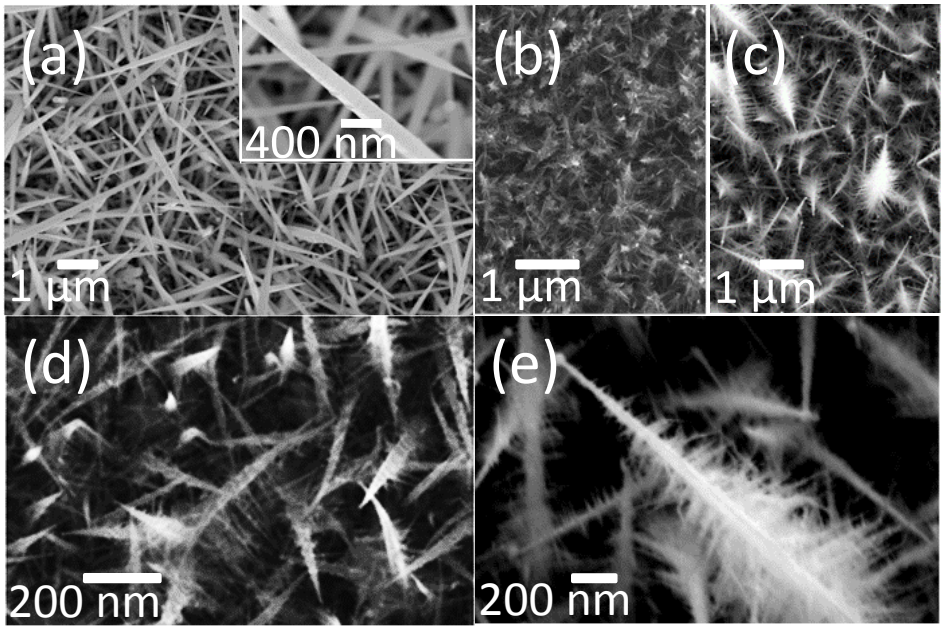

Figure 6.1 SEM images of (a) pristine SnO_2 nanobelts with inset at a higher magnification, (b, d) NiO-SnO_2 hierarchical nanostructures, and (c, e) MgO/NiO-SnO_2 hierarchical nanostructures (with a MgO passivation layer of an optimized thickness). All the nanostructures were PLD-grown on ITO-glass substrates pre-decorated with gold nanoislands at 500 °C in 400 mTorr of Ar for 90 min.

The corresponding GIXRD results (Figure 6.2) show very similar results for the PLD-grown SnO_2 nanobelts and NiO-SnO_2 hierarchical nanostructures, both with a preferred growth direction of (110), while the hierarchical nanostructures are found to have a higher (100) intensity for the $Au_{17}Sn_3$ alloy feature. Furthermore, no shift in the X-ray peak position from the literature values for SnO_2 (00-041-1445) is observed, with the full width half maximum also showing little or no broadening, consistent with a pure material. This finding confirms the absence of any doping effect of NiO on the SnO_2 crystal structure due to their low solubility, in accord with the results of Castro et al. [254] Lowering the NiO concentration in the NiO-SnO_2 target has led to larger and longer primary SnO_2 nanobelts before the formation of side branches, while increasing the NiO concentration has given rise to smaller primary SnO_2 nanobelts and potentially more side branches.

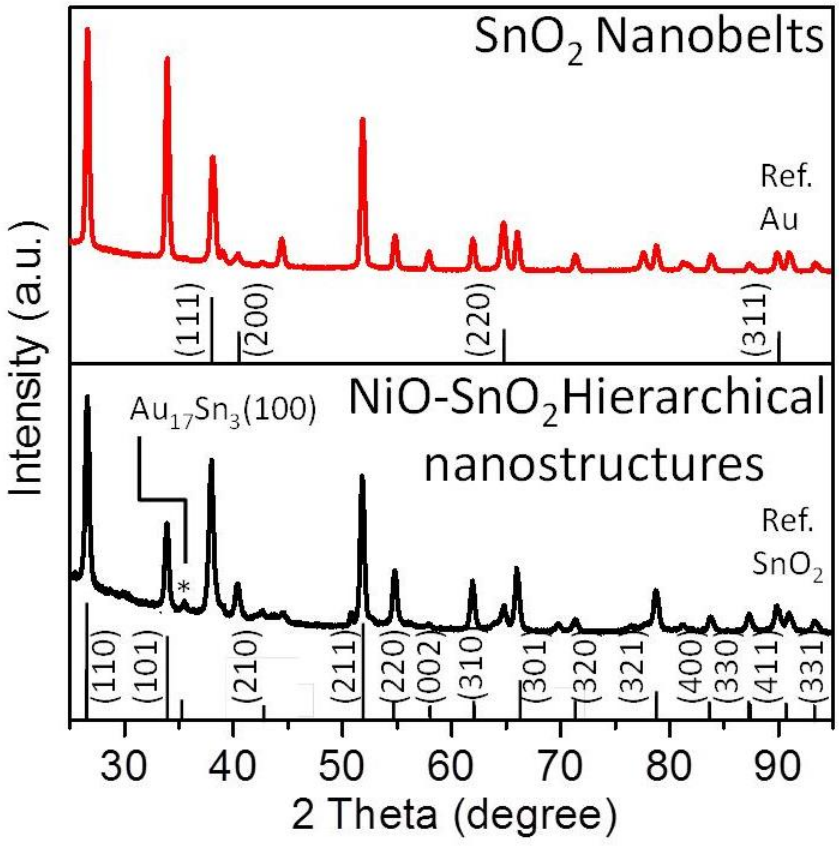

Figure 6.2 Typical glancing-incidence X-ray diffraction patterns of pristine SnO_2 nanobelts and of NiO-SnO_2 hierarchical nanostructures. The PDF2 reference patterns of the tetragonal phase of SnO_2 powder (#00-041-1445) and FCC phase of Au (#00-004-0784) are shown as bottom and top bar graphs, respectively. Asterisk is used to denote a $Au_{17}Sn_3$ alloy feature (#03-065-6388).

The crystal structures of the as-grown hierarchical nanostructures have also been examined by TEM. The low-resolution TEM image (Figure 6.3a) shows a typical PLD-grown NiO-SnO_2 hierarchical nanostructure in which the tapered nanobelts are capped with gold nanoparticles. The corresponding high-resolution TEM images for the nanoparticle (Figure 6.3b) and side branch regions (Figure 6.3c) reveal respective fringe spacings of 0.23 nm and 0.33 nm, which correspond to the interplanar spacings along the Au[111] (Figure 6.3b) and SnO_2[110] directions (Figure 6.3c), respectively. Fourier transform patterns (Figure 6.3, far right panels) are also obtained for the catalyst region (Region 1), outer region of the catalyst (Region 2), and the nanobelt region (Region 3). These patterns are found to be consistent with the identification of the respective regions to Au, metallic Sn, and SnO_2, respectively. The existence of a gold-tin alloy was observed in our earlier work[253] and our results are in accord with previous studies on the catalytic role of metallic Sn nanoparticles in the growth of other semiconductors, [255,256] and the self-catalytic property for the growth of SnO_2 nanowires and nanobelts. [257,258]

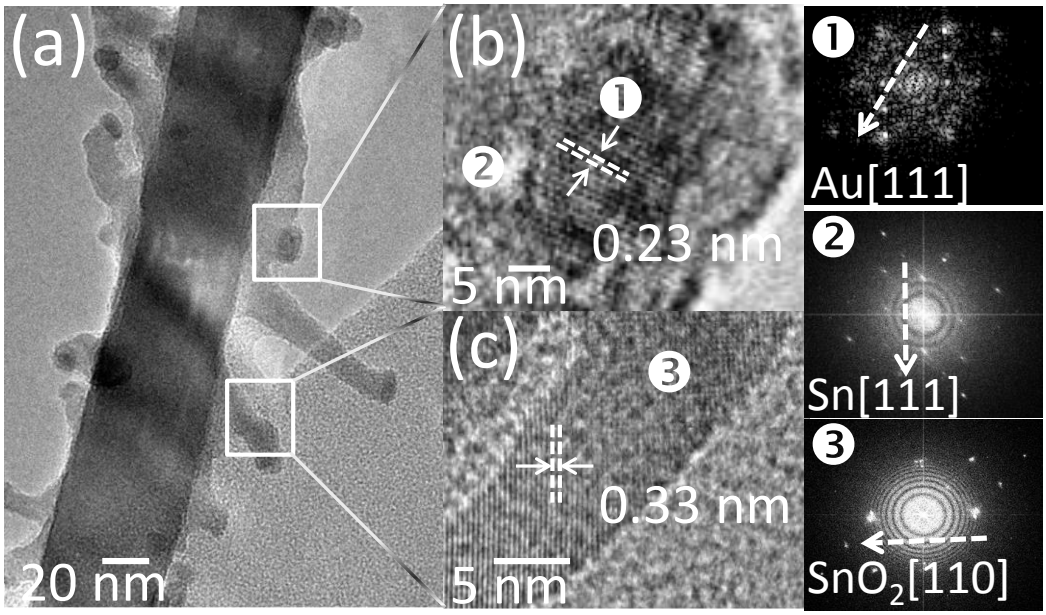

Figure 6.3 (a) Low-resolution and (b, c) high-resolution TEM images for a typical NiO-SnO_2 hierarchical nanostructure with fringe spacings corresponding to different crystalline planes for region 1: gold nanoparticles, region 2: metallic Sn, and region 3: SnO_2 side branch, with different respective growth orientations. Respective Fourier transform patterns for selected regions 1, 2 and 3 are shown on the far right.

In Figure 6.4, we show a schematic diagram of our proposed mechanism for the growth of these hierarchical structures. In our model, Au nanoisland formation on an ITO-glass substrate (Stage a) provides the catalysts for PLD-growth of SnO_2 nanobelts following the vapour-liquid-solid growth mechanism (Stage b). This process is catalyzed with the gold nanoparticle at the top of the nanobelt. As soon as there is a sufficiently large SnO_2 nanobelt surface, the NiO nanoclusters are adsorbed on the surface due to the low solubility of NiO in SnO_2.[254] These NiO nanoclusters on the SnO_2 nanobelt surface would lower the mobility of gold catalysts on the surface, which are relatively mobile at deposition temperature of 500°C. The lower mobility of gold catalysts leads to the formation of smaller gold nanoparticles on the edges of the nanobelt (Stage c). These NiO+Au nanoclusters could serve as possible reaction sites that promote the reduction of Sn^{2+}/Sn^{4+} to metallic Sn on the nanobelt edge (Stage d). The Sn atoms interacting with the mobile gold atoms form the Sn-Au alloy nucleation sites that catalyse growth of SnO_2 side branches off the trunk of the nanobelt, following the vapour-liquid-solid growth mechanism (Stage e) with higher magnification of the gold particles surrounded with metallic Sn shell as will be confirmed later. This process is self-limited by the finite amount of NiO (5%) present in the target, creating the hierarchical nanostructures without any secondary side branch generation. Consistent with our XRD results, no doping effect of NiO is detected as shown in Figure 6.3c, as no change in the SnO_2 lattice spacing is observed. Growth of the hierarchical structures should depend sensitively on the NiO concentration in the SnO_2 target, because a critical surface concentration of NiO is required to lower the gold mobility. The effect of NiO can be inferred by the presence of a thin layer of metallic Sn coating the gold nanoparticles located at the tips of the side branches and of the main trunks of SnO_2 nanobelts. The presence of the metallic Sn coating is supported by the Fourier transform patterns of region 2 in Figure 6.3.

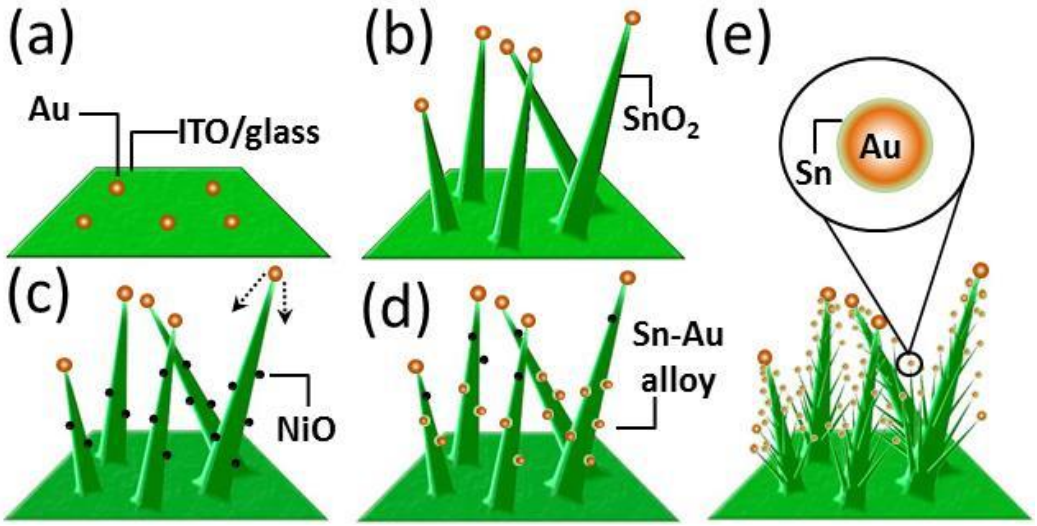

Figure 6.4 Schematic diagram of our proposed growth mechanism for a typical NiO-SnO_2 hierarchical nanostructure grown by catalyst-assisted PLD using a SnO_2 target mixed with NiO.

6.2.2 SnO_2 nanostructures as photoanodes for DSSC application

The increase in the surface area of the NiO-SnO_2 hierarchical nanostructures can be estimated by measuring the enhancement of dye absorption. Prior to our dye loading measurements, a calibration curve of the Z907 dye at different concentrations at constant maximum wavelength = 542 nm was constructed as shown in Figure 6.5. The UV-Vis absorption spectra were collected after incubating both the pristine SnO_2 nanobelts and hierarchical NiO-SnO_2 nanostructures in the dye overnight. This was followed by desorption of the absorbed dye from the nanostructures using 10 mM KOH at pH 13 and evaluation of the concentrations of the desorbed dye for both samples from their UV-Vis spectra. Figure 6.6a shows a higher dye absorbance for the NiO-SnO_2 hierarchical nanostructures giving a dye concentration of 8.6×10^{-3} mM, in comparison to that of pristine SnO_2 nanobelts with a concentration of 7.7×10^{-3} mM, all evaluated at wavelength of 542 nm. This result confirms the larger surface area of the as-prepared NiO-SnO_2 hierarchical nanostructures. In Figure 6.6b, we show the schematic diagrams of the DSSCs that we fabricated using the pristine SnO_2 nanobelts and NiO-SnO_2 hierarchical nanostructures as the photoanodes. The increase in the absorption areas provided by NiO-SnO_2 hierarchical nanostructures results in greater absorption of the dye, which in turn increases the solar cell performance, as discussed below.

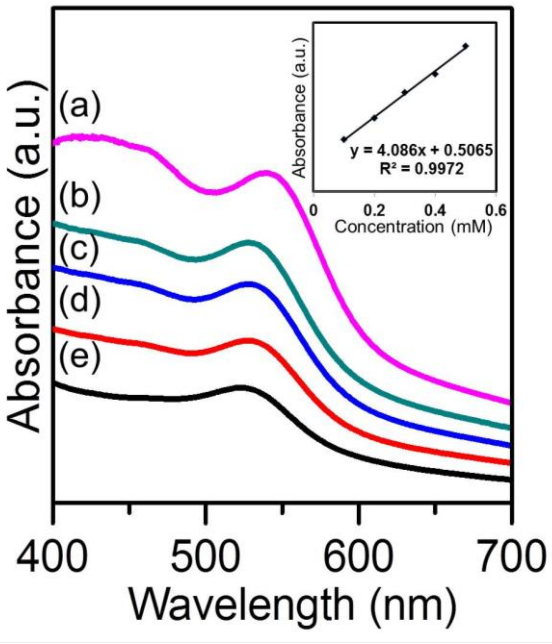

Figure 6.5 UV/Vis absorption spectra of dye solutions with different concentrations: (a) 0.5, (b) 0.4, (c) 0.3, (d) 0.2, and (e) 0.1 mM. The absorbance at constant wavelength = 542 nm as a function of the dye concentration is shown as the inset.

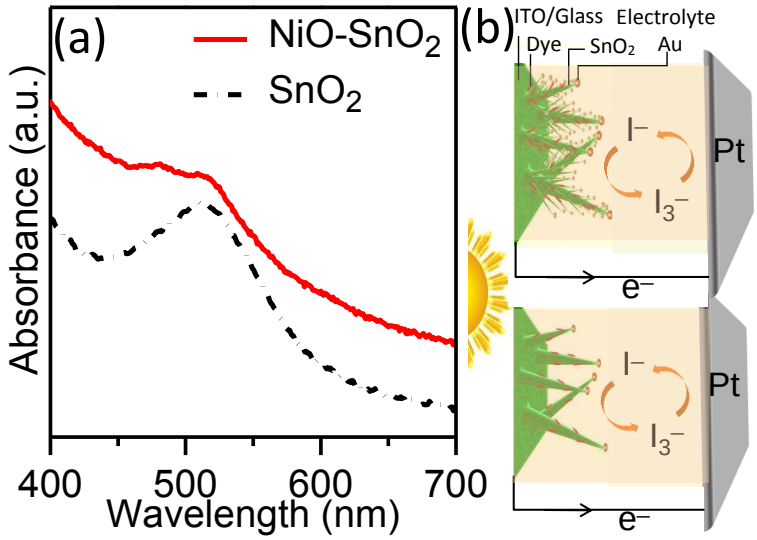

Figure 6.6 (a) UV/Vis absorption spectra for pristine SnO_2 nanobelts and NiO-SnO_2 nanostructures, depicting a higher dye loading for the NiO-SnO_2 hierarchical nanostructures than the pristine SnO_2 nanobelts due to the increase in surface area. (b) Schematic diagrams of DSSC device structures employing pristine SnO_2 nanobelts (top) and NiO-SnO_2 hierarchical nanostructures (bottom) as the photoanode materials.

Figure 6.7a shows the current density vs voltage curves obtained over an active area of 0.1 cm^2 for different DSSCs employing as active photoanode materials: pristine SnO_2 (Cell A), hierarchical NiO-SnO_2 (Cell B), and hierarchical NiO-SnO_2 nanostructures passivated with an MgO layer, designated as MgO/NiO-SnO_2 (Cell C). For Cell C, we varied the thickness of the MgO passivation layer by incubating the sample in different concentrations of hot ethanolic $Mg(CH_3COO)_2$: (C20) 20 mM, (C60) 60 mM, and (C120) 120 mM, all followed by annealing in air at 500°C for 90 min. Their solar cell performances, along with their cell structure, are summarized in Figure 6.7 and Table 6.1. Although great enhancement by nearly an order of magnitude is observed in the short circuit current density (J_{SC} = 18.57 mA/cm^2) for Cell B due to a higher dye loading arising from a larger surface area of the hierarchical NiO-SnO_2 nanostructures, both open circuit voltage (V_{OC} = 0.414 V) and fill factor (FF = 48 %) for Cell B are slightly lower than the respective values for Cell A (with V_{OC} = 0.463 V, FF = 55 % , and J_{SC} = 1.87 mA/cm^2). This finding confirms a more pronounced effect that the higher mobility in SnO_2 leads to a higher probability of recombination of electrons injected to SnO_2 with acceptors in the electrolyte.[246]

In order to reduce the recombination process loss, we coated an insulating layer of MgO with different thickness using hot ethanolic $Mg(CH_3COO)_2$ solutions of different concentrations, as shown in the schematic band diagram of the constructed cell in Figure 6.8. For a thicker MgO film coating obtained with a higher concentration for Cell C120, up to 0.3 V improvement in V_{OC} to 0.710 V and 15.9 % increase in FF to 71 % with respect to Cell B are obtained. However, this is accompanied by a drastically lower J_{SC} of 1.83 mA/cm^2, indicating sharp retardation in charge carrier diffusion likely caused by a thicker passivation layer. Further investigation was conducted to optimize the passivation layer thickness by studying the effect of different concentrations of $Mg(CH_3COO)_2$ on both J_{SC} and V_{OC}, as well as the overall PCE, as shown in Figure 6.7.

Evidently, an increase of 0.138 V in V_{OC} for C20, followed by higher values of 0.188 V for C60 and 0.296 V for C120, all with respect to V_{OC} for Cell B, is observed (Figure 6.7b). At the same time, sharp increase in J_{SC} is found for Cell B (compared with Cell A), followed by a generally reducing trend from B to C20, C60 and C120 (Figure 6.7c). An optimum concentration of 20 mM was obtained for Cell C20, with J_{SC}, V_{OC}, and FF of 13.34 mA/cm^2, 0.547 V, and 52 %, respectively, leading to a notable increase in PCE (to 4.14%) from the PCEs of Cell A (0.48%) and Cell B (3.69%) (Figure 6.7d). However, this increase in PCE is at the expense of a smaller J_{SC}, which can be explained by the blue shift in the photocurrent of insulating coating.[259] Recent studies have employed

SnO_2 films and nanostructures, mostly prepared by hydrothermal methods, as the photoanode material for DSSC applications, the PCE of which was found to increase by up to 7% after passivation process. [248, 249, 250, 259, 244] To date, even fewer studies have used SnO_2 nanomaterials grown by vapor deposition methods for DSSCs applications. Gubbala et al. employed ALD-grown SnO_2 nanowires as a photoanode with an excellent open circuit voltage of 0.560 V and an overall PCE of 2.1%. Furthermore, an enhancement in their performance of 4.1% was obtained by coating the highly interconnected nanowires with TiO_2 nanoparticles.[247]

In the present work, a remarkable enhancement in PCE, i.e. over 7 times increase, for Cell B is observed when compared with pristine SnO_2 nanobelts (Cell A). While fine tuning of the thickness of the MgO passivation layer appears to improve the PCE by only 12% for Cell C20 from that without any passivation layer (Cell B), the improvement in V_{OC} by 33% for Cell C20 (and 71% for Cell 120) with respect to that for Cell B is significant. Future work will focus on further optimization of the deposition parameters to obtain better length to width aspect ratio for the as-grown SnO_2 nanostructure for electronic applications. In addition, in-situ decoration with Au or Ag nanoclusters in the hierarchical SnO_2 nanostructures during PLD growth may offer additional improvement on their PCEs through plasmonic effects.

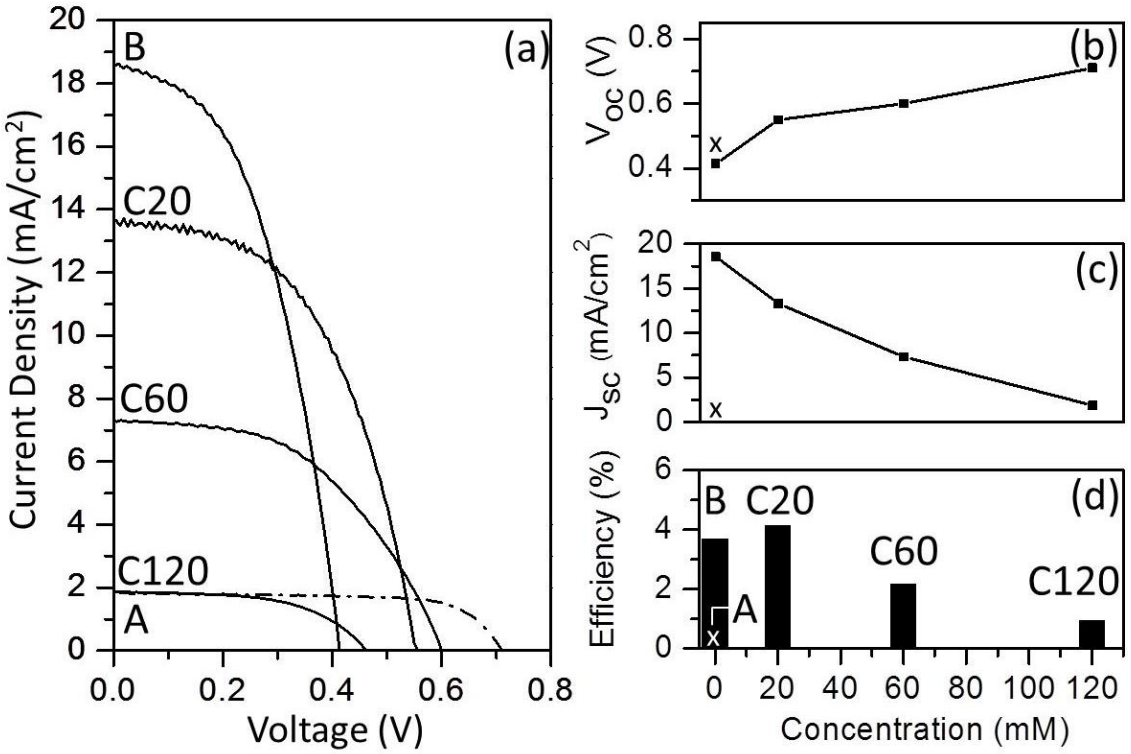

Figure 6.7 (a) Current density vs voltage profiles, (b) open circuit voltage, (c) short circuit current density, and (d) photoconversion efficiency of DSSCs with different photoanode materials: (Cell A) pristine SnO_2 nanobelts (marked by cross), (Cell B) NiO-SnO_2 hierarchical nanostructures, and (Cell C20, C60, C120) NiO-SnO_2 hierarchical nanostructures passivated with MgO layers of different thicknesses.

Table 6.1 Solar cell performance of DSSCs with different photoanode materials: (Cell A) pristine SnO_2 nanobelts, (Cell B) NiO-SnO_2 hierarchical nanostructures, and (Cell C20, C60, C120) MgO/NiO-SnO_2 hierarchical nanostructures passivated with MgO of different thicknesses *

Cell Structure			V_{OC} (V)	J_{SC} (mA/cm²)	FF [%]	PCE [%]
A		SnO_2	0.463	1.87	55	0.48
B		NiO-SnO_2	0.414	18.57	48	3.69
C	C20	MgO/NiO-SnO_2	0.552	13.34	52	4.14
	C60	MgO/NiO-SnO_2	0.602	7.30	49	2.17
	C120	MgO/NiO-SnO_2	0.710	1.83	71	0.93

*Cells C20, C60 and C120 were prepared with MgO passivation layers of different thicknesses obtained by soaking in, respectively, 20, 60, and 120 mM of hot ethanolic Mg acetate solution at 70 °C for 1 min, followed by annealing in air at 500 °C for 90 min.

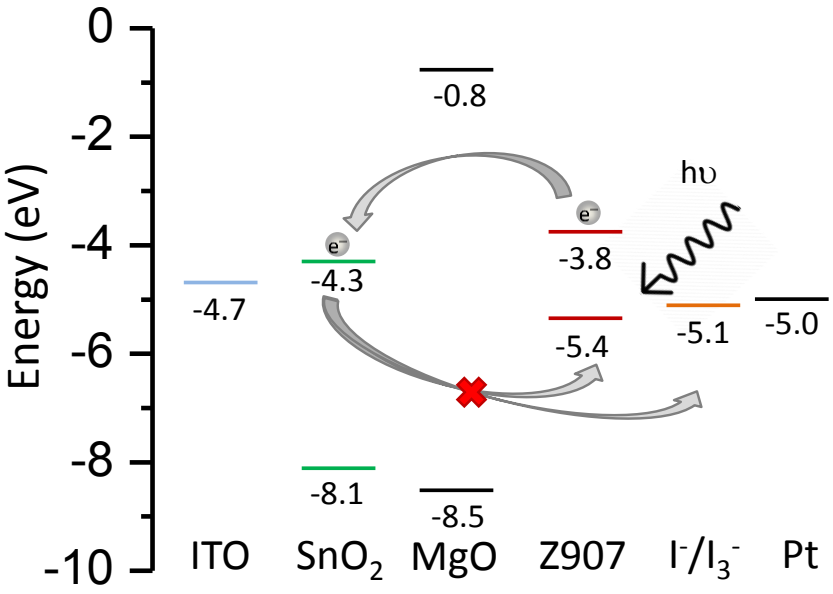

Figure 6.8 Schematic diagram of MgO-coated SnO_2 nanostructures in a typical DSSC system, depicting that the presence of MgO as the passivation layer could prevent the undesirable charge recombination with any oxidized dye or electrolyte species.

6.3 Conclusion

Highly branched NiO-SnO_2 hierarchical nanostructures, consisting of tapered nanobelt main trunk and nanobelt side branches with greatly increased surface area, were obtained by using a NiO-mixed SnO_2 target for catalyst-assisted PLD. We propose a plausible growth model involving NiO nanoclusters as the initiators for reducing Sn ions to metallic Sn, which then mixes with the highly mobile Au atoms (coming from the Au nanocatalyst at the tip of the nanobelt) forming Sn-Au alloy nanoclusters on the nanobelt surface. These Sn-Au alloy nanoclusters provide the nucleation sites for growth of SnO_2 side branches. Furthermore, both pristine SnO_2 nanobelts and NiO-SnO_2 hierarchical nanostructures were employed as photoanode materials in DSSCs. When compared to SnO_2 pristine nanobelts (Cell A), an excellent enhancement in J_{SC} is observed for NiO-SnO_2 hierarchical nanostructures (Cell B) due to their higher dye loading as a result of their larger surface area and better charge collection property. Furthermore, hot ethanolic $Mg(CH_3COO)_2$ solutions of different concentrations have been used to optimize coating of the as-prepared NiO-SnO_2 hierarchical nanostructures with a MgO passivation layer of appropriate thickness. This passivation step is found to be successful in reducing the large contribution of recombination of electrons injected to SnO_2 with

acceptors in the electrolyte due to the much higher electron transport dynamics of SnO_2 photoanode. With an optimized thickness for the MgO passivation layer to reduce the expected recombination loss, a nearly 10-fold enhancement in the PCE to 4.14% has been achieved for MgO-passivated NiO-SnO_2 hierarchical nanostructures (Cell C20) when compared to pristine SnO_2 nanobelts (Cell A). The present work therefore illustrates the importance of increasing surface area and enhancing the charge carrier collection by developing a new approach of synthesizing hierarchical nanostructures. In addition, we succeeded in improving the open circuit voltage by minimizing recombination loss using MgO passivation with appropriately optimized layer thickness for building high efficiency dye-sensitized solar cells.

Chapter 7
Concluding Remarks and Future Work

7.1 Summary of Contributions

In the present work, we have succeeded in constructing different inorganic and organic solar cells by employing ZnO and SnO_2 nanostructures and achieve respectable performance. For the first time, ZnO nanotubes have been synthesized on ITO-glass substrates using a one-step, catalyst- and seed-layer-free direct electrodeposition method without O_2 bubbling or any etching step. This method creates one-dimensional tubular nanostructure with high surface area and less surface defects. We demonstrate the importance of controlling the electrolyte conductivity rather than the traditional method of using different electrolyte concentration to manipulate the morphologies of the prepared ZnO nanostructures. Two different ZnO nanostructures (i.e. nanotubes vs nanorods) can be prepared by varying the supporting electrolyte with different monovalent and divalent anions, respectively. We propose a growth mechanism for ZnO nanotubes (ZnO-NTs) and ZnO nanorods (ZnO-NRs), based on complete characterization of their morphologies, crystal structures and chemical-state compositions.

Briefly, the equivalent conductance values for all supporting electrolytes with monovalent anions: Cl^- (62.8 S cm^2 mol^{-1}), ClO_4^- (59.1 S cm^2 mol^{-1}), and NO_3^- (59.2 S cm^2 mol^{-1}) are considerably lower than that of supporting electrolytes with divalent anions: SO_4^{2-} (207.6 S cm^2 mol^{-1}) and $C_2O_4^{2-}$ (207.4 S cm^2 mol^{-1}). This difference affects the ion diffusion process during electrodeposition of ZnO nanostructures and their growth mechanism. A highly conducting electrolyte is expected to enhance the diffusion of Zn^{2+}, which therefore leads to higher $Zn(OH)_2$ generation and subsequently higher ZnO deposition that results in ZnO nanorod formation. However, under a lower conductivity condition, the Cl^- adsorption rate (as in the monovalent anion case) is more pronounced, which would result in a lower ZnO growth rate and then the pseudo two-dimensional nanotube formation would occur. Different parameters such as deposition temperature and deposition time have also been investigated in order to control the areal density of the electrodeposited ZnO nanotubes. As an exploratory investigation for their application in photovoltaics, we shed some light on employing these ZnO nanotubes as an active photoanode material in DSSCs that offer a decent efficiency of 1.6%.

These n-type one-dimensional ZnO nanostructures allow us to construct a p-n heterojunction inorganic solar cell by incorporating p-type Cu_2O thin film. This approach is used to improve the light harvesting and the charge collection efficiency by taking advantage of the high surface area junction and direct charge transfer pathway of these one-dimensional ZnO nanostructures. Most of the previous studies on electrodeposited p-Cu_2O/n-ZnO heterojunction solar cells have involved electrodeposited ZnO nanorods/nanowires and ZnO nanotubes, the latter obtained after a second etching step of the as-prepared ZnO nanorods in order to obtain complete dissolution of the (0001) plane and formation of the tubular structure. However, etching in such a highly alkaline solution would create a significant amount of surface defects and consequently further increase the recombination loss at the junction interface. This has become a limiting factor for the reported open-circuit voltage value and consequently the overall performance. In contrast, we construct our heterojunction solar cells consisted of directly electrodeposited n-type ZnO nanotubes (and nanorods) with less surface defects and a p-type Cu_2O thin film of appropriate thickness to maximize their open-circuit voltages.

Post-annealing of the p-type Cu_2O nanostructured film at 200°C is found to provide better crystallinity and a higher conductivity for additional improvement in the performance. Further optimizing the film thickness of Cu_2O, as calculated using Poisson's equation according to their charge carrier concentration and absolute permittivity values, also assures the full built-in potential across the junction interface. Finally, the electrodeposited tubular ZnO nanostructures is grown on the top of a sufficiently thick ZnO seed layer, which prevents any leakage pathway and increases the junction area, and consequently increases their short-circuit current values. The open-circuit values obtained for Cu_2O/ZnO-NT (0.71 V) and Cu_2O/ZnO-NR heterojunction devices (0.66 V) represent the highest V_{OC} reported to date for this type of electrodeposited Cu_2O/ZnO solar cells. Remarkably, the short-circuit current density of the Cu_2O/ZnO-NT cell (2.40 mA/cm^2) is twice that of the Cu_2O/ZnO-NR cell (1.12 mA/cm^2), which validates the advantages of larger junction area and better charge carrier collection as provided by junction devices based on tubular nanostructures.

As an alternative to TiO_2 photoanode, ZnO and SnO_2 nanostructures are used as photoanodes in classical dye sensitized solar cells (DSSCs) in order to take advantage of their excellent electron dynamics, particularly their higher electron mobility and electron diffusion coefficients when compared to the commonly used TiO_2. The electrodeposited pristine ZnO nanotubes exhibit an efficiency approaching 4.7% when loaded with the N719 dye in a typical liquid based DSSC. Simple

modification by electrodepositing gold nanoparticles (GNPs) on the surfaces of ZnO nanotubes produces a higher-performance photoanode (GNP/ZnO-NT) with higher absorbance in the visible region due to the surface plasmon resonance of the metallic gold nanoparticles. The size distribution and the areal density of the electrodeposited gold nanoparticles are optimized by employing the appropriate $AuCl_3$ solution concentration and deposition time. An optimized deposition time of 300 s in a 1 mM $AuCl_3$ electrolyte solution is found to produce a homogenous coverage of GNPs with an average particle size of 12 nm and the largest areal density, which leads to the highest light absorbance for GNP/ZnO-NT. Using cyclic voltammetry and electrochemical impedance spectroscopy, we further illustrate the enhanced charger transfer property as provided by the smaller charge transfer resistance for GNP/ZnO-NT compared to the pristine ZnO-NT photoanode.

The GNP/ZnO-NT and ZnO-NT photoanodes are used to construct classical liquid-based DSSCs with and without dye loading to investigate their solar cell performance. Our findings confirm the higher photon absorbance of GNP/ZnO-NT compared to pristine ZnO-NT photoanode due to the enhancement by the plasmonic gold nanoparticles. The latter is responsible for electron injection from the Au Fermi level into the ZnO conduction band, which subsequently produces photocurrent even in the absence of the dye molecules. In the presence of the dye, electron injection into the ZnO conduction band could occur in two routes. The electrons can be generated from the photo-excited dye molecules as expected in a typical DSSC process mechanism or transferred indirectly to the deposited GNPs first and then onto the ZnO NT surface. Furthermore, electron accumulation at the Au energy level could shift the Au Fermi level upward near the ZnO conduction band and hence lead to build up of a potential barrier in the metal/semiconductor photodiode. The formation of such a Schottky barrier at the Au/ZnO interface would improve the device performance due to the blockage of the back electron-transfer from the ZnO conduction band to the GNPs. These enhancements in the GNP/ZnO-NT photoanode have led to an excellent efficiency of 6%.

In addition, we employ the hierarchical SnO_2 nanostructures, prepared by using catalyst-assisted pulsed laser deposition, as the photoanode for DSSC application. A novel growth mechanism is proposed for such highly branched one-dimensional nanostructures obtained by mixing NiO into the SnO_2 target. In particular, the growth of the primary SnO_2 nanobelts is catalyzed by gold nanoislands prepared on ITO glass substrate. The catalyzed PLD-growth of SnO_2 follows the vapour-liquid-solid growth mechanism, where the gold nanoparticles are lifted up on the top of SnO_2 nanobelts. NiO nanoclusters would adsorb on the nanobelt surface as soon as they are formed,

because of the low solubility of NiO in SnO_2. Consequently, the adsorbed NiO nanoclusters could first reduce the mobility of the gold catalysts on the surface, which are relatively mobile at the deposition temperature of 500°C. Known for their reducing property, the Au catalysts could also convert Sn^{2+}/Sn^{4+} to metallic Sn to form Sn-Au alloy nucleation sites. These Sn-Au alloy sites catalyze the growth of secondary side branches of SnO_2 that consequently leads to the formation of the observed highly branched hierarchical NiO-SnO_2 nanostructures.

Taking the advantage of their high specific surface area and consequently their enhanced dye loading property, we employ these hierarchical NiO-SnO_2 nanostructures as photoanode material for DSSC application. With their enhanced UV/Vis absorbance compared to pristine SnO_2 nanobelts, we obtain an efficiency of 3.69% for the NiO-SnO_2 based DSSC, which is nearly an order of magnitude that of pristine SnO_2 nanobelts (0.48%). However, their open-circuit voltage (0.41 V) is somewhat limited, which is due to the recombination loss that occurs when electrons are injected to SnO_2 with acceptors in the electrolyte. To further improve the DSSC performance, we coat the as-prepared hierarchical NiO-SnO_2 nanostructures with an MgO passivation layer of appropriately optimized thickness in order to reduce the undesirable recombination loss. This leads to an improved V_{OC} of 0.14 V and a respectable overall efficiency of 4.14%.

7.2 Future Work

In the present work, we utilize the as-prepared one-dimensional ZnO and SnO_2 nanostructures as advanced photoanode materials for constructing various inorganic and organic solar cell systems. Further work could be pursued to further improve the performance of the constructed solar cells. Several lines of research are summarized below:

- **Photoanode design optimization by nanolithography**

Further control of the dimensionality of the electrodeposited ZnO and as-grown SnO_2 nanostructures including their length, diameter, and length-to-width aspect ratio would allow us to further optimize the performance of the solar cells. Despite their higher cost and more complicated fabrication process, nanolithographical techniques could provide us with the flexibility in "tuning" the spatial, geometrical and orientational arrangements of the as-prepared one-dimensional nanostructures on the substrate. Studies using these optimized templates can provide us with new insights into charge collection and geometrical enhancement in the overall performance of the solar cell before lower-cost, large-scale methods can be developed. As shown in Figure 7.1, some

preliminary work along this direction has been achieved. A matrix of dots of different diameters and pitch spacings is patterned on a photoresist-coated ITO-glass substrate by using the newly installed ion beam lithography system, followed by sputtering with Pt and photoresist removal. These templates are then used as nanoelectrodes for electrodeposition of ZnO nanostructures. Early results demonstrate the potential control of the growth direction of as-grown ZnO nanostructures in well-ordered arrays. Further work is clearly needed to optimize the template diameter to achieve better vertically alignment of as-grown nanostructures in the arrays.

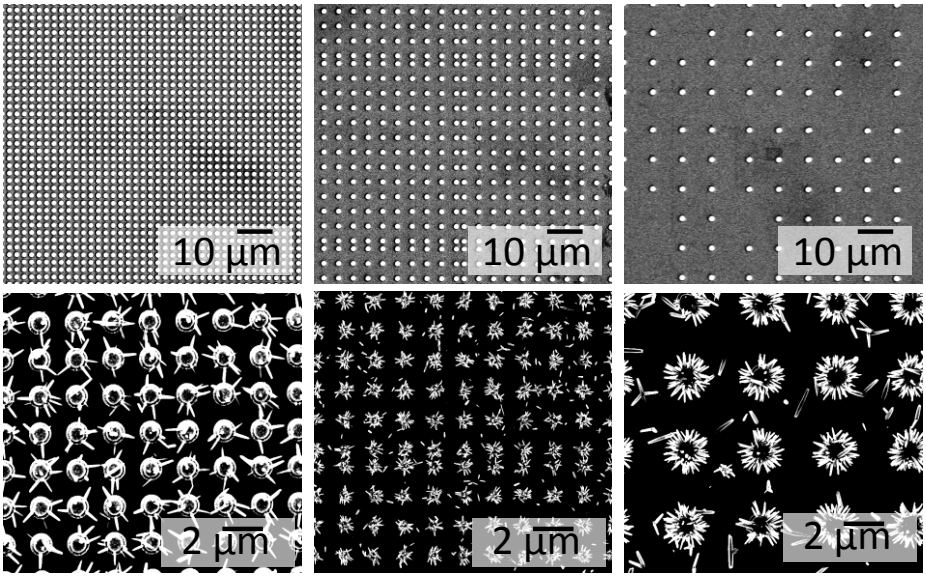

Figure 7.1 SEM images of Pt template on ITO-glass with different pitch spacings before and after electrodeposition of ZnO nanostructures.

- **Dry deposition methods for nanostructure synthesis**

Despite the advantage of the "all-electrodeposition" approach for fabricating photovoltaic devices at ambient temperature, wet-chemistry methods suffer from lower reproducibility and the presence of unwanted chemicals. Simple dry deposition methods such as the reactive ion etching should be explored to reproduce similar nanostructures that are compatible with heterojunction solar cells. Preliminary work has shown that reactive ion etching could easily generate the required one-dimensional nanostructures (nanofingers), and that the interface quality with an acceptable amount of defects could also be achieved.

- **Band structure engineering**

Additional band structure engineering of the constructed cells should be explored. This can be achieved by doping the as-prepared nanostructures with trivalent group-III elements such as Al, Ga, and In, which would substitute the cation in ZnO nanostructures and consequently affect their electronic structure with fine control of tuning their band gap using different doping concentrations. Another approach is to construct core-shell nanostructured materials with different band gaps, in order to maximize the amount of photon absorbed and their light harvesting capability. For example, coating ZnO nanostructures with different semiconductors nanocrystals (quantum dots), including CdS, CdSe, and InAs, could enhance the solar light absorption by finely controlling their particle size. In addition, the ability of quantum dots in generating multiple electron-hole pairs per photon could also improve the device performance.

- **Post treatment, theoretical calculations, and new configuration of DSSCs**

For DSSC systems, synthesis of new hybrid nanostructures designed specifically for photovoltaic applications could lead to better device performance by taking advantage of their synergetic properties that individual constituent components lack. For instance, coating TiO_2 nanoclusters on ZnO nanostructures surface would improve their chemical stability in the acidic media of the dye, which would produce fewer defects and less recombination loss. Additional post-treatments of ultra-violet radiation, ozone, and annealing in different ambient gas environments for the as-prepared photoanodes should be examined, with the goal to enhance the dye/semiconductor interface and their dye-loading properties. New metal-free dyes should also be evaluated especially for ZnO nanostructures due to their higher complexing ability than SnO_2 and TiO_2. Similar to an earlier work done by Barpuzary et al, showing an excellent performance of (5.7%) using hydrothermally grown one-dimensional ZnO nanowire in cooperated with a newly synthesized metal-free, D−π–A type, carbazole dye (SK1) sensitizer-based photovoltaic device.[260] An extensive study of the charge transfer process, the lifetime of the charge carriers, and their diffusion lengths would help to refine the details of the DSSC process mechanism and to minimize the undesirable recombination loss. Exploring other types of solid-state DSSCs, including a solid-state polymer electrolyte or/and DSSC with a hole-conducting (p-type semiconductor) electrolyte, should also be pursued.

- **Other applications**

In addition to the present focus on photovoltaic applications, further work is needed to explore the use of these ZnO and SnO_2 nanostructures for other optoelectronic and sensing applications. Newly emerged solar battery for producing and storing electrical energy without the need of additional traditional batteries has been constructed by using classical TiO_2 based DSSCs. Alternative photoanodes could, however, help to minimize the performance decay due to the observed low thermal stability and dye degradation as reported by Yu et al.[261] By taking the advantage of SnO_2 nanostructured thin-film photoanodes, high thermal and chemical stability with low UV degradation could provide an interesting solution to reducing the efficiency decay problem in solar batteries.

Appendix A

Permissions

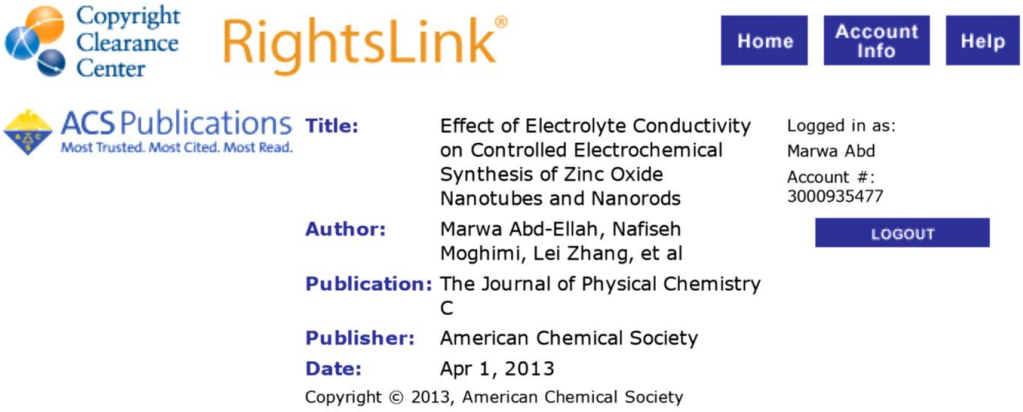

Copyright Clearance Center RightsLink®

Home | Account Info | Help

ACS Publications
Most Trusted. Most Cited. Most Read.

Title: Effect of Electrolyte Conductivity on Controlled Electrochemical Synthesis of Zinc Oxide Nanotubes and Nanorods

Author: Marwa Abd-Ellah, Nafiseh Moghimi, Lei Zhang, et al

Publication: The Journal of Physical Chemistry C

Publisher: American Chemical Society

Date: Apr 1, 2013

Copyright © 2013, American Chemical Society

Logged in as:
Marwa Abd
Account #:
3000935477

LOGOUT

PERMISSION/LICENSE IS GRANTED FOR YOUR ORDER AT NO CHARGE

This type of permission/license, instead of the standard Terms & Conditions, is sent to you because no fee is being charged for your order. Please note the following:

- Permission is granted for your request in both print and electronic formats, and translations.
- If figures and/or tables were requested, they may be adapted or used in part.
- Please print this page for your records and send a copy of it to your publisher/graduate school.
- Appropriate credit for the requested material should be given as follows: "Reprinted (adapted) with permission from (COMPLETE REFERENCE CITATION). Copyright (YEAR) American Chemical Society." Insert appropriate information in place of the capitalized words.
- One-time permission is granted only for the use specified in your request. No additional uses are granted (such as derivative works or other editions). For any other uses, please submit a new request.

BACK | CLOSE WINDOW

JOHN WILEY AND SONS LICENSE TERMS AND CONDITIONS

Jul 15, 2015

This Agreement between Marwa Abd ("You") and John Wiley and Sons ("John Wiley and Sons") consists of your license details and the terms and conditions provided by John Wiley and Sons and Copyright Clearance Center.

License Number	3670370575703
License date	Jul 15, 2015
Licensed Content Publisher	John Wiley and Sons
Licensed Content Publication	Advanced Electronic Materials
Licensed Content Title	Hierarchical Tin Oxide Nanostructures for Dye-Sensitized Solar Cell Application
Licensed Content Author	Marwa Abd-Ellah,Samad Bazargan,Joseph P. Thomas,Md Anisur Rahman,Saurabh Srivastava,Xiongyao Wang,Nina F. Heinig,Kam Tong Leung
Licensed Content Date	Jul 8, 2015
Pages	1
Type of use	Dissertation/Thesis
Requestor type	Author of this Wiley article
Format	Print and electronic
Portion	Full article
Will you be translating?	No
Title of your thesis / dissertation	Hypride transparent conductive oxide for photovoltaic applications
Expected completion date	Dec 2015
Expected size (number of pages)	150
Requestor Location	Marwa Abd-Ellah 604-205 Victoria Street South Kitchener, ON N2G 4Z6 Canada Attn: Marwa Abd-Ellah
Billing Type	Invoice
Billing Address	Marwa Abd-Ellah 604-205 Victoria Street South Kitchener, ON N2G 4Z6 Canada Attn: Marwa Abd-Ellah

Order Completed

Thank you very much for your order.

This is a License Agreement between Marwa Abd-Ellah ("You") and Cambridge University Press ("Cambridge University Press"). The license consists of your order details, the terms and conditions provided by Cambridge University Press, and the payment terms and conditions.

Get the printable license.

License Number	3670890941188
License date	Jul 16, 2015
Licensed content publisher	Cambridge University Press
Licensed content publication	MRS Bulletin
Licensed content title	Criteria for Choosing Transparent Conductors
Licensed content author	Roy G. Gordon
Licensed content date	Jan 31, 2011
Volume number	25
Issue number	08
Start page	52
End page	57
Type of Use	Dissertation/Thesis
Requestor type	Not-for-profit
Portion	Text extract
Number of pages requested	1
Order reference number	None
Territory for reuse	World
Title of your thesis / dissertation	Hybrid Transparent Conductive Oxide Nanostructured Materials for Photovoltaic Applications
Expected completion date	Nov 2015
Estimated size(pages)	150
Billing Type	Invoice
Billing address	Marwa Abd-Ellah 604-205 Victoria Street South Kitchener, ON N2G 4Z6 Canada Attn: Marwa Abd-Ellah
Tax (0.00%)	0.00 USD
Total	0.00 USD

ORDER MORE... CLOSE WINDOW

Order Completed

Thank you very much for your order.

This is a License Agreement between Marwa Abd-Ellah ("You") and Springer ("Springer"). The license consists of your order details, the terms and conditions provided by Springer, and the payment terms and conditions.

Get the printable license.

License Number	3670900227532
License date	Jul 16, 2015
Licensed content publisher	Springer
Licensed content publication	Springer eBook
Licensed content title	Electronic Structure of Transparent Conducting Oxides
Licensed content author	J. Robertson
Licensed content date	Jan 1, 2011
Type of Use	Thesis/Dissertation
Portion	Figures
Author of this Springer article	No
Original figure numbers	Fig. 2.13
Title of your thesis / dissertation	Hybrid Transparent Conductive Oxide Nanostructured Materials for Photovoltaic Applications
Expected completion date	Nov 2015
Estimated size(pages)	150
Total	0.00 CAD

CLOSE WINDOW

Order Completed

Thank you very much for your order.

This is a License Agreement between Marwa Abd-Ellah ("You") and Cambridge University Press ("Cambridge University Press"). The license consists of your order details, the terms and conditions provided by Cambridge University Press, and the payment terms and conditions.

Get the printable license.

License Number	3670900987338
License date	Jul 16, 2015
Licensed content publisher	Cambridge University Press
Licensed content publication	MRS Bulletin
Licensed content title	Transparent Conducting Oxides for Photovoltaics
Licensed content author	Elvira Fortunato, David Ginley, Hideo Hosono and David C. Paine
Licensed content date	Jan 31, 2011
Volume number	32
Issue number	03
Start page	242
End page	247
Type of Use	Dissertation/Thesis
Requestor type	Not-for-profit
Portion	Text extract
Number of pages requested	1
Order reference number	None
Territory for reuse	World
Title of your thesis / dissertation	Hybrid Transparent Conductive Oxide Nanostructured Materials for Photovoltaic Applications
Expected completion date	Nov 2015
Estimated size(pages)	150
Billing Type	Invoice
Billing address	Marwa Abd-Ellah 604-205 Victoria Street South Kitchener, ON N2G 4Z6 Canada Attn: Marwa Abd-Ellah
Tax (0.00%)	0.00 USD
Total	0.00 USD

ORDER MORE... CLOSE WINDOW

Copyright Clearance Center RightsLink®

Home | Account Info | Help

Title:	Nanostructures of zinc oxide
Author:	Zhong Lin Wang
Publication:	Materials Today
Publisher:	Elsevier
Date:	June 2004

Logged in as:
Marwa Abd
Account #:
3000935814

LOGOUT

Order Completed

Thank you very much for your order.

This is a License Agreement between Marwa Abd-Ellah ("You") and Elsevier ("Elsevier"). The license consists of your order details, the terms and conditions provided by Elsevier, and the payment terms and conditions.

Get the printable license.

License Number	3670910274352
License date	Jul 16, 2015
Licensed content publisher	Elsevier
Licensed content publication	Materials Today
Licensed content title	Nanostructures of zinc oxide
Licensed content author	Zhong Lin Wang
Licensed content date	June 2004
Licensed content volume number	7
Licensed content issue number	6
Number of pages	8
Type of Use	reuse in a thesis/dissertation
Portion	figures/tables/illustrations
Number of figures/tables/illustrations	1
Format	both print and electronic
Are you the author of this Elsevier article?	No
Will you be translating?	No
Original figure numbers	Figure 1
Title of your thesis/dissertation	Hybrid Transparent Conductive Oxide Nanostructured Materials for Photovoltaic Applications
Expected completion date	Nov 2015
Estimated size (number of pages)	150
Elsevier VAT number	GB 494 6272 12
Permissions price	0.00 CAD
VAT/Local Sales Tax	0.00 CAD / 0.00 GBP
Total	0.00 CAD

ORDER MORE... | CLOSE WINDOW

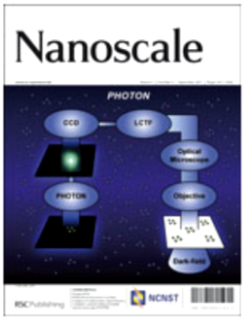

Title: Recent advances in solar cells based on one-dimensional nanostructure arrays

Author: Miao Yu,Yun-Ze Long,Bin Sun,Zhiyong Fan

Publication: Nanoscale

Publisher: Royal Society of Chemistry

Date: Mar 16, 2012

Order Completed

Thank you very much for your order.

This is a License Agreement between Marwa Abd-Ellah ("You") and Royal Society of Chemistry. The license consists of your order details, the terms and conditions provided by Royal Society of Chemistry, and the payment terms and conditions.

Get the printable license.

License Number	3670930404967
License date	Jul 16, 2015
Licensed content publisher	Royal Society of Chemistry
Licensed content publication	Nanoscale
Licensed content title	Recent advances in solar cells based on one-dimensional nanostructure arrays
Licensed content author	Miao Yu,Yun-Ze Long,Bin Sun,Zhiyong Fan
Licensed content date	Mar 16, 2012
Volume number	4
Issue number	9
Type of Use	Thesis/Dissertation
Requestor type	non-commercial (non-profit)
Portion	figures/tables/images
Number of figures/tables/images	1
Distribution quantity	50
Format	print and electronic
Will you be translating?	no
Order reference number	None
Title of the thesis/dissertation	Hybrid Transparent Conductive Oxide Nanostructured Materials for Photovoltaic Applications
Expected completion date	Nov 2015
Estimated size	150
Total	0.00 CAD

ORDER MORE... CLOSE WINDOW

Order Completed

Thank you very much for your order.

This is a License Agreement between Marwa Abd-Ellah ("You") and Royal Society of Chemistry. The license consists of your order details, the terms and conditions provided by Royal Society of Chemistry, and the payment terms and conditions.

Get the printable license.

License Number	3675501047573
License date	Jul 24, 2015
Licensed content publisher	Royal Society of Chemistry
Licensed content publication	Energy & Environmental Science
Licensed content title	Influence of the dye molecular structure on the TiO2 conduction band in dye-sensitized solar cells: disentangling charge transfer and electrostatic effects
Licensed content author	Enrico Ronca,Mariachiara Pastore,Leonardo Belpassi,Francesco Tarantelli,Filippo De Angelis
Licensed content date	Oct 19, 2012
Volume number	6
Issue number	1
Type of Use	Thesis/Dissertation
Requestor type	non-commercial (non-profit)
Portion	figures/tables/images
Number of figures/tables/images	1
Distribution quantity	50
Format	print and electronic
Will you be translating?	no
Order reference number	None
Title of the thesis/dissertation	Hybrid Transparent Conductive Oxide Nanostructured Materials for Photovoltaic Applications
Expected completion date	Nov 2015
Estimated size	150
Total	0.00 CAD

Title: Ruthenium dye functionalized gold nanoparticles and their spectral responses

Author: Linda Zedler,Frank Theil,Andrea Csáki,Wolfgang Fritzsche,Sven Rau,Michael Schmitt,Jürgen Popp,Benjamin Dietzek

Publication: RSC Advances

Publisher: Royal Society of Chemistry

Date: Apr 10, 2012

Order Completed

Thank you very much for your order.

This is a License Agreement between Marwa Abd-Ellah ("You") and Royal Society of Chemistry. The license consists of your order details, the terms and conditions provided by Royal Society of Chemistry, and the payment terms and conditions.

Get the printable license.

License Number	3675540051156
License date	Jul 24, 2015
Licensed content publisher	Royal Society of Chemistry
Licensed content publication	RSC Advances
Licensed content title	Ruthenium dye functionalized gold nanoparticles and their spectral responses
Licensed content author	Linda Zedler,Frank Theil,Andrea Csáki,Wolfgang Fritzsche,Sven Rau,Michael Schmitt,Jürgen Popp,Benjamin Dietzek
Licensed content date	Apr 10, 2012
Volume number	2
Issue number	10
Type of Use	Thesis/Dissertation
Requestor type	non-commercial (non-profit)
Portion	figures/tables/images
Number of figures/tables/images	2
Distribution quantity	50
Format	print and electronic
Will you be translating?	no
Order reference number	None
Title of the thesis/dissertation	Hybrid Transparent Conductive Oxide Nanostructured Materials for Photovoltaic Applications
Expected completion date	Nov 2015
Estimated size	150
Total	0.00 CAD

ORDER MORE... CLOSE WINDOW

Title: A novel tri-layered photoanode of hierarchical ZnO microspheres on 1D ZnO nanowire arrays for dye-sensitized solar cells

Author: Xiaohui Kang,Chunyang Jia,Zhongquan Wan,Jia Zhuang,Juan Feng

Publication: RSC Advances

Publisher: Royal Society of Chemistry

Date: Jan 28, 2015

Order Completed

Thank you very much for your order.

This is a License Agreement between Marwa Abd-Ellah ("You") and Royal Society of Chemistry. The license consists of your order details, the terms and conditions provided by Royal Society of Chemistry, and the payment terms and conditions.

Get the printable license.

License Number	3670951352725
License date	Jul 16, 2015
Licensed content publisher	Royal Society of Chemistry
Licensed content publication	RSC Advances
Licensed content title	A novel tri-layered photoanode of hierarchical ZnO microspheres on 1D ZnO nanowire arrays for dye-sensitized solar cells
Licensed content author	Xiaohui Kang,Chunyang Jia,Zhongquan Wan,Jia Zhuang,Juan Feng
Licensed content date	Jan 28, 2015
Volume number	5
Issue number	22
Type of Use	Thesis/Dissertation
Requestor type	non-commercial (non-profit)
Portion	figures/tables/images
Number of figures/tables/images	2
Distribution quantity	50
Format	print and electronic
Will you be translating?	no
Order reference number	None
Title of the thesis/dissertation	Hybrid Transparent Conductive Oxide Nanostructured Materials for Photovoltaic Applications
Expected completion date	Nov 2015
Estimated size	150
Total	0.00 CAD

ORDER MORE... CLOSE WINDOW

Order Completed

Thank you for your order.

This Agreement between Marwa Abd-Ellah ("You") and John Wiley and Sons ("John Wiley and Sons") consists of your license details and the terms and conditions provided by John Wiley and Sons and Copyright Clearance Center.

Your confirmation email will contain your order number for future reference.

Get the printable license.

License Number	3673681349899
License date	Jul 21, 2015
Licensed Content Publisher	John Wiley and Sons
Licensed Content Publication	Wiley Books
Licensed Content Title	Electrochemical Methods: Fundamentals and Applications, 2nd Edition
Licensed Content Author	Allen J. Bard, Larry R. Faulkner
Licensed Content Date	Dec 1, 2000
Licensed Content Pages	864
Type of use	Dissertation/Thesis
Requestor type	University/Academic
Format	Print and electronic
Portion	Figure/table
Number of figures/tables	1
Original Wiley figure/table number(s)	Figure 10.1.11
Will you be translating?	No
Title of your thesis / dissertation	Hybrid Transparent Conductive Oxide Nanostructured Materials for Photovoltaic Applications
Expected completion date	Nov 2015
Expected size (number of pages)	150
Requestor Location	Marwa Abd-Ellah 604-205 Victoria Street South Kitchener, ON N2G 4Z6 Canada Attn: Marwa Abd-Ellah
Billing Type	Invoice
Billing address	Marwa Abd-Ellah 604-205 Victoria Street South Kitchener, ON N2G 4Z6

Order Completed

Thank you very much for your order.

This is a License Agreement between Marwa Abd-Ellah ("You") and Springer ("Springer"). The license consists of your order details, the terms and conditions provided by Springer, and the payment terms and conditions.

Get the printable license.

License Number	3677181300039
License date	Jul 27, 2015
Licensed content publisher	Springer
Licensed content publication	Analytical and Bioanalytical Chemistry
Licensed content title	Fritz Scholz (Ed.): Electroanalytical methods. Guide to experiments and applications, 2nd ed.
Licensed content author	Daniel Mandler
Licensed content date	Jan 1, 2010
Volume number	398
Issue number	7
Type of Use	Thesis/Dissertation
Portion	Figures
Author of this Springer article	No
Original figure numbers	Figure 1.2.1
Title of your thesis / dissertation	Hybrid Transparent Conductive Oxide Nanostructured Materials for Photovoltaic Applications
Expected completion date	Nov 2015
Estimated size(pages)	150
Total	0.00 CAD

CLOSE WINDOW

Order Completed

Thank you for your order.

This Agreement between Marwa Abd-Ellah ("You") and John Wiley and Sons ("John Wiley and Sons") consists of your license details and the terms and conditions provided by John Wiley and Sons and Copyright Clearance Center.

Your confirmation email will contain your order number for future reference.

Get the printable license.

License Number	3673880580211
License date	Jul 21, 2015
Licensed Content Publisher	John Wiley and Sons
Licensed Content Publication	Wiley Books
Licensed Content Title	Handbook of Photovoltaic Science and Engineering, 2nd Edition
Licensed Content Author	Antonio Luque (Editor), Steven Hegedus (Co-Editor)
Licensed Content Date	Jan 1, 2011
Licensed Content Pages	1162
Type of use	Dissertation/Thesis
Requestor type	University/Academic
Format	Print and electronic
Portion	Figure/table
Number of figures/tables	1
Original Wiley figure/table number(s)	Figure 3.16
Will you be translating?	No
Title of your thesis / dissertation	Hybrid Transparent Conductive Oxide Nanostructured Materials for Photovoltaic Applications
Expected completion date	Nov 2015
Expected size (number of pages)	150
Requestor Location	Marwa Abd-Ellah 604-205 Victoria Street South Kitchener, ON N2G 4Z6 Canada Attn: Marwa Abd-Ellah
Billing Type	Invoice
Billing address	Marwa Abd-Ellah 604-205 Victoria Street South Kitchener, ON N2G 4Z6

Order Completed

Thank you very much for your order.

Click here for Payment Terms and Conditions.

Get a printable version for your records.

License Number	3674311354634
Order Date	Jul 22, 2015
Publisher	AIP Publishing LLC
Publication	Journal of Applied Physics
Article Title	Evaluation of the CdS/CdTe heterojunction solar cell
Author	Kim W. Mitchell,Alan L. Fahrenbruch,Richard H. Bube
Online Publication Date	Aug 26, 2008
Volume number	48
Issue number	10
Type of Use	Thesis/Dissertation
Requestor type	Student
Format	Print and electronic
Portion	Figure/Table
Number of figures/tables	1
Title of your thesis / dissertation	Hybrid Transparent Conductive Oxide Nanostructured Materials for Photovoltaic Applications
Expected completion date	Nov 2015
Estimated size (number of pages)	150
Total	0.00 CAD

ORDER MORE... CLOSE WINDOW

Bibliography

(1) Feynman, R. P. Plenty of Room at the Bottom. *Am. Phys. Soc. Proc.* **1959**.

(2) Nalwa, H. *Nanostructured materials and nanotechnology;* Concise ed.; San Diego, Academic Press., **2002**.

(3) Zhuiykov, S. *Nanostructured Semiconductor Oxides for the next Generation of Electronics and Functional Devices : Properties and Applications;* Woodhead Publishing Series in Electronic and Optical Materials. Cambridge, Woodhead Publishing, **2014**.

(4) Exarhos, G. J.; and Zhou, X. D. Discovery-based design of transparent conducting oxide films. *Thin Solid Films.* **2007**, 515, 7025-7052.

(5) Gordon, R. G. Criteria for Choosing Transparent Conductors. *MRS Bull.* **2000**, *25*, 52–57.

(6) Robertson, J.; and Falabretti, B. *Handbook of Transparent Conductors;* Hosono, H.; Paine, D. C.; Ginely, D., Ed.; New York, Springer US, **2011**.

(7) Fortunato, E.; Ginley, D.; Hosono, H.; Paine, D. C. Transparent Conducting Oxides for Photovoltaics. *MRS Bulliten* **2007**, *32*, 242–247.

(8) Look, D. C. Recent Advances in ZnO Materials and Devices. *Mater. Sci. Eng. B Solid-State Mater. Adv. Technol.* **2001**, *80*, 383–387.

(9) Look, D. C.; Reynolds, D. C.; Sizelove, J. R.; Jones, R. L.; Litton, C. W.; Cantwell, G.; Harsch, W. C. Electrical Properties of Bulk ZnO. *Solid State Commun.* **1998**, *105*, 399–401.

(10) Djurišić, A. B.; Chen, X.; Leung, Y. H.; Man Ching Ng, A. ZnO Nanostructures: Growth, Properties and Applications. *J. Mater. Chem.* **2012**, *22*, 6526-6535.

(11) Yi, G.-C.; Wang, C.; Park, W. Il. ZnO Nanorods: Synthesis, Characterization and Applications. *Semicond. Sci. Technol.* **2005**, *20*, S22–S34.

(12) Wang, Z. L. Nanostructures of Zinc Oxide. *Mater. Today* **2004**, *7*, 26–33.

(13) Gupta, A.; Mondal, K.; Sharma, A.; Bhattacharya, S. Superhydrophobic Polymethylsilsesquioxane Pinned One Dimensional ZnO Nanostructures for Water Remediation through Photo-Catalysis. *RSC Adv.* **2015**, *5*, 45897–45907.

(14) Arya, S. K.; Saha, S.; Ramirez-Vick, J. E.; Gupta, V.; Bhansali, S.; Singh, S. P. Recent Advances in ZnO Nanostructures and Thin Films for Biosensor Applications: Review. *Anal. Chim. Acta* **2012**, *737*, 1–21.

(15) Panda, D.; Tseng, T. Y. One-Dimensional ZnO Nanostructures: Fabrication, Optoelectronic Properties, and Device Applications. *J. Mater. Sci.* **2013**, *48*, 6849–6877.

(16) Feng, Z.; Jia, R.; Dou, B.; Li, H.; Jin, Z.; Liu, X.; Li, F.; Zhang, W.; Wu, C. Fabrication and Properties of ZnO Nanorods within Silicon Nanostructures for Solar Cell Application. *Appl. Phys. Lett.* **2015**, *106*, 053118-4.

(17) Li, Q.; Sun, X.; Lozano, K.; Mao, Y. Facile and Scalable Synthesis of "Caterpillar-Like" ZnO Nanostructures with Enhanced Photoelectrochemical Water-Splitting Effect. *J. Phys. Chem. C* **2014**, *118*, 13467–13475.

(18) Jarzebski, Z. M. Physical Properties of SnO_2, Materials. *J. Electrochem. Soc.: Reviews and News.* **1976**, 333C-346C.

(19) Toft Sørensen, O. *Nonstoichiometric Oxides. Materials Science and Technology*; New York, Academic Press, **1981**.

(20) Isono, T.; Fukuda, T.; Nakagawa, K.; Usui, R.; Satoh, R.; Morinaga, E.; Mihara, Y. High Conductivity SnO_2 Thin Films for Flat Panel Displays *SID Symposium Digest of Technical Papers.* **2006**, *37*, 1874–1877.

(21) Wang, H.; Liang, Q.; Wang, W.; An, Y.; Li, J.; Guo, L. Preparation of Flower-like SnO_2 Nanostructures and Their Applications in Gas-Sensing and Lithium Storage. *Cryst. Growth Des.* **2011**, *11*, 2942–2947.

(22) Wang, H.; Rogach, A. L. Hierarchical SnO_2 Nanostructures : Recent Advances in Design , Synthesis , and Applications. *Chem. Mater.* **2014**, 26, 123−133.

(23) Manjula, P.; Boppella, R.; Manorama, S. V. A Facile and Green Approach for the Controlled Synthesis of Porous SnO_2 Nanospheres: Application as an Efficient Photocatalyst and an Excellent Gas Sensing Material. *ACS Appl. Mater. Interfaces* **2012**, *4*, 6252–6260.

(24) Wang, Z.; Luan, D.; Boey, F. Y. C.; Lou, X. W. Fast Formation of SnO_2 Nanoboxes with Enhanced Lithium Storage Capability. *J. Am. Chem. Soc.* **2011**, *133*, 4738–4741.

(25) Zhao, Q.; Ma, L.; Zhang, Q.; Wang, C.; and Xu, X. SnO_2-Based Nanomaterials: Synthesis and Application in Lithium-Ion Batteries and Supercapacitors, *J. Nanomater.* **2015**, 2015, 1-15.

(26) Liu, R.; Yang, S.; Wang, F.; Lu, X.; Yang, Z.; Ding, B. Sodium Chloride Template Synthesis of Cubic Tin Dioxide Hollow Particles for Lithium Ion Battery Applications. *ACS Appl. Mater. Interfaces* **2012**, *4*, 1537–1542.

(27) Paek, S. M.; Yoo, E.; Honma, I. Enhanced Cyclic Performance and Lithium Storage Capacity of SnO_2/graphene Nanoporous Electrodes with Three-Dimensionally Delaminated Flexible Structure. *Nano Lett.* **2009**, *9*, 72–75.

(28) Pan, S. S.; Yu, S. F.; Zhang, Y. X.; Luo, Y. Y.; Wang, S.; Xu, J. M.; Li, G. H. Crystallite Size-Modulated Exciton Emission in SnO_2 Nanocrystalline Films Grown by Sputtering. *J. Appl. Phys.* **2013**, *113*, 143104-4.

(29) Choopun, S.; Hongsith, N.; Tanunchai, S.; Chairuangsri, T.; Krua-In, C.; Singkarat, S.; Vilaithong, T.; Mangkorntong, P.; Mangkorntong, N. Single-Crystalline ZnO Nanobelts by RF Sputtering. *J. Cryst. Growth* **2005**, *282*, 365–369.

(30) Jamal, R. K.; Hameed, M. A.; Adem, K. A. Optical Properties of Nanostructured ZnO Prepared by a Pulsed Laser Deposition Technique. *Mater. Lett.* **2014**, *132*, 31–33.

(31) Bazargan, S.; Leung, K. T. Catalyst-Assisted Pulsed Laser Deposition of One-Dimensional Single-Crystalline Nanostructures of tin(IV) Oxide: Interplay of VS and VLS Growth Mechanisms at Low Temperature. *J. Phys. Chem. C* **2012**, *116*, 5427–5434.

(32) Sinha, S. K.; Bhattacharya, R.; Ray, S. K.; Manna, I. Influence of Deposition Temperature on Structure and Morphology of Nanostructured SnO_2 Films Synthesized by Pulsed Laser Deposition. *Mater. Lett.* **2011**, *65*, 146–149.

(33) Pallotti, D. K.; Orabona, E.; Amoruso, S.; Aruta, C.; Bruzzese, R.; Chiarella, F.; Tuzi, S.; Maddalena, P.; Lettieri, S. Multi-Band Photoluminescence in TiO_2 Nanoparticles-Assembled Films Produced by Femtosecond Pulsed Laser Deposition. *J. Appl. Phys.* **2013**, *114*, 043503-9.

(34) Lakshmi, B. B.; Patrissi, C. J.; Martin, C. R. Sol- Gel Template Synthesis of Semiconductor Oxide Micro-and Nanostructures. *Chem. Mater* **1997**, *9*, 2544–2550.

(35) Li, J.; Srinivasan, S.; He, G. N.; Kang, J. Y.; Wu, S. T.; Ponce, F. A. Synthesis and Luminescence Properties of ZnO Nanostructures Produced by the Sol-Gel Method. *J. Cryst. Growth* **2008**, *310*, 599–603.

(36) Lee, J.; Easteal, A. J.; Pal, U.; Bhattacharyya, D. Evolution of ZnO Nanostructures in Sol-Gel Synthesis. *Curr. Appl. Phys.* **2009**, *9*, 792–796.

(37) Rani, S.; Suri, P.; Shishodia, P. K.; Mehra, R. M. Synthesis of Nanocrystalline ZnO Powder via Sol-Gel Route for Dye-Sensitized Solar Cells. *Sol. Energy Mater. Sol. Cells* **2008**, *92*, 1639–1645.

(38) Gu, F.; Wang, S. F.; Lü, M. K.; Zhou, G. J.; Xu, D.; Yuan, D. R. Photoluminescence Properties of SnO_2 Nanoparticles Synthesized by Sol−Gel Method. *J. Phys. Chem. B* **2004**, *108*, 8119–8123.

(39) Ghodsi, F. E.; Mazloom, J. Optical, Electrical and Morphological Properties of p-Type Mn-Doped SnO_2 Nanostructured Thin Films Prepared by Sol–gel Process. *Appl. Phys. A* **2012**, *108*, 693–700.

(40) Hamann, C. H. *Electrochemistry*; 2nd ed; New York, Wiley-VCH, **2007.**

(41) Holze, R. Piero Zanello: Inorganic Electrochemistry: Theory, Practice and Applications. *J. Solid State Electrochem.* **2006**, *10*, 512–513.

(42) Heinze, J. *Cyclic Voltammetry-Electrochmical Spectroscopy*; Angew. Chem. Int. Ed. Engl. **1984**, 23, 831-918.

(43) Garcia, E. M.; Lins, V. F. C.; and Matencio, T. *Modern Surface Engineering Treatments*; Aliofkhazraei, Ed.; InTech, Chapters, **2013**.

(44) Beranek, R.; Macak, J. M.; Gärtner, M.; Meyer, K.; Schmuki, P. Enhanced Visible Light Photocurrent Generation at Surface-Modified TiO_2 Nanotubes. *Electrochim. Acta* **2009**, *54*, 2640–2646.

(45) Zhang, C.; Van Overschelde, O.; Boudiba, A.; Snyders, R.; Olivier, M. G.; Debliquy, M. Improvement of Sensing Characteristics of Radio-Frequency Sputtered Tungsten Oxide Films through Surface Modification by Laser Irradiation. *Mater. Chem. Phys.* **2012**, *133*, 588–591.

(46) Tu, J.; Zhao, X. B.; Cao, G. S.; Zhuang, D. G.; Zhu, T. J.; Tu, J. P. Enhanced Cycling Stability of $LiMn_2O_4$ by Surface Modification with Melting Impregnation Method. *Electrochim. Acta* **2006**, *51*, 6456–6462.

(47) Zhang, C.; Wang, G.; Liu, M.; Feng, Y.; Zhang, Z.; Fang, B. A Hydroxylamine Electrochemical Sensor Based on Electrodeposition of Porous ZnO Nanofilms onto Carbon Nanotubes Films Modified Electrode. *Electrochim. Acta* **2010**, *55*, 2835–2840.

(48) Bedja, I.; Hotchandani, S.; Carpentier, R.; Fessenden, R. W.; Kamat, P. V. Chlorophyll B-Modified Nanocrystalline SnO_2 Semiconductor Thin Film as a Photosensitive Electrode. *J. Appl. Phys.* **1994**, *75*, 5444–5446.

(49) Li, Y.; Cai, W.; Duan, G.; Cao, B.; Sun, F.; Lu, F. Superhydrophobicity of 2D ZnO Ordered Pore Arrays Formed by Solution-Dipping Template Method. *J. Colloid Interface Sci.* **2005**, *287*, 634–639.

(50) Palomares, E.; Clifford, J. N.; Haque, S. A; Lutz, T.; Durrant, J. R. Slow Charge Recombination in Dye-Sensitised Solar Cells (DSSC) Using Al_2O_3 Coated Nanoporous TiO_2 Films. *Chem. Commun.* **2002**,14, 1464–1465.

(51) Chang, S. J.; Weng, W. Y.; Hsu, C. L.; Hsueh, T. J. High Sensitivity of a ZnO Nanowire-Based Ammonia Gas Sensor with Pt Nano-Particles. *Nano Commun. Netw.* **2010**, *1*, 283–288.

(52) Ren, C.; Yang, B.; Wu, M.; Xu, J.; Fu, Z.; Lv, Y.; Guo, T.; Zhao, Y.; Zhu, C. Synthesis of Ag/ZnO Nanorods Array with Enhanced Photocatalytic Performance. *J. Hazard. Mater.* **2010**, *182*, 123–129.

(53) Chandrasekharan, N.; Kamat, P. Improving the Photoelectrochemical Performance of Nanostructured TiO_2 Films by Adsorption of Gold Nanoparticles. *J. Phys. Chem. B* **2000**, *104*, 10851–10857.

(54) Huang, H.; Ong, C. Y. ; Guo, J.; White, T.; Tsea, M. S.; and Tan, O. K. Pt surface modification of SnO_2 nanorod arrays for CO and H_2 sensors *Nanoscale* **2010**, *2*, 1203-1207.

(55) Wang, C.; Astruc, D. Nanogold Plasmonic Photocatalysis for Organic Synthesis and Clean Energy Conversion. *Chem. Soc. Rev.* **2014**, *43*, 7188–7216.

(56) Kelly, K. L.; Coronado, E.; Zhao, L.; Coronado, E.; Schatz, G. C.; Zhao, L. L.; Schatz, G. C. The Optical Properties of Metal Nanoparticles: The Influence of Size, Shape, and Dielectric Environment. *J. Phys. Chem. B* **2003**, *107*, 668–677.

(57) Atwater, H. A; Polman, A. Plasmonics for Improved Photovoltaic Devices. *Nat. Mater.* **2010**, *9*, 205–213.

(58) Sakai, N.; Ikegami, M.; Miyasaka, T. MgO-Hybridized TiO_2 Interfacial Layers Assisting Efficiency Enhancement of Solid-State Dye-Sensitized Solar Cells. *Appl. Phys. Lett.* **2014**, *104*, 063303-5.

(59) Prasittichai, C.; Hupp, J. T. Surface Modification of SnO_2 Photoelectrodes in Dye-Sensitized Solar Cells: Significant Improvements in Photovoltage via Al_2O_3 Atomic Layer Deposition. *J. Phys. Chem. Lett.* **2010**, *1*, 1611–1615.

(60) Kang, S. H.; Kim, J.-Y.; Kim, Y.; Kim, H. S.; Sung, Y. E. Surface Modification of Stretched TiO_2 Nanotubes for Solid-State Dye-Sensitized Solar Cells. *J. Phys. Chem. B* **2007**, *111*, 9614–9623.

(61) Saxena, V.; Aswal, D. K. Surface Modifications of Photoanodes in Dye Sensitized Solar Cells: Enhanced Light Harvesting and Reduced Recombination. *Semicond. Sci. Technol.* **2015**, *30*, 064005-23.

(62) Kalyanasundaram, K. ; and Gratzel, M. Dye-sensitized solar cells based on redox active monolayers adsorbed on nanocrystalline oxide semiconductor films. *International Symposium on Micelles, Microemulsions, and Monolayers: Science and Technology* **1995**, 579-603.

(63) Palomares, E.; Clifford, J. N.; Haque, S. A; Lutz, T.; Durrant, J. R. Control of Charge Recombination Dynamics in Dye Sensitized Solar Cells by the Use of Conformally Deposited Metal Oxide Blocking Layers. J. Am. Chem. Soc. **2003**, 125, 475–482.

(64) Yu, M.; Long, Y.-Z.; Sun, B.; Fan, Z. Recent Advances in Solar Cells Based on One-Dimensional Nanostructure Arrays. *Nanoscale* **2012**, *4*, 2783-2796.

(65) Kirchartz, T.; Bisquert, J.; Mora-Sero; Ivan; Garcia-Belmonte, G. Classification of Solar Cells according to Mechanisms of Charge Separation and Charge Collection. *Phys. Chem. Chem.*

Phys. **2015**, 17, 4007–4014.

(66) Labouret, A.; and Villoz, M. *Solar Photovoltaic Energy. IET Renewable Energy Series;* Stevenage, Institution of Engineering and Technology, **2010**.

(67) Meyers, P.V. Advances In CdTe n-i-p Photovoltaics. *Solar Cells*. **1989**, 27, 91–98.

(68) Callister, W. D.; and Rethwisch, D. G. *Fundamentals of Materials Science and Engineering : An Integrated Approach*; 4th ed.; New Jersy, Wiley, **2012**.

(69) Beard, M. C.; Luther, J. M.; Nozik, A. J. The Promise and Challenge of Nanostructured Solar Cells. *Nat. Nanotechnol.* **2014**, *9*, 951–954.

(70) Conibeer, G.; Green, M.; Corkish, R.; Cho, Y.; Cho, E. C.; Jiang, C. W.; Fangsuwannarak, T.; Pink, E.; Huang, Y.; Puzzer, T.; et al. Silicon Nanostructures for Third Generation Photovoltaic Solar Cells. *Thin Solid Films* **2006**, *511-512*, 654–662.

(71) Conibeer, G.; Green, M.; Cho, E. C.; König, D.; Cho, Y. H.; Fangsuwannarak, T.; Scardera, G.; Pink, E.; Huang, Y.; Puzzer, T.; Huang, S.; Song, D.; Flynn, C.; Park, S.; Hao, X.; Mansfield, D. Silicon Quantum Dot Nanostructures for Tandem Photovoltaic Cells. *Thin Solid Films* **2008**, *516*, 6748–6756.

(72) Hao, X. J.; Cho, E. C.; Flynn, C.; Shen, Y. S.; Park, S. C.; Conibeer, G.; Green, M. A. Synthesis and Characterization of Boron-Doped Si Quantum Dots for All-Si Quantum Dot Tandem Solar Cells. *Sol. Energy Mater. Sol. Cells* **2009**, *93*, 273–279.

(73) Hao, X. J.; Cho, E.-C.; Scardera, G.; Shen, Y. S.; Bellet-Amalric, E.; Bellet, D.; Conibeer, G.; Green, M. a. Phosphorus-Doped Silicon Quantum Dots for All-Silicon Quantum Dot Tandem Solar Cells. *Sol. Energy Mater. Sol. Cells* **2009**, *93*, 1524–1530.

(74) Kamat, P. V. Quantum Dot Solar Cells. Semiconductor Nanocrystals as Light Harvesters. *J. Phys. Chem. C* **2008**, *112*, 18737–18753.

(75) Vera-Marquina, A.; Leal Cruz, A. L.; Berman, D.; Zaldivar, I.; García, L. a.; García, A.; Rojas, A. G. Optical Properties of Annealed CdS-Nanostructured Films for Solar Cells. *Front. Opt.* **2014**, 1, FW2B.6.

(76) McShane, C. M.; Siripala, W. P.; Choi, K. S. Effect of Junction Morphology on the Performance of Polycrystalline Cu_2O Homojunction Solar Cells. *J. Phys. Chem. Lett.* **2010**, *1*, 2666–2670.

(77) Fan, Z.; Ho, J. C.; Huang, B. *One-Dimensional Nanostructures for Energy Harvesting, in One-Dimensional Nanostructures;* Zhai, T. and Yao, J., Ed.; New Jersy, John Wiley & Sons, Inc., **2012**.

(78) Chen, X.; Lin, P.; Yan, X.; Bai, Z.; Yuan, H.; Shen, Y.; Liu, Y.; Zhang, G.; Zhang, Z.; Zhang,

Y. Three-Dimensional Ordered ZnO/Cu_2O Nanoheterojunctions for Efficient Metal–Oxide Solar Cells. *ACS Appl. Mater. Interfaces* **2015**, *7*, 3216–3223.

(79) Li, B.; Wang, L.; Kang, B.; Wang, P.; Qiu, Y. Review of Recent Progress in Solid-State Dye-Sensitized Solar Cells. *Sol. Energy Mater. Sol. Cells* **2006**, *90*, 549–573.

(80) Ronca, E.; Pastore, M.; Belpassi, L.; Tarantelli, F.; De Angelis, F. Influence of the Dye Molecular Structure on the TiO_2 Conduction Band in Dye-Sensitized Solar Cells: Disentangling Charge Transfer and Electrostatic Effects. *Energy Environ. Sci.* **2012**, 6, 183–193.

(81) O'Regan, B.; Grätzel, M. A Low-Cost, High-Efficiency Solar Cell Based on Dye-Sensitized Colloidal TiO_2 Films. *Nature* **1991**, *353*, 737–740.

(82) Zedler, L.; Theil, F.; Csáki, A.; Fritzsche, W.; Rau, S.; Schmitt, M.; Popp, J.; Dietzek, B. Ruthenium Dye Functionalized Gold Nanoparticles and Their Spectral Responses. *RSC Adv.* **2012**, *2*, 4463-4471

(83) Qin, Y.; Peng, Q. Ruthenium Sensitizers and Their Applications in Dye-Sensitized Solar Cells. *Int. J. Photoenergy* **2012**,1-21.

(84) Polizzotti, A.; Schual-berke, J.; Falsgraf, E.; Johal, M. *Third Generation Photovoltaics;* InTecOpen, **2012**.

(85) Kalyanasundaram, K. *Dye-sensitized Solar Cells*; Lausanne, EFPL Press, **2010**.

(86) Shao, F.; Sun, J.; Gao, L.; Yang, S.; Luo, J. Forest-like TiO_2 Hierarchical Structures for Efficient Dye-Sensitized Solar Cells. *J. Mater. Chem.* **2012**, *22*, 6824-6830.

(87) Liao, J. Y.; He, J. W.; Xu, H.; Kuang, D. B.; Su, C. Y. Effect of TiO_2 Morphology on Photovoltaic Performance of Dye-Sensitized Solar Cells: Nanoparticles, Nanofibers, Hierarchical Spheres and Ellipsoid Spheres. *J. Mater. Chem.* **2012**, *22*, 7910-7918.

(88) Chen, H. Y.; Kuang, D. B.; Su, C. Y. Hierarchically Micro/nanostructured Photoanode Materials for Dye-Sensitized Solar Cells. *J. Mater. Chem.* **2012**, *22*, 15475-15489.

(89) Tiwana, P.; Docampo, P.; Johnston, M. B.; Snaith, H. J.; Herz, L. M. Electron Mobility and Injection Dynamics in Mesoporous ZnO, SnO_2, and TiO_2 Films Used in Dye-Sensitized Solar Cells. *ACS Nano* **2011**, *5*, 5158–5166.

(90) Zhang, Q. F.; Dandeneau, C. S.; Zhou, X. Y.; Cao, G. Z. ZnO Nanostructures for Dye-Sensitized Solar Cells. *Adv. Mater.* **2009**, *21*, 4087–4108.

(91) Green, A. N. M.; Palomares, E.; Haque, S. A; Kroon, J. M.; Durrant, J. R. Charge Transport versus Recombination in Dye-Sensitized Solar Cells Employing Nanocrystalline TiO_2 and SnO_2 Films. *J. Phys. Chem. B* **2005**, *109*, 12525–12533.

(92) Kang, X.; Jia, C.; Wan, Z.; Zhuang, J.; Feng, J. A Novel Tri-Layered Photoanode of Hierarchical ZnO Microspheres on 1D ZnO Nanowire Arrays for Dye-Sensitized Solar Cells. *RSC Adv.* **2015**, *5*, 16678–16683.

(93) Bard, A. J.; and Faulkner, L. R. *Electrochemical Methods : Fundamentals and Applications*; 2nd ed.; New York, John Wiley, **2001**.

(94) Heinze, J. *Cyclic Voltammetry—Electrochemical Spectroscopy*; Angew, Chemie Int. Ed.*;* **1984**, *23*, 831–847.

(95) Scholz, F.; and Bond, A. M. *Electroanalytical Methods Guide to Experiments and Applications*; 2nd ed.; New York, Springer, 2010.

(96) Macdonald, J. R. *Impedance Spectroscopy Theory, Experiment, and Applications*; Barsoukov, and Macdonald, (ed.); 2nd ed, Hoboken, Wiley, **2007**.

(97) Orazem, M. E.; and Tribollet, B. *Electrochemical Impedance Spectroscopy*. *Electrochemical Society Series*; New Jersy, Wiley, **2008**.

(98) Newman, J. S.; and Thomas-Alyea, K. E. *Electrochemical Systems*; New Jersy, Wiley-Interscience, **2004**.

(99) Brandon, D. G.; and Kaplan, W. D. *Microstructural Characterization of Materials*; 2nd ed.; Chichester, John Wiley, **2008.**

(100) Carl Zeiss SMT Inc. *Instruction Manual: SEM MERLIN Users Manual*, **2013**.

(101) Joy, D. C. Scanning He^+ Ion Beam Microscopy and Metrology. *AIP Conf. Proc.* **2011**, *1395*, 80–84.

(102) Postek, M. T.; Vladar, A. E.; Kramar, J.; Stern, L. A.; Notte, J.; McVey, S. Helium Ion Microscopy: A New Technique for Semiconductor Metrology and Nanotechnology. *AIP Conf. Proc.* **2007**, *931*, 161–167.

(103) Carl Zeiss SMT Inc. *Instruction Manual: Orion Plus Helium Ion Microscope,* **2009**.

(104) Williams, D. B.; Carter, C. B. *Transmission Electron Microscopy: A Textbook for Materials Science*; New York, SpringerUS, **2009**.

(105) Carl Zeiss SMT Inc. *Instruction Manual: Libra 200 MC Transmission Electron Microscope*, **2013**.

(106) Warren, B. E. *X-ray Diffraction*; Dover ed.; New York, Dover Publications, **1990**.

(107) Kimura, M. X-Ray Evanescent Diffraction: Application to Metal Surfaces. **1999**, *16*, 25–31.

(108) Vickerman, J. C. *Surface Analysis : The Principal Techniques*; New York, John Wiley, **1997**.

(109) Woodruff, D. P, and Delchar, T. A. *Modern Techniques of Surface Science*; 2nd ed.; Cambridge Solid State Science Series; Cambridge University Press, **1994**.

(110) Thompson, M. *Auger Electron Spectroscopy Chemical Analysis*, New York, Wiley, **1985**.

(111) Moulder, J. F.; Stickle, W. F.; Sobol, P. E. *Handbook of X Ray Photoelectron Spectroscopy;* Chastain, J., (ed.); 2nd ed.; Physical Electronics Inc., Eden Prairie, **1992**.

(112) Watts, J. F.; Wolstenholme, J.; *An Introduction to surface analysis by XPS and AES*, Chichester, Wiley, **2003**.

(113) Michler, G. H. Atomic Force Microscopy. *Electron Microsc. Polym.* **2008**, 121–143.

(114) Asylum Research. *Instruction Manual: Cypher™ Atomic Force Microscope*, **2014**.

(115) Ecopia corp. *Instruction Manual: Ecopia HMS-5300 Hall Effect Measurment*, **2005**.

(116) Taylor, J. L. *Reflectance Measurements of Materials Used in the Solar Industry Selecting the Appropriate Accessories for UV / Vis / NIR Measurements. Instruction Manual: Lambda 1050 UV/Vis spectrometer.* PerkinElmer, Inc. **2005**.

(117) Wang, L.; You, J.; Shi, J.; Peng, B.; and Chu, P. K. *Improving solar-cell efficiency*; SPIE Newsroom. **2009**.

(118) PV Measurment Inc. *Instruction Manual: Solar Cell I-V Testing System Model IV-5*, **2011**.

(119) Luque, A.; and Hegedus, Steven. *Handbook of Photovoltaic Science and Engineering*; 2nd ed.; Chichester, Wiley, **2011**.

(120) PV Measurment Inc. I*nstruction Manual: QEX10 Solar Cell IPCE Spectral Response Measurement System.* **2011.**

(121) Bube, R. H. *Photovoltaic Materials. Series on Properties of Semiconductor Materials*; London, Imperial College Press , World Scientific, **1998**.

(122) Mitchell, K. W.; Fahrenbruch, A. L.; Bube, R. H. Evaluation of the CdS/CdTe Heterojunction Solar Cell. *J. Appl. Phys.* **1977**, *48*, 4365–4371.

(123) Zhang, X. .; Dai, J. .; Ong, H. .; Wang, N.; Chan, H. L. .; Choy, C. . Hydrothermal Synthesis of Oriented ZnO Nanobelts and Their Temperature Dependent Photoluminescence. *Chem. Phys. Lett.* **2004**, *393*, 17–21.

(124) Xu, S.; Wei, Y.; Kirkham, M.; Liu, J.; Mai, W.; Davidovic, D.; Snyder, R. L.; Wang, Z. L. Patterned Growth of Vertically Aligned ZnO Nanowire Arrays on Inorganic Substrates at Low

Temperature without Catalyst. *J. Am. Chem. Soc.* **2008**, *130*, 14958–14959.

(125) Xu, F.; Lu, Y.; Xie, Y.; Liu, Y. Controllable Morphology Evolution of Electrodeposited ZnO Nano/micro-Scale Structures in Aqueous Solution. *Mater. Des.* **2009**, *30*, 1704–1711.

(126) Liu, B.; Zeng, H. C. Direct Growth of Enclosed ZnO Nanotubes. *Nano Res.* **2009**, *2*, 201–209.

(127) Hughes, W. L.; Wang, Z. L. Controlled Synthesis and Manipulation of ZnO Nanorings and Nanobows. *Appl. Phys. Lett.* **2005**, *86*, 043106-3.

(128) Gao, P.; Ding, Y.; Wang, Z. L. Electronic Transport in Superlattice-Structured ZnO Nanohelix *Nano Lett*. 2009, 9, 137-143.

(129) Kong, X. Y.; Wang, Z. L. Spontaneous Polarization-Induced Nanohelixes, Nanosprings, and Nanorings of Piezoelectric Nanobelts. *Nano Lett.* **2003**, *3*, 1625–1631.

(130) Pradhan, D.; Sindhwani, S.; Leung, K. T. Parametric Study on Dimensional Control of ZnO Nanowalls and Nanowires by Electrochemical Deposition. *Nanoscale Res. Lett.* **2010**, *5*, 1727–1736.

(131) Zhai, T.; Xie, S.; Zhao, Y.; Sun, X.; Lu, X.; Yu, M.; Xu, M.; Xiao, F.; Tong, Y. Controllable Synthesis of Hierarchical ZnO Nanodisks for Highly Photocatalytic Activity. *CrystEngComm* **2012**, *14*, 1850-1855.

(132) Gao, P. X.; Wang, Z. L. Nanopropeller Arrays of Zinc Oxide. *Appl. Phys. Lett.* **2004**, *84*, 2883-2885.

(133) Pradhan, D.; Kumar, M.; Ando, Y.; Leung, K. T. Fabrication of ZnO Nanospikes and Nanopillars on ITO Glass by Templateless Seed-Layer-Free Electrodeposition and Their Field-Emission Properties. *ACS Appl. Mater. Interfaces* **2009**, *1*, 789–796.

(134) Pradhan, D.; Leung, K. T. Vertical Growth of Two-Dimensional Zinc Oxide Nanostructures on ITO-Coated Glass: Effects of Deposition Temperature and Deposition Time. *J. Phys. Chem. C* **2008**, *112*, 1357–1364.

(135) Li, L.; Pan, S.; Dou, X.; Zhu, Y.; Huang, X.; Yang, Y. Direct Electrodeposition of ZnO Nanotube Arrays in Anodic Alumina Membranes. **2010**, 111, 7288–7291.

(136) Tang, Y.; Luo, L.; Chen, Z.; Jiang, Y.; Li, B.; Jia, Z.; Xu, L. Electrodeposition of ZnO Nanotube Arrays on TCO Glass Substrates. *Electrochem. commun.* **2007**, *9*, 289–292.

(137) Xu, F.; Chen, J.; Guo, L.; Lei, S.; Ni, Y. In Situ Electrochemically Etching-Derived ZnO Nanotube Arrays for Highly Efficient and Facilely Recyclable Photocatalyst. *Appl. Surf. Sci.* **2012**, *258*, 8160–8165.

(138) Chu, D.; Masuda, Y.; Ohji, T.; Kato, K. Formation and Photocatalytic Application of ZnO

Nanotubes Using Aqueous Solution. *Langmuir* **2010**, *26*, 2811–2815.

(139) Wei, A.; Sun, X. W.; Xu, C. X.; Dong, Z. L.; Yu, M. B.; Huang, W. Stable Field Emission from Hydrothermally Grown ZnO Nanotubes. *Appl. Phys. Lett.* **2006**, *88*, 213102-3.

(140) Wang, J. X.; Sun, X. W.; Yang, Y.; Wu, C. M. L. N-P Transition Sensing Behaviors of ZnO Nanotubes Exposed to NO_2 Gas. *Nanotechnology* **2009**, *20*, 465501-4.

(141) Vayssieres, L.; Keis, K.; Hagfeldt, A.; Lindquist, S.-E. Three-Dimensional Array of Highly Oriented Crystalline ZnO Microtubes. *Chem. Mater.* **2001**, *13*, 4395–4398.

(142) Xu, L.; Liao, Q.; Zhang, J.; Ai, X.; Xu, D. Single-Crystalline ZnO Nanotube Arrays on Conductive Glass Substrates by Selective Disolution of Electrodeposited ZnO Nanorods. *J. Phys. Chem. C* **2007**, *111*, 4549–4552.

(143) Yu, H.; Zhang, Z.; Han, M.; Hao, X.; Zhu, F. A General Low-Temperature Route for Large-Scale Fabrication of Highly Oriented ZnO Nanorod/nanotube Arrays. *J. Am. Chem. Soc.* **2005**, *127*, 2378–2379.

(144) She, G. W.; Zhang, X. H.; Shi, W. S.; Fan, X.; Chang, J. C.; Lee, C. S.; Lee, S. T.; Liu, C. H. Controlled Synthesis of Oriented Single-Crystal ZnO Nanotube Arrays on Transparent Conductive Substrates. *Appl. Phys. Lett.* **2008**, *92*, 90–93.

(145) Jeong, J. S.; Lee, J. Y.; Cho, J. H.; Suh, H. J.; Lee, C. J. Single-Crystalline ZnO Microtubes Formed by Coalescence of ZnO Nanowires Using a Simple Metal-Vapor Deposition Method. *Chem. Mater.* **2005**, *17*, 2752–2756.

(146) Mensah, S. L.; Kayastha, V. K.; Ivanov, I. N.; Geohegan, D. B.; Yap, Y. K. Formation of Single Crystalline ZnO Nanotubes without Catalysts and Templates. *Appl. Phys. Lett.* **2007**, *90*, 113108-3.

(147) Xing, Y. J.; Xi, Z. H.; Zhang, X. D.; Song, J. H.; Wang, R. M.; Xu, J.; Xue, Z. Q.; Yu, D. P. Nanotubular Structures of Zinc Oxide. *Solid State Commun.* **2004**, *129*, 671–675.

(148) Zhang, B. P.; Binh, N. T.; Wakatsuki, K.; Segawa, Y.; Yamada, Y.; Usami, N.; Kawasaki, M.; Koinuma, H. Formation of Highly Aligned ZnO Tubes on Sapphire (0001) Substrates. *Appl. Phys. Lett.* **2004**, *84*, 4098–4100.

(149) Pradhan, D.; Leung, K. T. Controlled Growth of Two-Dimensional and One-Dimensional ZnO Nanostructures on Indium Tin Oxide Coated Glass by Direct Electrodeposition. *Langmuir* **2008**, *24*, 9707–9716.

(150) Jiangfeng, G.; Zhaoming, D.; Qingping, D.; Yuan, X.; Weihua, Z. Controlled Synthesis of ZnO Nanostructures by Electrodeposition Method. *J. Nanomater.* **2010**, 2010, 1–6.

(151) Pauporté, T.; Lincot, D. Hydrogen Peroxide Oxygen Precursor for Zinc Oxide

Electrodeposition II- Mechanistic aspects. *Journal of Electroanal. Chem.* **2001**, 517, 54–62.

(152) Choi, K. S.; Lichtenegger, H. C.; Stucky, G. D.; McFarland, E. W. Electrochemical Synthesis of Nanostructured ZnO Films Utilizing Self-Assembly of Surfactant Molecules at Solid-Liquid Interfaces. *J. Am. Chem. Soc.* **2002**, *124*, 12402–12403.

(153) Musselman, K. P.; Gershon, T.; Schmidt-Mende, L.; MacManus-Driscoll, J. L. Macroscopically Uniform Electrodeposited ZnO Films on Conducting Glass by Surface Tension Modification and Consequent Demonstration of Significantly Improved P-N Heterojunctions. *Electrochim. Acta* **2011**, *56*, 3758–3763.

(154) Ott, A. W.; Chang, R. P. H. Atomic Layer-Controlled Growth of Transparent Conducting ZnO on Plastic Substrates. *Mater. Chem. Phys.* **1999**, *58*, 132–138.

(155) Elias, J.; Tena-Zaera, R.; Lévy-Clément, C. Electrodeposition of ZnO Nanowires with Controlled Dimensions for Photovoltaic Applications: Role of Buffer Layer. *Thin Solid Films* **2007**, *515*, 8553–8557.

(156) Lupan, O.; Guérin, V. M.; Tiginyanu, I. M.; Ursaki, V. V.; Chow, L.; Heinrich, H.; Pauporté, T. Well-Aligned Arrays of Vertically Oriented ZnO Nanowires Electrodeposited on ITO-Coated Glass and Their Integration in Dye Sensitized Solar Cells. *J. Photochem. Photobiol. A Chem.* **2010**, *211*, 65–73.

(157) Cui, J.; Gibson, U. J. A Simple Two-Step Electrodeposition of Cu_2O / ZnO Nanopillar Solar Cells. *J. Phys. Chem. C* **2010**, *114*, 6408–6412.

(158) Pradhan, D.; Kumar, M.; Ando, Y.; Leung, K. T. Efficient Field Emission from Vertically Grown Planar ZnO Nanowalls on an ITO-Glass Substrate. *Nanotechnology* **2008**, *19*, 035603-6.

(159) Elias, J.; Tena-Zaera, R.; and Lévy-Clément, C. Effect of the Chemical Nature of the Anions on the Electrodeposition of ZnO Nanowire Arrays. *J. Phys.C* **2008**, 112, 5736–5741.

(160) Xu, C.; Kim, B.-S.; Lee, J.-H.; Kim, M.; Hwang, S. W.; Choi, B. L.; Lee, E. K.; Kim, J. M.; Whang, D. Seed-Free Electrochemical Growth of ZnO Nanotube Arrays on Single-Layer Graphene. *Mater. Lett.* **2012**, *72*, 25–28.

(161) Jiang, C. Y.; Sun, X. W.; Lo, G. Q.; Kwong, D. L.; Wang, J. X. Improved Dye-Sensitized Solar Cells with a ZnO-Nanoflower Photoanode. *Appl. Phys. Lett.* **2007**, *90*, 263501-3.

(162) Kotsis, K.; Staemmler, V. Ab Initio Calculations of the O1s XPS Spectra of ZnO and Zn Oxo Compounds. *Phys. Chem. Chem. Phys.* **2006**, *8*, 1490–1498.

(163) Xu, S.; Wang, Z. L. One-Dimensional ZnO Nanostructures: Solution Growth and Functional Properties. *Nano Res.* **2011**, *4*, 1013–1098.

(164) Wright, M. R. *An Introduction to Aqueous Electrolyte Solutions*; Chichester, John Wiley, **2007**.

(165) Coury, L. Conductance Measurements Part 1; Theory. *Curr. Sep.* **1999**, *18*, 91–96.

(166) Kidowaki, H.; Oku, T.; Akiyama, T. Fabrication and Characterization of CuO/ZnO Solar Cells. *J. Phys. Conf. Ser.* **2012**, *352*, 012022-5.

(167) Law, M.; Greene, L. E.; Johnson, J. C.; Saykally, R.; Yang, P. Nanowire Dye-Sensitized Solar Cells. *Nat. Mater.* **2005**, *4*, 455–459.

(168) Anta, J. A.; Guillén, E.; Tena-Zaera, R. ZnO-Based Dye-Sensitized Solar Cells. *J. Phys. Chem. C* **2012**, *116*, 11413–11425.

(169) Martinson, A. B. F.; Elam, J. W.; Hupp, J. T.; Pellin, M. J. ZnO Nanotube Based Dye-Sensitized Solar Cells. *Nano Lett.* **2007**, *7*, 2183–2187.

(170) Han, J.; Fan, F.; Xu, C.; Lin, S.; Wei, M.; Duan, X.; Wang, Z. L. ZnO Nanotube-Based Dye-Sensitized Solar Cell and Its Application in Self-Powered Devices. *Nanotechnology* **2010**, *21*, 405203-7.

(171) Pradhan, D.; Mohapatra, S. K.; Tymen, S.; Misra, M.; Leung, K. T. Morphology-Controlled ZnO Nanomaterials for Enhanced Photoelectrochemical Performance. *Mater. Express* **2011**, *1*, 59–67.

(172) Spinelli, P.; Polman, A. Light Trapping in Thin Crystalline Si Solar Cells Using Surface Mie Scatterers. *IEEE J. Photovoltaics* **2014**, *4*, 554–559.

(173) Panthani, M. G.; Kurley, J. M.; Crisp, R. W.; Dietz, T. C.; Ezzyat, T.; Luther, J. M.; Talapin, D. V. High Efficiency Solution Processed Sintered CdTe Nanocrystal Solar Cells: The Role of Interfaces. *Nano Lett.* **2014**, *14*, 670–675.

(174) Chou, S. M.; Hon, M. H.; Leu, I. C.; Lee, Y. H. Al-Doped ZnO/Cu_2O Heterojunction Fabricated on (200) and (111)-Orientated Cu_2O Substrates. *J. Electrochem. Soc.* **2008**, *155*, H923-H928.

(175) Wei, H.; Gong, H.; Wang, Y.; Hu, X.; Chen, L.; Xu, H.; Liu, P.; Cao, B. Three Kinds of Cu_2O/ZnO Heterostructure Solar Cells Fabricated with Electrochemical Deposition and Their Structure-Related Photovoltaic Properties. *CrystEngComm* **2011**, *13*, 6065-6070.

(176) Nolan, M.; Elliott, S. D. The P-Type Conduction Mechanism in Cu_2O: A First Principles Study. *Phys. Chem. Chem. Phys.* **2006**, *8*, 5350–5358.

(177) Xu, H.; Wang, W.; Zhu, W. Shape Evolution and Size-Controllable Synthesis of Cu_2O Octahedra and Their Morphology-Dependent Photocatalytic Properties. *J. Phys. Chem. B* **2006**, *110*, 13829–13834.

(178) Liang, J.; Kishi, N.; Soga, T.; Jimbo, T.; Ahmed, M. Thin Cuprous Oxide Films Prepared by Thermal Oxidation of Copper Foils with Water Vapor. *Thin Solid Films* **2012**, *520*, 2679–2682.

(179) Deuermeier, J.; Gassmann, J.; Brötz, J.; Klein, A. Reactive Magnetron Sputtering of Cu_2O: Dependence on Oxygen Pressure and Interface Formation with Indium Tin Oxide. *J. Appl. Phys.* **2011**, *109*, 113704-7.

(180) Jeong, S. S.; Mittiga, A.; Salza, E.; Masci, A.; Passerini, S. Electrodeposited ZnO/Cu_2O Heterojunction Solar Cells. *Electrochim. Acta* **2008**, *53*, 2226–2231.

(181) Hsu, Y.-K.; Lin, H.-H.; Wu, J.-R.; Chen, M.-H.; Chen, Y.-C.; Lin, Y.-G. Electrochemical Growth and Characterization of a p-Cu_2O Thin Film on n-ZnO Nanorods for Solar Cell Application. *RSC Adv.* **2014**, *4*, 7655-7659.

(182) Zoolfakar, A. S.; Rani, R. A.; Morfa, A. J.; Balendhran, S.; O'Mullane, A. P.; Zhuiykov, S.; Kalantar-zadeh, K. Enhancing the Current Density of Electrodeposited ZnO–Cu_2O Solar Cells by Engineering Their Heterointerfaces. *J. Mater. Chem.* **2012**, *22*, 21767-21775.

(183) Noda, S.; Shima, H.; Akinaga, H. Cu_2O/ZnO Heterojunction Solar Cells Fabricated by Magnetron-Sputter Deposition Method Films Using Sintered Ceramics Targets. *J. Phys. Conf. Ser.* **2013**, *433*, 012027-10.

(184) Minami, T.; Nishi, Y.; Miyata, T.; Nomoto, J. I. High-Efficiency Oxide Solar Cells with ZnO/Cu_2O Heterojunction Fabricated on Thermally Oxidized Cu_2O Sheets. *Appl. Phys. Express* **2011**, *4*, 062301-3.

(185) Chen, J. W.; Perng, D. C.; Fang, J. F. Nano-Structured Cu_2O Solar Cells Fabricated on Sparse ZnO Nanorods. *Sol. Energy Mater. Sol. Cells* **2011**, *95*, 2471–2477.

(186) Perng, D. C.; Chen, J. W.; Kao, T. T.; Chang, R. P. Cu_2O Growth Characteristics on an Array of ZnO Nanorods for the Nano-Structured Solar Cells. *Surf. Coatings Technol.* **2013**, *231*, 261–266.

(187) Guerguerian, G.; Elhordoy, F.; Pereyra, C. J.; Marotti, R. E.; Martín, F.; Leinen, D.; Ramos-Barrado, J. R.; Dalchiele, E. A. ZnO/Cu_2O Heterostructure Nanopillar Arrays: Synthesis, Structural and Optical Properties. *J. Phys. D. Appl. Phys.* **2012**, *45*, 245301-10.

(188) Izaki, M.; Shinagawa, T.; Mizuno, K.-T.; Ida, Y.; Inaba, M.; Tasaka, A. Electrodeposited Cu_2O/n-ZnO Heterojunction Diode for Photovoltaic Device. *J. Phys. D. Appl. Phys.* **2007**, *40*, 3326–3329.

(189) Musselman, K. P.; Marin, A.; Wisnet, A.; Scheu, C.; MacManus-Driscoll, J. L.; Schmidt-Mende, L. A Novel Buffering Technique for Aqueous Processing of Zinc Oxide Nanostructures and Interfaces, and Corresponding Improvement of Electrodeposited ZnO-Cu_2O Photovoltaics. *Adv. Funct. Mater.* **2011**, *21*, 573–582.

(190) Akimoto, K.; Ishizuka, S.; Yanagita, M.; Nawa, Y.; Paul, G. K.; Sakurai, T. Thin Film Deposition of Cu_2O and Application for Solar Cells. *Sol. Energy* **2006**, *80*, 715–722.

(191) Liu, Y.; Turley, H. K.; Tumbleston, J. R.; Samulski, E. T.; Lopez, R. Minority Carrier Transport Length of Electrodeposited Cu_2O in ZnO/Cu_2O Heterojunction Solar Cells. *Appl. Phys. Lett.* **2011**, *98*, 162105-3.

(192) Musselman, K. P.; Marin, A.; Schmidt-Mende, L.; MacManus-Driscoll, J. L. Incompatible Length Scales in Nanostructured Cu_2O Solar Cells. *Adv. Funct. Mater.* **2012**, *22*, 2202–2208.

(193) Abd-Ellah, M.; Moghimi, N.; Zhang, L.; Heinig, N. F.; Zhao, L.; Thomas, J. P.; Leung, K. T. Effect of Electrolyte Conductivity on Controlled Electrochemical Synthesis of Zinc Oxide Nanotubes and Nanorods. *J. Phys. Chem. C* **2013**, *117*, 6794–6799.

(194) Liu, Y. L.; Liu, Y. C.; Mu, R.; Yang, H.; Shao, C. L.; Zhang, J. Y.; Lu, Y. M.; Shen, D. Z.; Fan, X. W. The Structural and Optical Properties of Cu_2O Films Electrodeposited on Different Substrates. *Semicond. Sci. Technol.* **2004**, *20*, 44–49.

(195) Mizuno, K.; Izaki, M.; Murase, K.; Shinagawa, T.; Chigane, M.; Inaba, M.; Tasaka, A.; Awakura, Y. Structural and Electrical Characterizations of Electrodeposited p-Type Semiconductor Cu_2O Films. *J. Electrochem. Soc.* **2005**, *152*, C179-C182.

(196) Rakhshani, A. E. Preparation, Characteristics and Photovoltaic Properties of Cuprous Oxide—a Review. *Solid. State. Electron.* **1986**, *29*, 7–17.

(197) Hsu, Y. K.; Yu, C. H.; Chen, Y. C.; Lin, Y. G. Synthesis of Novel Cu_2O Micro/nanostructural Photocathode for Solar Water Splitting. *Electrochim. Acta* **2013**, *105*, 62–68.

(198) Nishi, Y.; Miyata, T.; Minami, T. The Impact of Heterojunction Formation Temperature on Obtainable Conversion Efficiency in n-ZnO/p-Cu_2O Solar Cells. *Thin Solid Films* **2013**, *528*, 72–76.

(199) Wu, L.; Tsui, L.; Swami, N.; Zangari, G. Photoelectrochemical Stability of Electrodeposited Cu_2O Films. *J. Phys. Chem. C* **2010**, *114*, 11551–11556.

(200) Paracchino, A.; Brauer, J. C.; Moser, J. E.; Thimsen, E.; Graetzel, M. Synthesis and Characterization of High-Photoactivity Electrodeposited Cu_2O Solar Absorber by Photoelectrochemistry and Ultrafast Spectroscopy. *J. Phys. Chem. C* **2012**, *116*, 7341–7350.

(201) Kuo, S. Y.; Chen, W. C.; Cheng, C. P. Investigation of Annealing-Treatment on the Optical and Electrical Properties of Sol-Gel-Derived Zinc Oxide Thin Films. *Superlattices Microstruct.* **2006**, *39*, 162–170.

(202) Lv, J.; Gong, W.; Huang, K.; Zhu, J.; Meng, F.; Song, X.; Sun, Z. Effect of Annealing Temperature on Photocatalytic Activity of ZnO Thin Films Prepared by Sol-Gel Method. *Superlattices Microstruct.* **2011**, *50*, 98–106.

(203) Kuo, S. Y.; Chen, W. C.; Lai, F. I.; Cheng, C. P.; Kuo, H. C.; Wang, S. C.; Hsieh, W. F. Effects of Doping Concentration and Annealing Temperature on Properties of Highly-Oriented Al-Doped ZnO Films. *J. Cryst. Growth* **2006**, *287*, 78–84.

(204) Ng, Z. N.; Chan, K. Y.; Tohsophon, T. Effects of Annealing Temperature on ZnO and AZO Films Prepared by Sol–gel Technique. *Appl. Surf. Sci.* **2012**, *258*, 9604–9609.

(205) Tauc, J.; Grigorovici, R.; and Vancu, A. Optical Properties and Electronic Structure of Amorphous Germanium. *J Phy. Stat. Sol.* **1966**, 15, 627-637.

(206) Shinagawa, T.; Onoda, M.; Fariza, B. M.; Sasano, J.; Izaki, M. Annealing Effects and Photoelectric Properties of Single-Oriented Cu_2O Films Electrodeposited on Au(111)/Si(100) Substrates. *J. Mater. Chem. A* **2013**, *1*, 9182-9188.

(207) Ievskaya, Y.; Hoye, R. L. Z.; Sadhanala, A.; Musselman, K. P.; MacManus-Driscoll, J. L. Fabrication of ZnO/Cu_2O Heterojunctions in Atmospheric Conditions: Improved Interface Quality and Solar Cell Performance. *Sol. Energy Mater. Sol. Cells* **2014**, *135*, 43–48.

(208) Musselman, B. K. P.; Wisnet, A.; Iza, D. C.; Hesse, H. C.; Scheu, C.; Macmanus-driscoll, J. L.; Schmidt-mende, L. Strong Efficiency Improvements in Ultra-Low-Cost Inorganic Nanowire Solar Cells. *Adv. Mater.* **2010**, 22, E254–E258.

(209) Zou, X.; Fan, H.; Tian, Y.; Zhang, M.; and Yan, X. Chemical bath deposition of Cu_2O quantum dots onto ZnO nanorod arrays for application in photovoltaic devices. *RSC Adv.* **2015**, 5, 23401-23409.

(210) Berweger, S.; Atkin, J. M.; Xu, X. G.; Olmon, R. L.; Raschke, M. B. Femtosecond Nanofocusing with Full Optical Waveform Control. *Nano Lett.* **2011**, *11*, 4309–4313.

(211) Langhammer, C. Nanoplasmonic Sensing for Nanomaterials Science and Catalysis. *SPIE Newsroom.* **2012**.

(212) Dreaden, E. C.; Alkilany, A. M.; Huang, X.; Murphy, C. J.; El-Sayed, M. A. The Golden Age: Gold Nanoparticles for Biomedicine. *Chem. Soc. Rev.* **2012**, *41*, 27402779.

(213) Liu, G. L. Nanoplasmonic-Particle-Enhanced Optical Molecular Sensing. *IEEE J. Sel. Top. Quantum Electron.* **2010**, *16*, 662–671.

(214) Bhattacharya, A.; Rao, V. P.; Jain, C.; Ghose, A.; Banerjee, S. Bio-Sensing Property of Gold Coated ZnO Nanorods. *Mater. Lett.* **2014**, *117*, 128–130.

(215) Georgiev, P.; Bojinova, A.; Kostova, B.; Momekova, D.; Bjornholm, T.; Balashev, K. Implementing Atomic Force Microscopy (AFM) for Studying Kinetics of Gold Nanoparticle's Growth. *Colloids Surfaces A Physicochem. Eng. Asp.* **2013**, *434*, 154–163.

(216) Elghanian, R.; Storhoff, J. J.; Mucic, R. C.; Letsinger, R. L.; Mirkin, C. A. Selective

Colorimetric Detection of Polynucleotides Based on the Distance-Dependent Optical Properties of Gold Nanoparticles. *Science* **1997**, *277*, 1078–1081.

(217) Li, D.; McCann, J. T.; Gratt, M.; Xia, Y. Photocatalytic Deposition of Gold Nanoparticles on Electrospun Nanofibers of Titania. *Chem. Phys. Lett.* **2004**, *394*, 387–391.

(218) Chou, C. S.; Yang, R. Y.; Yeh, C. K.; Lin, Y. J. Preparation of TiO_2/Nano-Metal Composite Particles and Their Applications in Dye-Sensitized Solar Cells. *Powder Technol.* **2009**, *194*, 95–105.

(219) Pala, R. A.; White, J.; Barnard, E.; Liu, J.; Brongersma, M. L. Design of Plasmonic Thin-Film Solar Cells with Broadband Absorption Enhancements. *Adv. Mater.* **2009**, *21*, 3504–3509.

(220) Akimov, Y. A.; Ostrikov, K.; Li, E. P. Surface Plasmon Enhancement of Optical Absorption in Thin-Film Silicon Solar Cells. *Plasmonics* **2009**, *4*, 107–113.

(221) Spinelli, P.; Ferry, V. E.; Van de Groep, J.; Van Lare, M.; Verschuuren, M. A.; Schropp, R. E. I.; Atwater, H. A.; Polman, A. Plasmonic Light Trapping in Thin-Film Si Solar Cells. *J. Opt.* **2012**, *14*, 024002-11.

(222) Ferry, V. E.; Verschuuren, M. A; Li, H. B. T.; Verhagen, E.; Walters, R. J.; Schropp, R. E. I.; Atwater, H. A; Polman, A. Light Trapping in Ultrathin Plasmonic Solar Cells. *Opt. Express* **2010**, 18, A237–A245.

(223) Ferry, V. E.; Munday, J. N.; Atwater, H. A. Design Considerations for Plasmonic Photovoltaics. *Adv. Mater.* **2010**, *22*, 4794–4808.

(224) Pillai, S.; Green, M. A. Plasmonics for Photovoltaic Applications. *Sol. Energy Mater. Sol. Cells* **2010**, *94*, 1481–1486.

(225) Stratakis, E.; Kymakis, E. Nanoparticle-Based Plasmonic Organic Photovoltaic Devices. *Mater. Today* **2013**, *16*, 133–146.

(226) Zhu, J.; Xue, M.; Shen, H.; Wu, Z.; Kim, S.; Ho, J. J.; Hassani-Afshar, A.; Zeng, B.; Wang, K. L. Plasmonic Effects for Light Concentration in Organic Photovoltaic Thin Films Induced by Hexagonal Periodic Metallic Nanospheres. *Appl. Phys. Lett.* **2011**, *98*, 13–16.

(227) Chen, F. C.; Wu, J. L.; Lee, C. L.; Hong, Y.; Kuo, C. H.; Huang, M. H. Plasmonic-Enhanced Polymer Photovoltaic Devices Incorporating Solution-Processable Metal Nanoparticles. *Appl. Phys. Lett.* **2009**, *95*, 013305-3.

(228) Kochergin, V.; Neely, L.; Jao, C. Y.; Robinson, H. D. Aluminum Plasmonic Nanostructures for Improved Absorption in Organic Photovoltaic Devices. *Appl. Phys. Lett.* **2011**, *98*, 1–4.

(229) Gan, Q.; Bartoli, F. J.; Kafafi, Z. H. Plasmonic-Enhanced Organic Photovoltaics: Breaking the 10% Efficiency Barrier. *Adv. Mater.* **2013**, *25*, 2385–2396.

(230) Brown, M. D.; Suteewong, T.; Kumar, R. S. S.; D'Innocenzo, V.; Petrozza, A.; Lee, M. M.; Wiesner, U.; Snaith, H. J. Plasmonic Dye-Sensitized Solar Cells Using Core-Shell Metal-Insulator Nanoparticles. *Nano Lett.* **2011**, *11*, 438–445.

(231) McCune, M.; Zhang, W.; Deng, Y. High Efficiency Dye-Sensitized Solar Cells Based on Three-Dimensional Multilayered ZnO Nanowire Arrays with "Caterpillar-like" Structure. *Nano Lett.* **2012**, *12*, 3656–3662.

(232) Ko, S. H.; Lee, D.; Kang, H. W.; Nam, K. H.; Yeo, J. Y.; Hong, S. J.; Grigoropoulos, C. P.; and Sung, H. J. Nanoforest of Hydrothermally Grown Hierarchical ZnO Nanowires for a High Efficiency Dye-Sensitized Solar Cell. Nano Lett. 2011, 11, 666–671.

(233) Ku, C. H.; Wu, J. J. Electron Transport Properties in ZnO Nanowire Array/nanoparticle Composite Dye-Sensitized Solar Cells. *Appl. Phys. Lett.* **2007**, *91*, 093117-3.

(234) Bhattacharjee, R.; Hung, I. M. A SnO_2 and ZnO Nanocomposite Photoanodes in Dye-Sensitized Solar Cells. *ECS Solid State Lett.* **2013**, *2*, Q101–Q104.

(235) Peh, C. K. N.; Ke, L.; Ho, G. W. Modification of ZnO Nanorods through Au Nanoparticles Surface Coating for Dye-Sensitized Solar Cells Applications. *Mater. Lett.* **2010**, *64*, 1372–1375.

(236) Standridge, S. D.; Schatz, G. C.; Hupp, J. T. Toward Plasmonic Solar Cells: Protection of Silver Nanoparticles via Atomic Layer Deposition of TiO_2. *Langmuir* **2009**, *25*, 2596–2600.

(237) Chen, Z. H.; Tang, Y. B.; Liu, C. P.; Leung, Y. H.; Yuan, G. D.; Chen, L. M.; Wang, Y. Q.; Bello, I.; Zapien, J. A.; Zhang, W. J. Lee, C. S.; and Lee, S. T.; Vertically Aligned ZnO Nanorod Arrays Sentisized with Gold Nanoparticles for Schottky Barrier Photovoltaic Cells. *J. Phys. Chem. C* **2009**, 133, 13433–13437.

(238) Joseph, Y.; Besnard, I.; Rosenberger, M.; Guse, B.; Nothofer, H. G.; Wessels, J. M.; Wild, U.; Knop-Gericke, A.; Su, D.; Schlo1gl, R.; Yasuda, A.; and Vossmeyer, T. Self-Assembled Gold Nanoparticle/Alkanedithiol Films: Preparation, Electron Microscopy, XPS-Analysis, Charge Transport, and Vapor-Sensing Properties. *J. Phys. Chem. B* **2003**, 107, 7406-7413.

(239) Lasia, A. *Electrochemical Impedance Spectroscopy and Its Applications*; New York, Springer, **2014**.

(240) Link, S.; El-Sayed, M. A. Size and Temperature Dependence of the Plasmon Absorption of Colloidal Gold Nanoparticles. *J. Phys. Chem. B* **1999**, *103*, 4212-4217.

(241) Pillai, S.; Catchpole, K. R.; Trupke, T.; Green, M. A. Surface Plasmon Enhanced Silicon Solar Cells. *J. Appl. Phys.* **2007**, *101*, 1–9.

(242) Hu, X.; Blackwood, D. J. Influence of Au Particles on the Photocurrent of TiO_2 Films. *J. Electroceramics* **2006**, *16*, 593–598.

(243) Bora, T.; Kyaw, H. H.; Sarkar, S.; Pal, S. K.; Dutta, J. Highly Efficient ZnO/Au Schottky Barrier Dye-Sensitized Solar Cells: Role of Gold Nanoparticles on the Charge-Transfer Process. *Beilstein J. Nanotechnol.* **2011**, *2*, 681–690.

(244) Snaith, H. J.; Ducati, C. SnO_2-Based Dye-Sensitized Hybrid Solar Cells Exhibiting near Unity Absorbed Photon-to-Electron Conversion Efficiency. *Nano Lett.* **2010**, *10*, 1259–1265.

(245) Chou, T. P.; Zhang, Q.; Cao, G.; Science, M.; Hall, R. Effects of Dye Loading Conditions on the Energy Conversion Efficiency of ZnO and TiO_2 Dye-Sensitized Solar Cells. *Society* **2007**, 111, 18804–18811.

(246) Birkel, A.; Lee,Y.; Koll, D.; Meerbeek, X. V.; Frank, S.; Choi, M. J.; Kang,Y. S.; Char, K.; and Tremel, W. Highly efficient and stable dye-sensitized solar cells based on SnO_2 nanocrystals prepared by microwave-assisted synthesis. *Energy Environ. Sci.* **2012**, 5, 5392–5400.

(247) Gubbala, S.; Chakrapani, V.; Kumar, V.; Sunkara, M. K. Band-Edge Engineered Hybrid Structures for Dye-Sensitized Solar Cells Based on SnO_2 Nanowires. *Adv. Funct. Mater.* **2008**, *18*, 2411–2418.

(248) Docampo, P.; Tiwana, P.; Sakai, N.; Miura, H.; Herz, L.; Murakami, T.; Snaith, H. J. Unraveling the Function of an MgO Interlayer in Both Electrolyte and Solid-State SnO_2 Based Dye-Sensitized Solar Cells. *J. Phys. Chem. C* **2012**, *116*, 22840–22846.

(249) Senevirathna, M. K. I.; Pitigala, P. K. D. D. P.; Premalal, E. V. A. Stability of the SnO_2/MgO Dye-Sensitized Photoelectrochemical Solar Cell. **2007**, *91*, 544–547.

(250) Gubbala, S.; Russell, H. B.; Shah, H.; Deb, B.; Jasinski, J.; Rypkema, H.; Sunkara, M. K. Surface Properties of SnO_2 Nanowires for Enhanced Performance with Dye-Sensitized Solar Cells. *Energy Environ. Sci.* **2009**, *2*, 1302-1309.

(251) Lee, D.; Rho, Y.; Allen, F. I.; Minor, A. M.; Ko, S. H.; Grigoropoulos, C. P. Synthesis of Hierarchical TiO_2 Nanowires with Densely-Packed and Omnidirectional Branches. *Nanoscale* **2013**, *5*, 11147–11152.

(252) Herman, I.; Yeo, J.; Hong, S.; Lee, D.; Nam, K. H.; Choi, J.; Hong, W.; Lee, D.; Grigoropoulos, C. P.; Ko, S. H. Hierarchical Weeping Willow Nano-Tree Growth and Effect of Branching on Dye-Sensitized Solar Cell Efficiency. *Nanotechnology* **2012**, *23*, 194005-5.

(253) Bazargan, S.; Leung, K. T. Growth of randomly oriented single-crystalline tin (IV) oxide nanobelts: Control on the predominant crystalline growth axis. *J. Chem. Phys.* **2013**, 138, 104704-9.

(254) Castro, R. H. R.; Hidalgo, P.; Muccillo, R.; Gouvêa, D. Microstructure and Structure of NiO-SnO_2 and Fe_2O_3-SnO_2 Systems. *Appl. Surf. Sci.* **2003**, *214*, 172–177.

(255) Subash, B.; Krishnakumar, B.; Swaminathan, M.; Shanthi, M. Highly Efficient, Solar Active, and Reusable Photocatalyst: Zr-Loaded Ag-ZnO for Reactive Red 120 Dye Degradation with Synergistic Effect and Dye-Sensitized Mechanism. *Langmuir* **2013**, *29*, 939–949.

(256) Lao, J. Y.; Huang, J. Y.; Wang, D. Z.; Ren, Z. F. ZnO Nanobridges and Nanonails. *Nano Lett.* **2003**, *3*, 235–238.

(257) Chen, Y. X.; Campbell, L. J.; Zhou, W. L. Self-Catalytic Branch Growth of SnO_2 Nanowire Junctions. *J. Cryst. Growth* **2004**, *270*, 505–510.

(258) Liang, Y.-C.; Zhong, H. Self-Catalytic Crystal Growth, Formation Mechanism, and Optical Properties of Indium Tin Oxide Nanostructures. *Nanoscale Res. Lett.* **2013**, *8*, 358-359.

(259) Kay, A.; Gra, M. Dye-Sensitized Core-Shell Nanocrystals : Improved Efficiency of Mesoporous Tin Oxide Electrodes Coated with a Thin Layer of an Insulating Oxide. Chem. Mater. **2002**, 14, 2930–2935.

(260) Barpuzary, D.; Patra, A. S.; Vaghasiya, J. V.; Solanki, B. G.; Soni, Saurabh S.; and Qureshi , M. Highly Efficient One-Dimensional ZnO Nanowire-Based Dye-Sensitized Solar Cell Using a Metal-Free, D−π−A-Type, Carbazole Derivative with More than 5% Power Conversion. *ACS Appl. Mater. Interfaces* **2014**, 6, 12629–12639.

(261) Yu, M.; Ren, X.; Ma, L.; and Wu, Y. Integrating a redox-coupled dye-sensitized photoelectrode into a lithium–oxygen battery for photoassisted charging. *Nat. Commun.* **2014**, 5, 1-6.